Adhesion Mechanics of Graphene

by

Narasimha Boddeti

Advisor: Prof. Martin L Dunn

A thesis submitted to the

Faculty of the Graduate School of the

University of Colorado in partial fulfillment

of the requirement for the degree of

Doctor of Philosophy

Department of Mechanical Engineering

2014

This thesis entitled:

Adhesion Mechanics of Graphene

written by Narasimha Boddeti

has been approved for the Department of Mechanical Engineering

_____

Martin L. Dunn

Committee Chairman

_____

Jianliang Xiao

Department of Mechanical Engineering

*Date*_____

The final copy of this thesis has been examined by the signatories, and we

Find that both the content and the form meet acceptable presentation standards

Of scholarly work in the above mentioned discipline.

Narasimha Boddeti (Mechanical Engineering)

Adhesion Mechanics of Graphene

Thesis directed by Professor Martin L. Dunn

Abstract

Graphene, being an atomically thin two dimensional crystalline material with a very low mass and high elastic strength, has great potential in next generation nano-mechanical devices. Additionally, it has attractive electronic, thermal and optical properties. In spite of possessing a high Young's modulus, graphene is highly bendable and ultra-floppy due to its atomic thickness. At the nano-scale the surface forces are very strong and being very flexible makes graphene membranes interact and adhere strongly to materials and structures in its vicinity. The effect of these interactions needs to be understood at different length scales – micro, nano and atomistic level to be able to design efficient and reliable graphene based nano-devices like electromechanical switches and resonators. Through this work, in the first step, we measure the strength of the adhesion of graphene membranes to a substrate using modified blister tests with the help of a detailed model accounting for the non-linear mechanics of graphene and the thermodynamics of the blister test. We also demonstrate, along the way, graphene nano-mechanical devices that can switch shapes depending on the applied pressure, adhesion strength, geometry etc. In the second step, an attempt is made to characterize the surface forces through a novel experimental setup involving pull-in of graphene membranes. The experimental observations are satisfactorily explained with the help of an analytical model. Finally, we investigate the atomistic mechanisms of adhesion and de-adhesion of graphene membranes. We used molecular mechanics simulations to investigate the effect of topography on graphene adhesion energy. The analytical model we developed captures the basic physics involved in these simulations quite well. We also study, using

the same methodology, the peeling of graphene membranes on 1D sinusoidal corrugated substrates. The results reveal that the peel mechanics involves periodic instabilities due to the corrugated nature of the substrate and sliding of the graphene atoms on the substrate.

Acknowledgements

"If I have seen further it is by standing on ye shoulders of Giants" – said Isaac Newton. It is no different in my case as all the work I have done and presented in this thesis draws upon the work done by researchers preceding me. I duly acknowledge them and can only hope to emulate them in my future.

I am grateful to my parents, family and friends who were always there to support and encourage me. I am thankful to my colleagues and co-authors – Steven Koenig, Xinghui Liu, Luda Wang, Harris Hall, Kevin Long and Rong Long. They have inspired me in many different ways, let me pick their brains and bounce ideas off of. Professors Xiao and Bunch have mentored me through different stages of my PhD and am grateful for their willingness to help me whenever I needed some.

I was pretty much like a lump of clay when I started my doctoral studies and I am very grateful to my advisor Prof. Martin Dunn for trusting and being patient with me. I am especially thankful to him for teaching me the propriety of conducting research, writing papers and presenting one's work which I would like to build upon and carry on with beyond my doctoral studies.

I will always cherish the time spent in the Mechanical Engineering department, in the University of Colorado Boulder and in the city of Boulder.

Table of Contents

List of Tables

List of Figures

xiii

1. Introduction

1.1 Graphene

1.1.1 Graphene: Characteristics and Properties

Figure 1.1 Single layer graphene (from http://en.wikipedia.org/wiki/Graphene)

Graphene is a single atomic layer of sp2-bonded carbon atoms arranged in a hexagonal lattice. When graphene sheets are stacked on each other, they form graphite – an allotrope of carbon just like diamond. Graphene sometimes also refers to its multi-layered counterparts (bi-layer, tri-layer etc.). It was first isolated by mechanical exfoliation of graphite[1] with a scotch tape. Ever since, several other methods of graphene synthesis focusing on mono-layer production have been proposed and realized. They include physical methods like exfoliation by graphite sonication in a suitable solvent[2] and electro-static exfoliation[3] and chemical methods of epitaxial growth or chemical vapor deposition (CVD) on a variety of substrates including SiC,[4,5] Ir,[6] Ru,[7] Ni,[8,9] Cu,[10] Pt,[11] and Pd.[12] Growth by CVD on polycrystalline copper foils using methane gas has become widely used due to the ability to grow large mono-layer flakes, low cost and ease of transfer to

1

other substrates. This method, however, produces polycrystalline graphene which possesses degraded material properties.[13] This problem is overcome in a recent development by wafer scale growth of single crystal graphene on Si wafers with a hydrogen terminated Ge buffer layer.[14] The single crystal Ge aligns the seed growth at multiple nucleation sites which then coalesce to form a larger single crystal.
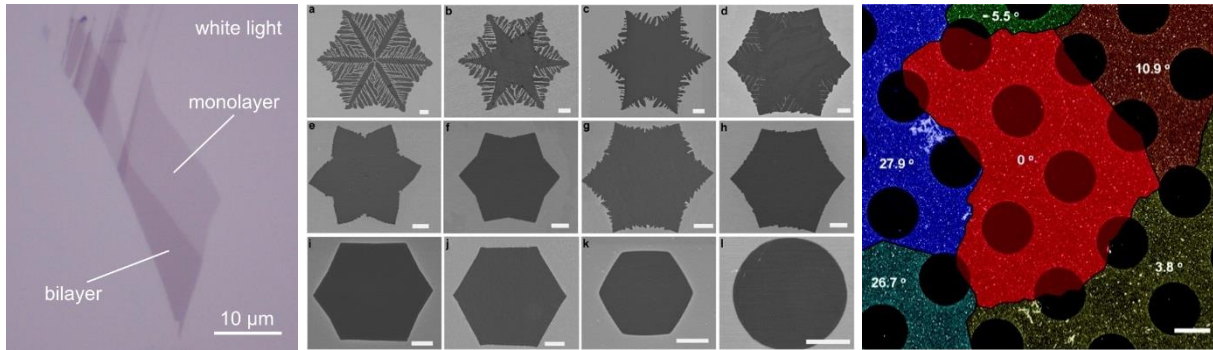
Figure 1.2 (a) Optical image of exfoliated graphene flake on 90 nm SiO₂ (from grapheneindustries.com) (b) Scanning electron microscopy (SEM) images of single crystal CVD graphene of various shapes grown on liquid Cu under different conditions[15] (all scale bars – 5 µm) (c) Scanning transmission electron microscopy (STEM) image of a polycrystalline CVD graphene flake with grains and grain boundaries identified[16] (false colors, scale bar – 1 µm)

The CVD or epitaxially grown graphene usually needs to be transferred to a desired substrate. This transfer step usually results in wrinkling, tearing or cracking of graphene.[10,17] Thus, mechanical exfoliation has still remained one of the most used methods in spite of its inefficiency. It is favored for graphene device research due to its straightforward nature coupled with the ability to produce relatively large defect free graphene flakes compared to other methods. The most commonly used substrate for fabrication of graphene devices is a Si wafer with thermally grown oxide layer of specific thickness (90 or 280 nm). These specific thicknesses enable experimenters to easily identify graphene flakes with various thicknesses optically.[18]

Graphene is found to have remarkable mechanical strength with a Young's modulus of about 1 TPa.[19] It also has remarkable electronic, thermal, chemical and optical properties.[20] The electrons in graphene can travel long distances without being scattered.[20,21] It is also found to be impermeable to all gases.[22] All this along with small mass makes it an attractive choice for future electronic devices and nano-electromechanical systems.

1.1.2 Graphene: Potential Applications

A great volume of graphene based nano-device research focuses on electronic switches that can potentially replace Si CMOS transistors, due to its unique electronic properties.[23] It has also found use in batteries and as electrode material that can potentially replace ITO (Indium Tin Oxide) in displays and photovoltaic applications.[24,25] Beyond electronics, graphene based gas and bio-sensors have been proposed.[26] Graphene based mechanical switches[27,28] and resonators[29,30] have been realized. It has also found potential use as a membrane for gas separation[31,32] and for water desalination.[33] The list goes on and graphene has undoubtedly captured the imagination of the current research community as the material of the future.

1.2 Interfacial Forces and Adhesion

1.2.1 Interfacial forces: Origin and Characteristics

The atoms on the surface behave differently compared to those in the bulk, due to the surface atoms having fewer bonds than the bulk counterparts. This is the reason why surfaces play an important role in catalytic chemistry. When two surfaces come together, they start interacting via a variety of forces which are all manifestations of electromagnetic interactions like hydrogen bonds, electrostatic interactions, dispersion forces etc. These forces especially play an important role in determining the properties of membranes (structures with dimension along the thickness

much smaller compared to lateral dimensions) considering that they have fewer bulk atoms and typically flexible. This is especially true in the case of graphene which does not have any bulk atoms being just one atomic layer thick.

Let us discuss some of the surface force phenomena which are long range (> few nm's) namely electrostatic forces, van der Waals interactions and Casimir forces.

- Electrostatic forces arise due to the presence of charged particles on surfaces which are either defects or adsorbed particles. They can be either repulsive or attractive and generally obey the inverse square law.

- Van der Waals (vdW) forces are interactions between dipoles or induced dipoles or instantaneous dipoles and are present even between neutral atoms. The force is usually attractive except below a critical sub-nanometer separation. The cumulative effect of these atomic and molecular level forces can be seen even at macro-scale. They play a crucial role in many biological systems as well as in micro-/nano-electromechanical systems. These forces are known to cause "stiction" in micro/nano-devices. These same forces give organisms like geckos the ability to adhere and balance their entire weight through setae on their feet.[34]

- Casimir forces can be termed as vdW interactions where a concept known as "retardation" comes into play. It is stated that vdW interactions arise due to interacting dipoles. When a pair of dipoles are close enough and when one dipole changes its orientation or strength, the other can react almost instantaneously. But when they are moved apart, the other dipole can only respond in a "retarded manner". Hence Casimir forces act at a longer range than vdW forces.

A lot of research went into understanding how these surface interactions are affected by geometry and medium. These surface forces, as noted already, play an important role in adhesion of materials spanning a wide range of scales.

1.2.2 Macro/Meso-scale Adhesion

At macro/meso-scales adhesion due to aforementioned surface forces is usually dominated by other forces (like gravity, capillary forces etc.). Hence adhesion is achieved either mechanically (joints, Velcro etc.) or chemically (glue). A lot of engineering applications involve adhesives and adhesion, which led to development of methods to characterize adhesion/adhesive and measure the strength of adhesion like the peel and blister tests for thin films and membranes. These tests involve creation of a "crack" or "fracture" in the interface of the two adhered bodies or the adhesive itself, if present. Some of the commonly used peel tests include 90° peel test, 180° peel test, V-peel test etc. Similarly, some commonly used blister tests are standard blister test, island blister test, peninsula blister test etc. Adhesion can also be measured using contact mechanics tests like JKR, DMT etc. in some cases. In addition, buckling of stressed thin films also provides a way to measure adhesion energy.

1.2.3 Micro/Nano-scale Adhesion

The surface forces like vdW interactions become more important at micro and nano-scales due to smaller separations involved. The surface forces have become the biggest obstacle to realizing efficient and reliable mechanical devices at this scale. A lot of effort has been made to minimize the effect of these forces on the operation of micro/nano devices. Some of the solutions developed are optimizing the geometry, using surface coatings to reduce the strength of these interactions and changing the surface topography to make them rougher to reduce the area of contact.[35] Adhesion or adhesive forces can be measured even at this scale by many of the methods

5

mentioned in the previous sub-section. In addition, methods and apparatus like cantilever beam array technique, nano-indentation, surface forces apparatus (SFA), atomic force microscopy (AFM) etc. are also commonly used at these length scales.

Even though the surface interactions at micro/nano scale are undesirable for M/NEMS devices, they are the operant forces in scanning probe microscopy techniques like AFM which have not only found use in measuring nano-scale topography but also in measuring friction and mechanical properties on micro/nano-scale surfaces. Adhesion at this scale also finds use in self-assembly of nano-particles and bio-membranes. It is also important in effective development of new generation electronic and magnetic storage devices based on hetero-structures of thin films.

1.3 Motivation for this Research
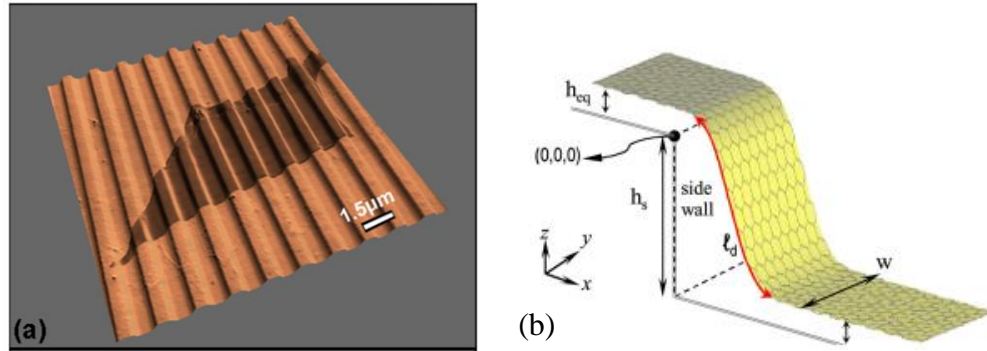
Figure 1.3 (a) AFM image of graphene conformed to a corrugated PDMS substrate[36] (b) Graphene over a substrate step, the deformation is dictated by substrate interactions[37]

Graphene with all its unique features and versatile properties, some of which are discussed already, is poised to be the material of the future. It is a membrane with no bulk – very thin and flexible. This means graphene is highly susceptible to the influence of surface forces and adhesion should play a critical role in the functioning of graphene based devices especially nano-mechanical devices like switches and resonators. It is found that graphene can conform to a patterned substrate very well due to the operant surface forces.[36] It is also found that the thermal[38] and electrical

properties[37] can be affected by how graphene adheres to a substrate. Furthermore, electronic properties can be tailored by strain engineering[39] and this can be achieved through deliberate deformation of graphene via surface interactions on a patterned substrate. Hence it is important to develop a good understanding of graphene adhesion and the mechanics behind graphene adhesion to enable better design and development of graphene based nano devices. This work should not only help with regards to graphene but also other two dimensional materials like BN, MoS_2 etc. Also, with the increasing use of epitaxially/CVD grown graphene and other thin films, understanding adhesion becomes more important for effective transfer of these films/membranes to other desired substrates.

1.4 Research Objectives and Scope

1.4.1   Mechanics of Graphene Membrane Configurations

The first step to understanding the adhesion mechanics is to understand how graphene membranes behave under the application of a variety of loads and boundary conditions. In this work, we concentrate on axi-symmetrically loaded graphene membrane problems. We try to understand graphene mechanics in a continuum elasticity framework and perform experiments to validate the theory.

1.4.2   Surface forces and Adhesion

We model modified blister tests based on the standard blister test and island blister test with graphene and use these models to measure adhesion energy of graphene on a given substrate. We also discuss how the graphene mechanical structures used in the modified blister tests can have potential applications in nano-electromechanical systems. The blister tests, however, do not reveal

the characteristics of the nano-scale surface forces leading to the adhesion. To do just that, we devise an experiment and model it analytically.

1.4.3   *Mechanics of Graphene Adhesion*

The blister tests provide a global averaged measure of the adhesion energy, but do not reveal any details of the local delamination mechanics. Hence, we take the simulation approach to understand the atomistic details of delamination and the effect of substrate corrugations on the adhesion. We develop an analytical framework to fit the simulation results in a continuum elastic framework.

1.5 Thesis Organization

The thesis is organized into six subsequent chapters. Chapter 2 is a brief literature survey on mechanical properties, adhesion and mechanics of graphene, and a general review of work on membrane mechanics and adhesion. Chapter 3 deals with a modified standard blister test of graphene where we create pressurized graphene blisters, while Chapter 4 deals with a modified island blister test of graphene where we create pressurized annular blisters. A detailed analysis of the thermodynamics is discussed and experimental results are presented in these chapters. Chapter 5 extends the work of Chapters 3 and 4 in understanding and characterizing the surface forces with the help of a novel experimental setup.

In Chapter 6, we propose and discuss the theory behind graphene island blister based nano-electromechanical systems where we used the knowledge gained in the previous chapters to design novel nano-devices. In Chapter 7, we discuss the details of the atomistic simulations we performed and the key insights they present into the adhesion mechanics of graphene membranes on

corrugated as well as flat substrates. We also discuss companion theoretical analyses that describe

and aid in understanding the results of the simulations.

2. Background and Literature Review

2.1 Mechanical Properties of Graphene
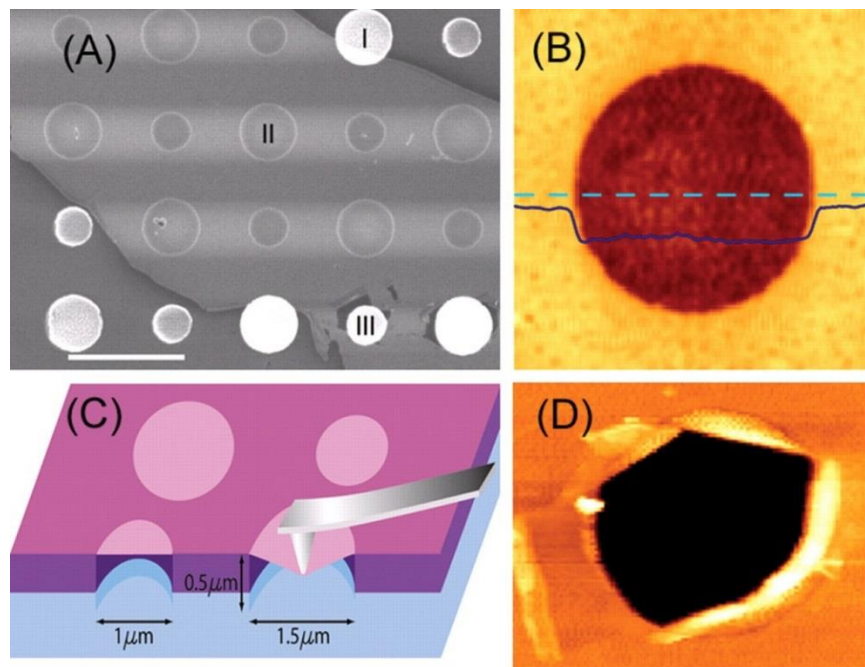
Figure 2.1 (a) Scanning electron micrograph of a graphene suspended over micro-cavities, (b) AFM image of suspended graphene, (c) Schematic of nano-indentation of suspended graphene, (d) AFM image of a fractured membrane[19]

The mechanical properties of graphene were well known theoretically even before it was isolated. This is because graphene is known to form the basis for graphite and carbon nanotubes which are structurally similar to graphene. As a result, a number of numerical analyses focused on carbon nanotubes also studied graphene. Some such efforts like Lier et al[40] have found the Young's modulus (E) of graphene to be 1.11 TPa using *ab initio* calculations, whereas Kudin et al[41] found it to be 1.02 TPa, again using *ab initio* calculations. The latter have reported a Poisson's ratio (v) of 0.149 for graphene. Some of the experimental efforts include atomic force microscopy (AFM) measurement of effective spring constants of suspended multi-layered graphene sheets by Frank et al[42] and AFM nano-indentation of suspended single layered graphene sheets by Lee et al.[19] Both

the experiments involve adherence of graphene sheets to the substrate through van der Waals and other interactions. They have obtained values of 0.5 TPa for multi-layered graphene and 1 TPa for single layered graphene respectively. Frank et al used suspended doubly clamped multi-layered graphene beams and measured their stiffness with an AFM to deduce the value of E and tension in the membranes. Lee et al, on the other hand, use an AFM to indent suspended clamped circular graphene membranes as shown in Fig. 2.1 to obtain E.

The thickness values for mono-layer graphene (t) found in the literature are scattered. Yakobson et al[43] reported a value of 0.066 nm and Lu[44] used a value of 0.34 nm, same as the inter-layer distance in graphite. Lee et al[19] assume a value of 0.335 nm for their calculations. Huang et al,[45] starting from arbitrary multi-body interatomic potentials for carbon, obtained an analytical expression for thickness of graphene which depends on the type of loading applied. They have obtained values of 0.0574 nm for thickness, 4.23 TPa for Young's modulus and 0.397 for Poisson's ratio for the case of uniaxial tension using second generation Brenner potential.

The bending rigidity for monolayer graphene is found to be between 1.4-1.46 eV according to Kudin et al[41]. Arroyo and Belytschko[46] put it at 0.83 eV based on calculations using an empirical potential. Koskinen and Kit,[47] using density functional tight binding (DFTB) simulations and revised periodic boundary conditions (RPBC), give a value of 1.61 eV, 180 eV and 690 eV for monolayer, bilayer and trilayer graphene respectively. They also give an analytical expression to calculate the bending rigidity, κ_n of a n layer graphene membrane:

$$\kappa_n = n\kappa_1 + \frac{Et^3(n^3 - n)}{12} \tag{2.1}$$

The bending rigidity, D of plates and membranes in continuum mechanics is given by $D = Et^3/12(1 - v^2)$. This gives a value of about $D = 20$ eV for monolayer graphene, which is an order

of magnitude higher than the value obtained using atomistic calculations. Using density functional techniques (DFT), Wei et al[48] obtained a value of 1.44 eV for monolayer graphene. Experimental efforts using lattice dynamics of graphite obtained a value of 1.4 eV[49] while experiments involving buckling of suspended bilayer graphene membranes by Lindahl et al gave a value of $35.5\,^{+20}_{-15}$ eV.[50]

2.2 Graphene Membrane Mechanics

2.2.1 *Mechanics of Plates and Membranes*

The mechanics of plates can be comprehensively described by the von Karman plate equation, provided the rotations are small compared to unity.[51,52] The von Karman plate equation does not have an analytical solution and has attracted the attention of applied mathematicians over the years. With the arrival of numerical techniques like finite element analysis, engineers were able to solve the equation in a variety of situations very easily. The mechanics of plates involves two distinct regimes – bending dominated and stretching dominated. In the bending dominated regime, the plate deformation is linear with respect to the load while in the stretching dominate regime, it hardens and has a cubic relation with the load. Timoshenko and several others developed approximate solutions to describe mechanics of circular plates for a pressure load (p):

$$pa^4 = A_1 D w_0 + A_2 E t w_0^3 \qquad (2.2)$$

Here, A_1 and A_2 are constants dependent on Poisson's ratio and boundary conditions, a is the radius of the plate and w_0 is the maximum deflection of the plate which occurs at the center. It can be clearly seen that when the deflection is small ($\sim t$), then the pressure is linearly proportional to w_0. When deflection is large ($> t$), then the pressure is proportional to cube of w_0.

A membrane, by definition, is a thin structure with zero or negligible bending rigidity. Examples include cloth and many biological films. Plate mechanics can be effectively used to describe membrane mechanics by considering D to be negligibly small which is true for extremely thin films. Hencky[53] provided an accurate description of the mechanics of uniformly pressurized circular membranes pinned at the boundary. Campbell[54] extended this to initially tensioned membranes. Fichter[55] noted that Hencky's solution neglects the radial component of the applied pressure and solved the reformulated problem with this radial component included. The problem of uniformly pressurized axisymmetric annular membranes is very interesting due to the possibility of symmetry breaking and wrinkle formation and has again garnered attention from applied mathematicians.[56] Approximate solutions have been developed by Williams[57] and Saif et al.[58]

2.2.2 Mechanics of Graphene

This sub-section describes some early work done on mechanics of graphene. Xu and Liao[59] have obtained molecular dynamics and non-linear finite element solutions for single layer as well as multi-layer circular graphene sheets subjected to a transverse central load. They have reported an error of 8-9% for central maximum deflection for single layer graphene sheets between molecular dynamics calculations and the continuum based calculations. Kitipornchai et al[60] have done vibration analysis of multilayer graphene sheets based on a continuum plate model. They have obtained an explicit formula to predict vdW force between any two layers of graphene using Lennard-Jones potential. Starting from an atomistic approach, Atalaya et al[61] obtained simplified continuum elasticity descriptions for modeling the mechanics of graphene sheets. They have finally arrived at von Karman equations for thin plates, without assuming the graphene sheet to be a plate a priori. Duan and Wang[62] have used molecular simulations to determine the static response of clamped circular graphene sheets.

Bao et al explained formation of periodic ripples on suspended few layer graphene using continuum theory.[63] In addition, the experiments on measurement of elastic properties of graphene all used continuum models. Hence it is well established in the literature that the mechanics of graphene membrane can be effectively described by continuum elasticity.

2.3 Adhesion of graphene based systems

2.3.1 Membrane Adhesion

Membranes, being flexible, can adhere very well to substrates. As mentioned in the earlier chapter, adhesion measurement techniques include peel tests and blister tests. Williams provides a nice review of all the commonly used peel and blister tests[57] for different geometries. Considerable amount of research has been done and is still carried out on adhesion of biological membranes.[64] Attempts have been made to establish a generalized theory to understand adhesion of membranes on patterned substrates.[65,66]

(a) (b)
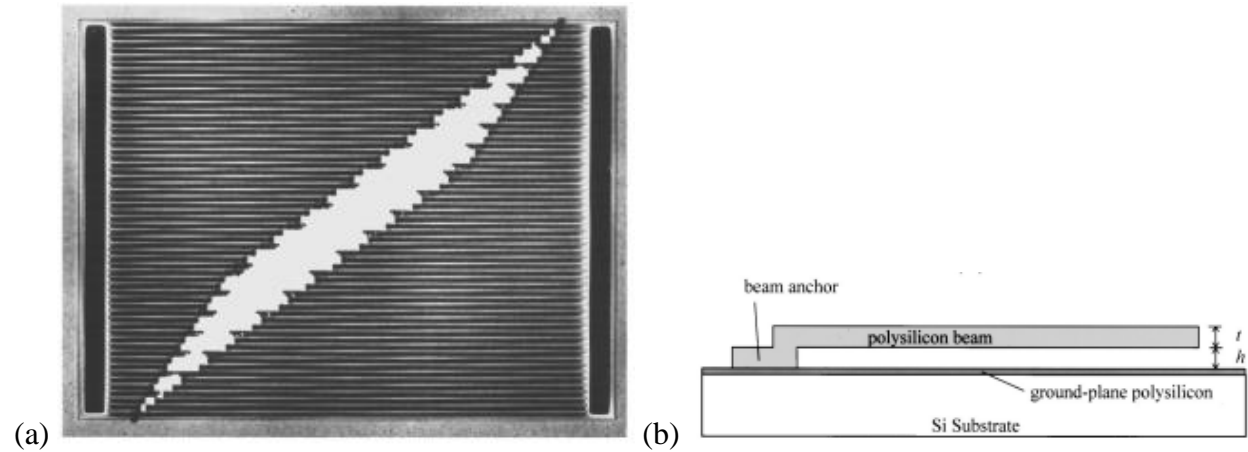
Figure 2.2 Cantilever beam array[35] (a) Optical image (b) Schematic

At micro and nano scales, blister and peel tests may not be carried out as easily when compared to macro-scale. Hence, novel techniques like cantilever beam array technique (see Fig. 2.2) and surface forces apparatus (see Fig. 2.3) have been developed to measure adhesion energy

as well as adhesive forces at these scales. Cantilever beam array technique takes advantage of the phenomenon of pull-in of cantilever beams due to the surface forces at micro/nano length scales. It involves use of an array of cantilever beams with varying lengths suspended over a substrate. The more compliant beams are pulled into contact with the underlying substrate under the influence of the strong surface forces while the stiffer ones stay suspended. The adhesion energy is calculated from the maximum length of the cantilever that is required to stay suspended.
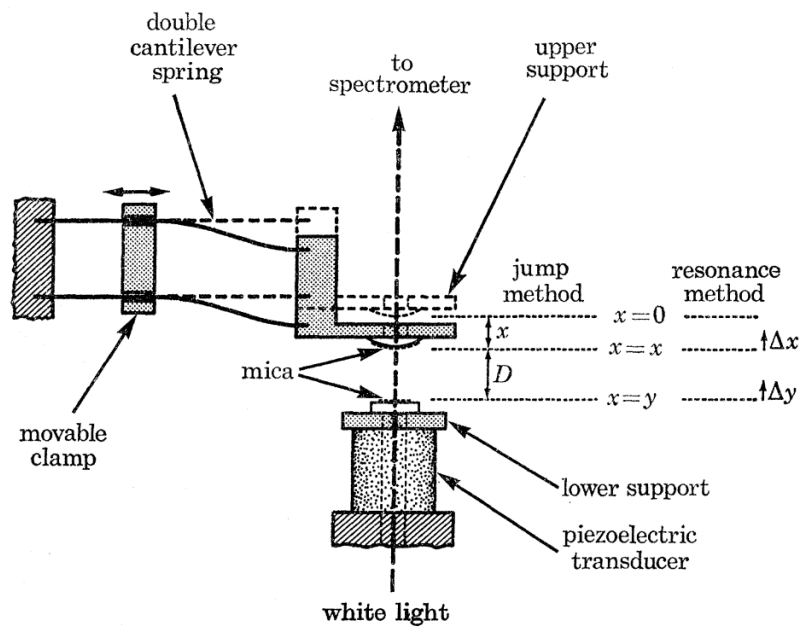
Figure 2.3 Schematic of the surface forces appartus[67]

The surface forces apparatus (SFA) developed by Tabor, Winterton and Israelachvili has been used to measure the vdW, Casimir and electrostatic forces at very small separations (~ 1 nm) between surfaces.[67,68] The SFA uses either the 'jump method' or the 'resonance method' to measure the forces while the distance between the surfaces is measured using optical interferometry. In the 'jump method', one surface is fixed while the other is attached to a cantilever spring and the distance between the surfaces is gradually decreased until they jump into contact at a critical distance. The magnitude of the operant forces can be calculated using this distance. In

15

the 'resonance method', one surface is vibrated at a known frequency in a low pressure environment which induced vibrations in the other surface due to modulation of the surface forces. The induced vibrations are measured to obtain the strength of the operant surface force. It has to be noted that the SFA, though can measure adhesive forces at very small separations, cannot measure adhesive forces either on thin films or nano-scale materials like graphene.

An atomic force microscope (AFM) can also be used to measure the effect of adhesive forces on a variety of surfaces and different operating conditions. But this method is limited by the fact that one surface is the AFM probe tip which has a small area resulting in a small contact area unlike in the SFA. Also with the AFM, the distance between the tip and the sample are not directly measurable in contrast to the SFA. However, AFM's are capable of measuring adhesion strength of thin films via indentation and scratch tests.

2.3.2   Graphene Adhesion

Graphene, like other membranes is affected by surface forces and adheres to any given substrate strongly. The adhesion strength is strong enough to keep the graphene membranes clamped onto a substrate in experiments on suspended graphene devices. Lu and Dunn[69] have done some of the early work on adhesion using atomistic simulations. They looked at the problem of peeling of graphene suspended over a trench and partially adhered to the side walls. They conclude that the atomistic simulations results can satisfactorily be explained with continuum mechanics. Computational studies of graphene on Ni(111)[70] and Ru(0001)[71] give adhesion energies of 0.12 J/m^2 and 0.17 J/m^2. Rudenko et al[72] used computational studies to determine the adhesion energy of graphene on mica and found it to be dependent on the nature of the surface of mica. They obtained a value of about 0.17 J/m^2 for electro-neutral mica, 0.43 J/m^2 for electro-positive mica and 0.66 J/m^2 for electro-negative mica. Zong et al[73] used intercalated nano-particles between

graphene and SiO_2 substrate to determine the adhesion energy. The adhesion energy, which is found to be about 0.15 J/m^2, determines the radius of the blister formed by graphene membrane due to the presence of the nano-particle.

3. Pressurized Graphene Blisters

3.1 Introduction

The bulge test has been traditionally used to determine mechanical properties of thin films and membranes like elastic modulus, yield strength, fracture strength and residual stress.[74] It involves application of a pressure load on a thin suspended film/membrane clamped along its edges, the region over which the pressure is applied usually being circular. The resultant deformation, which appears like a "bulge", is measured and analyzed with the help of a model to obtain the film's mechanical properties. The blister test on the other hand can be viewed upon as an extension of bulge test which is used for measuring adhesion energy between thin films/membranes and substrates[75,76] (hereafter the words thin film and membrane are used interchangeably). Here, the edges of the membrane are 'clamped' by an adhesive or by adhesive interactions with the substrate. The applied pressure load initially deforms the membrane which is being clamped (through the adhesive or adhesive interactions) just as in the bulge test, but at a critical pressure the adhesive bond breaks and the membrane forms what is known as a "blister". The measurement of the blister area and the deformation gives the adhesion energy, again with the help of a suitable model for the membrane mechanics and material behavior as well as the adhesive or adhesive interactions.

Conventionally, the blister test is carried out at a prescribed pressure. The deformation caused by this prescribed pressure gradually increases with increasing magnitude of the pressure and at a critical pressure the membrane is blown off due to unstable delamination.[76] A stable alternative was achieved by Wan and Mai by using constant number of molecules of gas to pressurize the film.[77] In this constant N (number of gas atoms/molecules) blister test, a fixed mass

of gas is trapped in a cavity sealed by the membrane, the adhesion energy of which is to be measured. The pressure outside the cavity is decreased gradually which leads to a pressure differential across the membrane. This pressure differential deforms the membrane and the trapped gas expands isothermally. A stable delamination (or crack) is observed when the external pressure is decreased below a critical value. This stability is possible because the system equilibrates quickly to a stable configuration due to the limited number of gas atoms/molecules as opposed to the case in constant pressure blister tests.

In this chapter, the mechanics and thermodynamics of a constant N blister test on graphene membranes supported on silicon oxide (SiO_x) is described. The blister test set up used here has been independently devised by Steven Koenig and Prof. Scott Bunch of the University of Colorado at Boulder. It differs from Wan and Mai's setup[77] slightly in how the pressure load is applied to the graphene membrane. The adhesion energy between graphene and SiO_x substrate is determined along with stretching rigidity Et (E = Young's modulus, t = graphene membrane thickness) in this experiment.

3.2 Experiment

The experiment, performed by Steven Koenig, involves exfoliated graphene membranes of varying number of layers on a silicon chip with a thermally grown oxide layer. Micro-cavities of fixed dimensions, cylindrical in shape are lithographically patterned onto the chip before exfoliation. These micro-cavities form traps for gas molecules (N_2 in this case) when covered with graphene membranes. They are "charged" inside a pressure chamber where the micro-cavities are filled with gas molecules at a prescribed input or charging pressure, p_0 (which is higher than the atmospheric pressure, p_a). This charging process takes advantage of the diffusion of gas molecules through the thermal oxide layer between graphene and silicon.[22] Once equilibrium is reached, the

pressure of the trapped gas in the micro-cavities should increase from the atmospheric pressure, p_a at the time of exfoliation to the charging pressure, p_0 (Fig. 3.1b). It takes about a week to achieve equilibration after which the pressure outside the micro-cavities is brought down to p_a. This leads to expansion of the trapped gas presumably in an isothermal manner until the trapped gas reaches an equilibrium pressure, p_i. If the input pressure, p_0 is below a critical value $p_{0,c}$, the graphene membrane deforms to form a bulge as shown in Fig. 3.1c; else when p_0 is above $p_{0,c}$, blister formation is seen where the membrane is not only deformed but it also delaminates from the substrate (Fig. 3.1d). The resultant deformation is measured using an atomic force microscope (AFM). The process is repeated several times at different values of p_0, for several devices with the number of layers in the graphene membranes ranging from 1 to 5 as shown in the optical image (Fig. 3.1a).
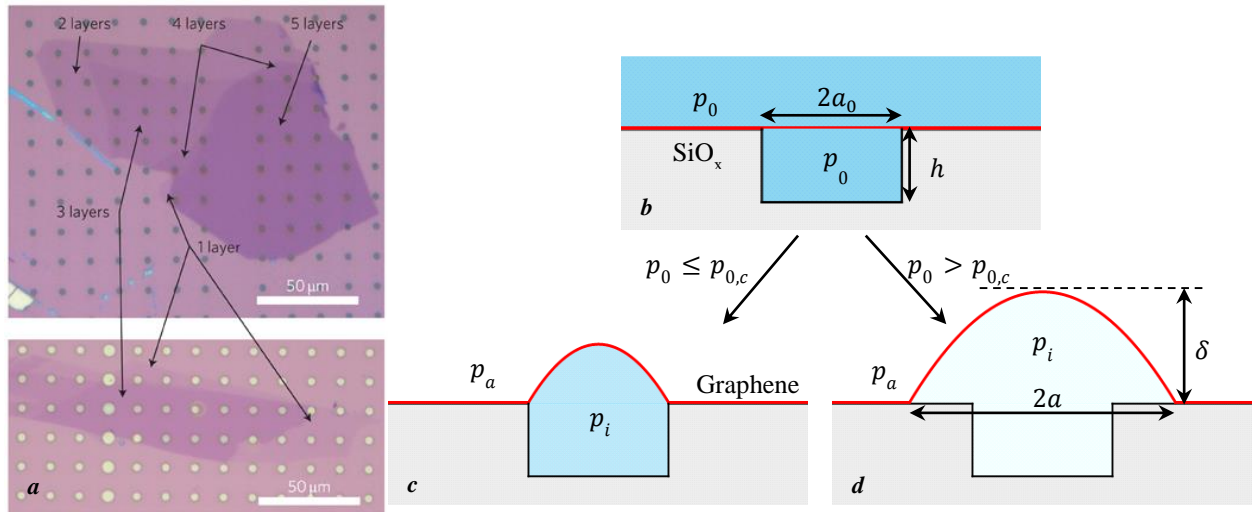
Figure 3.1 (a) Optical image of the devices covered with different layers of graphene, (b) Schematic of the cross section of a device charged to a pressure p_0 in a pressure chamber – the blue color indicates gas, the red curve is the graphene membrane, (c) Schematic illustrating the deformation of the graphene membrane due to the expanding gas molecules to form a bulge without delamination, (d) Formation of a blister is seen if the charging pressure is greater than the critical charging pressure, $p_{0,c}$ (Change of the blue color from darker to lighter shade indicates decreasing pressure)

The time during which each measurement is done is small compared to the time taken for the diffusion processes associated with charging and discharging of the micro-cavities,[22] so we can assume that the number of molecules inside the cavity remains the same throughout. Hence this can be viewed upon as a constant N blister test. The graphene membranes adhere to the substrate (SiO$_x$) via a variety of possible surface interactions like van der Waals forces, electrostatic forces, capillary forces, chemical bonds etc. The aim of the experiment is to determine statistically the strength of this adhesion.

3.3 Theory

Here, we develop an analytical model to describe the aforementioned experiment. The analytical model involves description of the mechanics of the graphene membrane coupled with the thermodynamics of the trapped gas and the membrane-substrate interfacial interactions. We consider the graphene membrane, the trapped gas and interfacial interactions as a thermodynamic system. Our approach is to then develop a thermodynamic free energy for the system while modeling the gas as ideal, the substrate-graphene adhesion energy to be uniform and adopting a nonlinear membrane model to describe graphene mechanics. We then minimize this free energy with respect to the unknown system parameters revealing the underlying relationship tying various system parameters which include the mechanical properties of graphene, adhesion energy, geometry of the micro-cavities and the charging pressure. We also contrast this analysis with that of a constant P blister test to note the differences between constant P and constant N blister tests.

3.3.1   Mechanics of Pressurized Graphene

The pressurized graphene sheets in this experiment can be looked at as an axisymmetric circular membrane clamped along its circumference by the adhesive forces. The mechanics of the such pressurized membranes (of radius a) are well described by the membrane equations, which

can be obtained from the more general Foppl-Von Karman (FvK) plate equations by neglecting the terms with bending rigidity, D.[51] The equations give a relationship between the membrane stresses and the applied pressure load:

$$N_r \frac{dw}{dr} = \frac{pr}{2}$$
$$N_t = \frac{d(rN_r)}{dr}$$

(3.1)

Here, r is the radial coordinate, p is the pressure load acting on the membrane, and w is the deflection. N_r and N_t are radial and tangential components of the membrane stress respectively. The membrane stresses are related to their respective membrane strains ϵ_r and ϵ_t through (u is the radial displacement):

$$\epsilon_r = \frac{1}{Et}(N_r - vN_t) = \frac{du}{dr} + \frac{1}{2}\left(\frac{dw}{dr}\right)^2$$
$$\epsilon_t = \frac{1}{Et}(N_t - vN_r) = \frac{u}{r}$$

(3.2)

Equations (3.1) and (3.2) can be reduced to one single equation in N_r given by:

$$N_r^2 \frac{d}{dr}\left(r^3 \frac{dN_r}{dr}\right) = -\frac{Etp^2}{8}r^3$$

(3.3)

A series solution to this equation is given by Hencky[53,57] for clamped circular membranes. He assumed that the solution to this equation is given by:

$$N_r = \left(\frac{Etp^2a^2}{64}\right)^{\frac{1}{3}} \sum_{n=0}^{\infty} A_{2n}\left(\frac{r}{a}\right)^{2n}$$

(3.4)

(a = radius of the circular region of the membrane being pressurized, $A_{2n} = \text{n}^{\text{th}}$ coefficient)

Putting this in eq. (3.3) and equating terms on the left hand side with those on the right hand side in the resultant algebraic equation, he got $A_2 = -A_0^{-2}, A_4 = -\frac{2}{3}A_0^{-5}, A_6 = -\frac{13}{18}A_0^{-8}$ etc. The clamped boundary condition of $u = 0$ at $r = a$ gives A_0. Hencky truncated the series to 7 terms to obtain an approximation for A_0. We used 13 terms ($n = 12$) and obtained a value of $A_0 = 1.668$ with Poisson's ratio, $\nu = 0.16$. Once an approximate description of the radial stress is obtained, it is easy to obtain the deflection profile and the maximum deflection:

$$w(r) = \int_r^a \frac{p\rho}{2N_r(\rho)} d\rho$$
$$\delta = w(r = 0) = C_2 \left(\frac{pa^4}{Et}\right)^{\frac{1}{3}}$$

(3.5)

Here, δ is the maximum deflection and $C_2(\nu = 0.16) = 0.6863$ is a pre-factor dependent on ν. Similarly we can also get the volume of the bulge, V_b:

$$V_b = \int_0^a 2\pi r w(r) dr = C_1 \pi a^2 \delta$$

(3.6)

$C_1(\nu = 0.16) = 0.5245$ is also a pre-factor similar to C_2. This solution is applicable to membranes whether they are delaminating or not as in each case the membrane is assumed to be clamped to the substrate through adhesive interactions.

We note here that Hencky's solution is for a uniform lateral loading which is not exactly the same as that of a uniformly pressurized membrane. Fichter treated the latter case and noted that the difference is only appreciable for very large loads. In view of this, we neglected the small difference between these two cases and adopted Hencky's solution for our purposes. Furthermore, Hencky's analysis does not include any pre-stress in the membrane. Campbell[54] extended Hencky's solution to include pre-tension (N_0) and noted that when the non-dimensional parameter

$P = (pa/Et)(Et/N_0)^{\frac{3}{2}} > 100$, the maximum deflection given by Hencky's solution is within 5% of the value given by Campbell's solution. Mechanically exfoliated graphene membranes are known to have pre-stresses in the range of 0.03 and 0.15 N/m with the average value being 0.07 N/m.[22,78,79] With values of $a = 2$ μm, $Et = 340$ N/m and $N_0 = 0.07$ N/m, that are typical to our experiment we can show that Campbell's parameter is about 100 when $p = 500$ kPa. Later, it will be seen that the majority of our measurements are well above this pressure and hence we neglect any effects of pre-stress in our analysis.

3.3.2 Thermodynamics of the Blister test

We now formulate the thermodynamic free energy, $\mathcal{F}$ of the system comprising of pressurized membrane, trapped gas and the membrane-substrate interface. This free energy captures the change in the energy of the system between the initial equilibrium state to the final equilibrium state. In the initial equilibrium state the membrane is flat and the pressure inside and outside the cavity is equal to p_0. In the final equilibrium state, the gas has isothermally expanded to deform the membrane into a near spherical cap shape with or without delamination as the pressure outside the cavity is brought down to the ambient pressure, p_a for the constant N blister test; while for the constant P case, the membrane is deformed in a similar manner except the pressure stays the same. The free energy, $\mathcal{F}$ can be written as:

$$\mathcal{F} = \mathcal{F}_{mem} + \mathcal{F}_{gas} + \mathcal{F}_{ext} + \mathcal{F}_{adh} \tag{3.7}$$

Here $\mathcal{F}_{mem}$ is the strain energy stored in the deformed membrane, $\mathcal{F}_{gas}$ is the work done by the pressurized gas on the membrane, $\mathcal{F}_{ext}$ is the work done in displacing the ambient which is held at a constant pressure, p_a and $\mathcal{F}_{adh}$ is the work done in delaminating the membrane from the substrate.

The membrane strain energy can be obtained by calculating the work done by the pressure load, $p = p_i - p_a$ at a fixed blister radius, a. Hence:

$$\mathcal{F}_{mem} = \iint N_i d\epsilon_i dA = \int p dV_b \,|_{\,a} = \frac{pV_b}{4} = \begin{cases} \dfrac{(p_0 - p_a)V_b}{4} & const\ P \\[2mm] \dfrac{(p_i - p_a)V_b}{4} & const\ N \end{cases} \tag{3.8}$$

The free energy contribution of the work done by the gas going from the initial state (p_0, V_0) to the final state $((p_i, V_0 + V_b) - $ constant N, $(p_0, V_0 + V_b) - $ constant P) is given by:

$$\mathcal{F}_{gas} = -\int p_i dV = \begin{cases} -p_0 V_b & const\ P \\[2mm] -p_0 V_0 \ln\left[\dfrac{V_0 + V_b}{V_0}\right] & const\ N \end{cases} \tag{3.9}$$

Here $V_0 = \pi h a_0^2$ is the volume of the micro-cavity, h being the depth of the cavity. In the constant P case, the work done is simply the applied pressure times the change in volume. While in the constant N case, $\mathcal{F}_{gas}$ is the isothermal work done by the trapped gas initially at a pressure p_0 and volume V_0 expanding to pressure p_i and volume $V_0 + V_b$. The work done on displacing a volume of the ambient gas equal to the blister/bulge volume should also be accounted for and is equal to:

$$\mathcal{F}_{ext} = \int p_a dV = p_a V_b \tag{3.10}$$

And the adhesion energy is given by:

$$\mathcal{F}_{adh} = \Gamma \pi (a^2 - a_0^2) \tag{3.11}$$

Here Γ is the adhesion energy per unit area, a property of the interface.

In the constant P case, among the parameters in the overall free energy expression, p_0, V_0, p_a and a_0 are known; while a and δ are unknown. When we use Hencky's relation as obtained in eq. (3.5) which relates a and δ at a given pressure p_0, the free energy then depends only on a.

While in the constant N case, p_i is an additional unknown. Since the trapped gas expands isothermally we have from the ideal gas law:

$$p_i(V_0 + V_b) = p_0 V_0 \tag{3.12}$$

Hence, again as in the constant P case, the overall free energy $\mathcal{F}$ can be expressed solely as a function of a. Finally, the total free energy is given by:

$$\mathcal{F}(a) = \begin{cases} \dfrac{pV_b}{4} - p_0 V_b + p_a V_b + \Gamma \pi (a^2 - a_0^2) & const\ P \\[2em] \dfrac{pV_b}{4} - p_0 V_0 \ln\left[\dfrac{V_0 + V_b}{V_0}\right] + p_a V_b + \Gamma \pi (a^2 - a_0^2) & const\ N \end{cases} \tag{3.13}$$

3.3.3 Equilibrium Conditions

The system equilibrium configurations can be found by looking at the extrema of the free energy, $\mathcal{F}(a)$. Hence we solve the equation:

$$\frac{d\mathcal{F}(a)}{da} = 0 \tag{3.14}$$

In the constant P case, this means:

$$\frac{d\mathcal{F}(a)}{da} = -\frac{3p}{4}\frac{dV_b}{da} + 2\pi \Gamma a = 0 \tag{3.15}$$

$$\Gamma = \frac{5C_1}{4} p\delta = \frac{5C_1 C_2}{4}\left(\frac{p^4 a^4}{Et}\right)^{\frac{1}{3}} \tag{3.16}$$

The eq. (3.16) tells us that for a given value of Γ and $a = a_0$, there is a critical pressure load, p_c given by:

$$p_c = \frac{1}{a_0}\left(\left(\frac{4\Gamma}{5C_1 C_2}\right)^3 Et\right)^{\frac{1}{4}} \tag{3.17}$$

Below this pressure eq. (3.14) has no solutions, hence there will be no delamination and the membrane mechanics is entirely described by Hencky's solution. At or above this pressure, there will be delamination. A more detailed explanation with an example follows later in the next section. The stability of this equilibrium configuration can be determined by the second derivative of $\mathcal{F}$ at this extremum:

$$\frac{d^2\mathcal{F}(a)}{da^2}\Big|_{p=p_c} = -\frac{8\pi\Gamma}{3} < 0 \tag{3.18}$$

This suggests that the equilibrium is unstable and leads to a catastrophic crack growth. This limits the ability to repeat the experiment on a membrane sample above p_c. However in the constant N case:

$$\frac{d\mathcal{F}(a)}{da} = -\frac{3p}{4}\frac{dV_b}{da} + \frac{V_b}{4}\frac{dp}{da} + 2\pi\Gamma a = 0 \tag{3.19}$$

and $p\ (= p_i - p_a)$ depends on a through the relation:

$$a = \left(\frac{p_0}{p_i} - 1\right)^{\frac{3}{10}} \left(\frac{V_0}{\pi C_1 C_2}\right)^{\frac{3}{10}} \left(\frac{Et}{p}\right)^{\frac{1}{10}} \tag{3.20}$$

Using eqs. (3.5) and (3.6), we can write that:

$$\frac{dV_b}{da} = \frac{\partial V_b}{\partial p}\Big|_a \frac{\partial p}{\partial a} + \frac{\partial V_b}{\partial a}\Big|_p = \frac{1}{3}\frac{V_b}{p}\frac{\partial p}{\partial a} + \frac{\partial V_b}{\partial a}\Big|_p \tag{3.21}$$

Putting this in eq. (3.19) gives:

$$\frac{d\mathcal{F}(a)}{da} = -\frac{3p}{4}\frac{\partial V_b}{\partial a}\Big|_p + 2\pi\Gamma a = 0 \tag{3.22}$$

This is similar to the result obtained from the constant P case except that p now is not a constant. Hence combining the result in eq. (3.22) with the ideal gas eq. (3.12) we get:

$$\Gamma = \frac{5C_1}{4}\left(\frac{p_0 V_0}{V_0 + V_b(a)} - p_a\right)\delta(a) \tag{3.23}$$

Putting $a = a_0$ in the above equation and solving for p_0 gives the critical input pressure, $p_{0,c}$ at which the membrane starts delamination. The second derivative at the equilibrium configuration is given by:

$$\frac{d^2\mathcal{F}}{da^2}\bigg|_{p=p_{0,c}} = \frac{10pV_b}{a^2}\left(\frac{2p_0 p_i - 3p_i^2 + p_0 p_a}{3p_0 p + p_i(p_0 - p_i)}\right) \tag{3.24}$$

The above expression is positive only if $p_i < 2p_0/3$ (assuming $p_a \ll p_i, p_0$). This inequality is same as saying $V_0 < 2V_b$ which can be satisfied easily by tailoring the geometry of the micro-cavity or sufficiently large p_0. Hence stable delamination is possible as opposed to the constant P case. This whole analysis in the constant N case can also be done regarding p or δ instead of a as the independent variable with the same results. But one noticeable difference when p is considered the independent variable, is that we can define a free energy before delamination begins:

$$\mathcal{F}_{bd}(p) = \frac{pV_b(p)}{4} - p_0 V_0 Log\left[\frac{V_0 + V_b(p)}{V_0}\right] + p_a V_b(p) \tag{3.25}$$

The extrema of this newly defined free energy gives a trivial solution which is the same as the eq. (3.5). Rather, the usefulness of this free energy is in helping visualize graphically the system behavior which will be discussed later in the next section.

The analysis gives us a relation through eq. (3.23), for the constant N case, between the known quantities (p_0, V_0), the measured quantities from the deformation (a, δ) and the unknown

quantity that the experiment is supposed to determine (Γ). Putting $a = a_0$ and rewriting the eq. (3.23), we get the critical charging pressure, $p_{0,c}$ as:

$$p_{0,c} = \left(\left(\frac{4\Gamma}{5C_1\delta(a_0)}\right) + p_a\right)\frac{V_0 + V_b(a_0)}{V_0} \tag{3.26}$$

We note that as $V_0 \rightarrow \infty$, $p_i = p_0V_0/(V_0 + V_b) \rightarrow p_0$ and $p_{0,c} \rightarrow p_c + p_a$ implying that the constant P blister test is a limiting case of the constant N blister test achieved by a large reservoir of trapped gas or equivalently a very large microcavity.

3.3.4   *System Behavior with Examples*

Before analyzing the experimental data, an effort is made to understand the effect of the system parameters a_0, h and Γ on the critical delamination pressure and the stability of the system through illustrative examples with $Et = 340$ N/m, $v = 0.16$, $a_0 = 2$ μm and $\Gamma = 0.2$ J/m². These are the four different scenarios we look at:

1. Constant P blister test

2. Constant N blister test with $h = 0.25$ μm

3. Constant N blister test with increased cavity radius ($a = 3$ μm) keeping $h = 0.25$ μm

4. Constant N blister test with increased cavity depth ($h = 1.25$ μm) keeping $a_0 = 2$ μm

Let us look at the first example - constant P blister test on monolayer graphene. According to the theory with the given parameters, the critical pressure load $p_c = 1.17$ MPa from eq. (3.17). The plots in Fig. 3.2 show the free energy, $\mathcal{F}$ as defined in the eq. (3.13) for constant P case at three different pressures – one below p_c, one exactly equal to p_c and one above it covering all the three possible scenarios. When $p < p_c$, from eq. (3.15) there is an equilibrium configuration at a value of $a > a_0$ and there is an energy barrier which keeps the system at $a = a_0$ implying no

blister formation. When $p \geq p_c$, the equilibrium shifts to a value of $a \leq a_0$ and the energy barrier vanishes. The system now has a favorable gradient as the blister radius increases, encouraging the membrane to completely delaminate. With finite sized membranes, this usually results in what experimentalists call "blow-off".[76] As shown in Fig. 3.2 the energy barrier is exactly equal to zero when $p = p_c$ and $\mathcal{F}$ has a maximum at $a = a_0$ along the black curve, consistent with the definition of p_c.
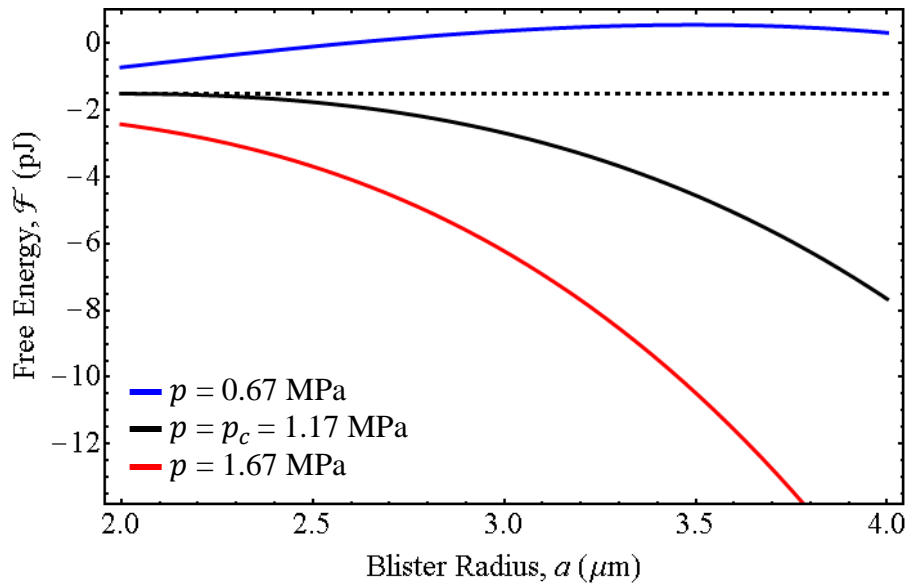
Figure 3.2 Plots showing the variation of free energy, $\mathcal{F}$ with blister radius, "a" at a fixed pressure load "p"

Now the second case - the constant N blister test with the same geometry, material and interfacial properties viz. $a_0 = 2$ μm, $Et = 340$ N/m, $\Gamma = 0.2$ J/m^2 and $V_0 \approx 3.14$ μm^3 ($h = 0.25$ μm). This geometry is very similar to that of the experimental devices used and the critical charging pressure $p_{0,c}$ is calculated to be 1.94 MPa from eq. (3.26) with $p_a = 83$ kPa. As before, the free energy is plotted as a function of the blister radius at three different input/charging pressures as shown in Fig. 3.3. The green and magenta colored points on the curves signify the initial configuration of the system and the final equilibrium configuration where $d\mathcal{F}/da = 0$ is

30

satisfied respectively. The dashed part of each curve corresponds to $a < a_0$ which is physically not realizable as opposed to the solid part. When $p_0 < p_{0,c}$ (blue curve), there is no equilibrium configuration to be found on the curve implying there will be no delamination and a remains equal to a_0. When $p_0 = p_{0,c}$ (black curve), the system finds an equilibrium configuration exactly at $a = a_0$, an inflection point. If p_0 is increased to a value beyond $p_{0,c}$ this unique equilibrium configuration splits into two equilibrium configurations – one local maximum to the left (not shown and unrealizable) and a local minimum to the right which is evident from the red curve in the Fig. 3.3. Thus when $p_0 > p_{0,c}$ (red curve), the system starts from the initial configuration denoted by green dot and moves to the minimum configuration denoted by the magenta dot. The presence of this minimum is what makes stable delamination possible in the constant N blister test.
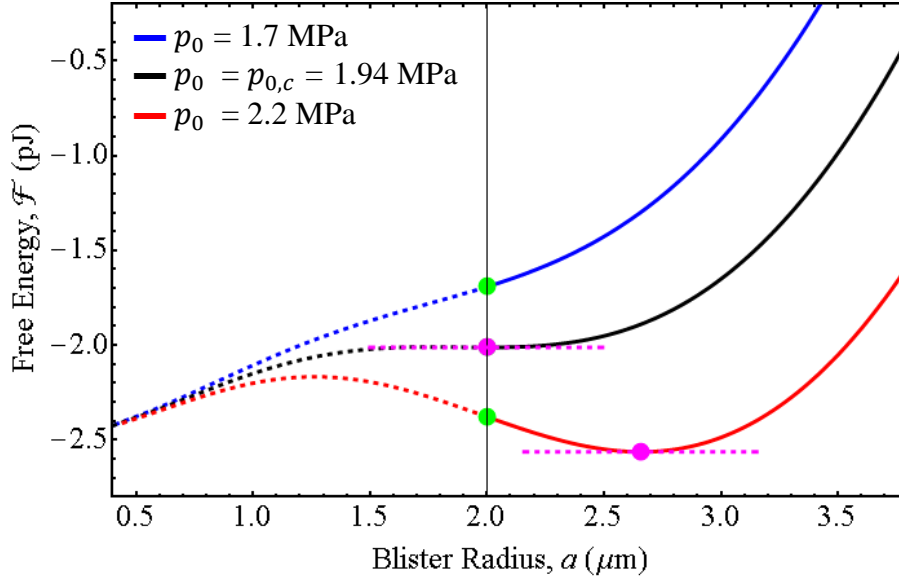
Figure 3.3 Plots showing the variation of free energy, $\mathcal{F}$ with blister radius, "a" at a fixed pressure "p" with $a_0 = 2 \ \mu m$ and $h = 0.25 \ \mu m$
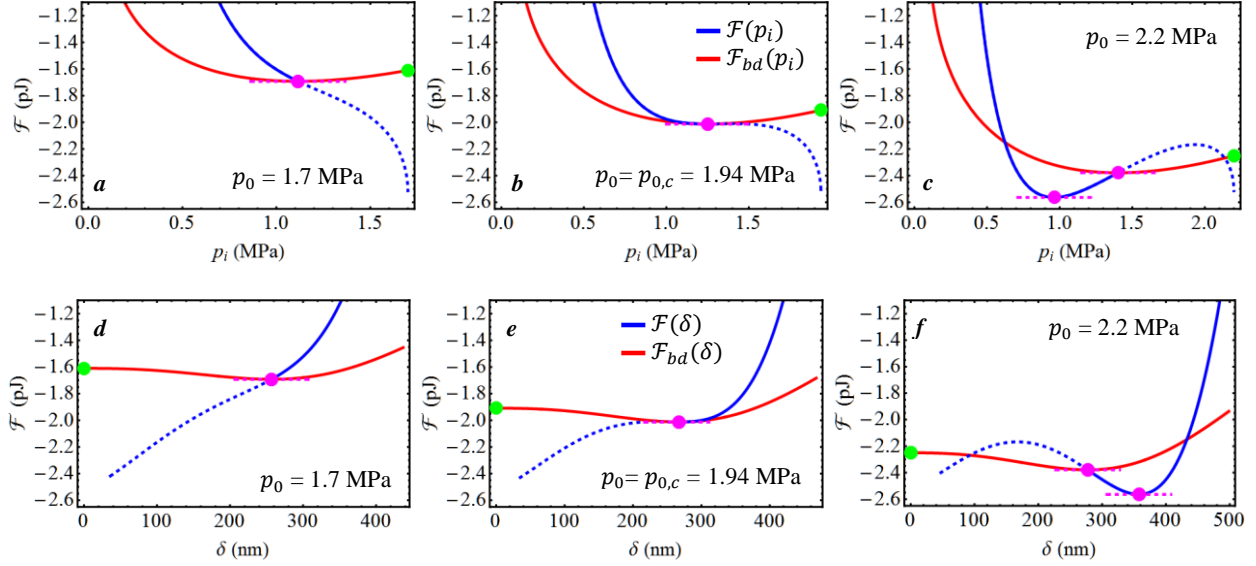
Figure 3.4 $\mathcal{F}$ vs p_i/δ and $\mathcal{F}_{bd}$ vs p_i/δ plots at different values of p_0 - the plots show initial configurations (green points) and possible equilibrium configuration (magenta dots) with $a_0 = 2\ \mu m$ and $h = 0.25\ \mu m$

The same exact conclusions can be drawn through plots of $\mathcal{F}(p_i)$ and $\mathcal{F}_{bd}(p_i)$ as shown in Fig. 3.4a-c. But this approach gives us a different perspective to the delamination phenomenon through the free energy defined for configurations before delamination, $\mathcal{F}_{bd}(p_i)$. The green and magenta points denote initial and equilibrium configurations as before. Since initially $a = a_0$ and there is no delamination yet, the initial configuration always lies on the $\mathcal{F}_{bd}$ curve. The dashed part of the $\mathcal{F}(p_i)$ curve is the equivalent of the $a < a_0$ part of $\mathcal{F}(a)$ and hence unrealizable. When $p_0 < p_{0,c}$ (Fig. 3.4a), $\mathcal{F}_{bd}(p_i)$ has a minimum as shown whereas there is none on $\mathcal{F}(p_i)$. Thus the system equilibrates to the point shown which is incidentally the point where the curves $\mathcal{F}_{bd}(p_i)$ and $\mathcal{F}(p_i)$ intersect and also the point where $a = a_0$ on $\mathcal{F}(p_i)$. When $p_0 = p_{0,c}$ (Fig. 3.4b), there is now an equilibrium configuration also on $\mathcal{F}(p_i)$ which is an inflection point and it coincides with that on $\mathcal{F}_{bd}(p_i)$. Increasing p_0 further such that $p_0 > p_{0,c}$ (Fig. 3.4c), the equilibrium point which was an inflection point splits into a maximum and a minimum. The maximum (not shown) as mentioned before is unrealizable and the system chooses the minimum of the minima on the

curves $\mathcal{F}(p_i)$ and $\mathcal{F}_{bd}(p_i)$. As shown in Fig. 3.4c, the minimum of the minima occurs on $\mathcal{F}(p_i)$ and hence we see delamination. The preceding discussion is also valid for $\mathcal{F}(\delta)$ and $\mathcal{F}_{bd}(\delta)$ as well and the corresponding plots are as shown in Figs. 3.4d-f.
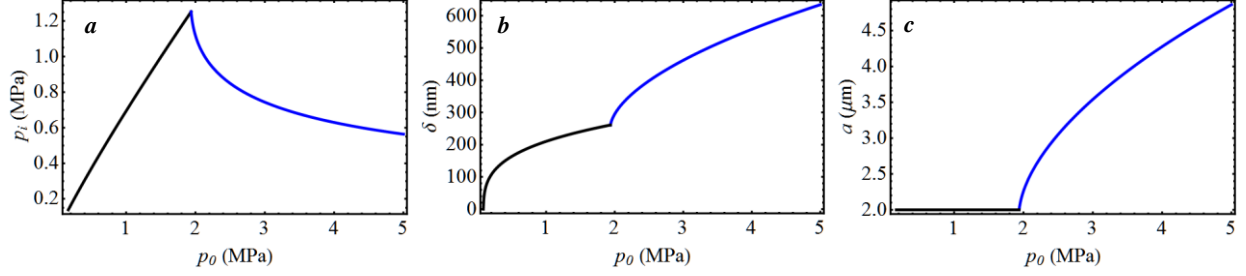
Figure 3.5 (a) Final Equilibrium pressure, p_i (b) Maximum Deflection and (c) Blister radius plotted as functions of the input pressure, p_0 with $a_0 = 2$ μm and $h = 0.25$ μm with the black and blue curves denoting the behavior pre and post-delamination respectively

From the equilibrium configurations thus obtained at each given charging pressure (p_0), we can then obtain the final equilibrium pressure (p_i), maximum deflection of the membrane (δ) and blister radius (a) as functions of input or charging pressures (p_0). They are shown in Fig. 3.5, with the behavior before and after delamination separated. Before delamination, p_i almost linearly increases with p_0 but after delamination it decreases exponentially with increasing p_0 (Fig. 3.5a). This can be attributed to the fact that after delamination the volume increases at a higher rate than before delamination, thereby decreasing the equilibrium pressure. Formally as the charging pressure becomes very large ($p_0 \rightarrow \infty$), the final equilibrium pressure reaches a limiting value of p_a ($p_i \rightarrow p_a$).

The deflection, δ increases initially and the membrane stiffens continuously; as delamination starts we see abrupt softening and stiffening continues again. The blister radius, while remaining constant until the critical charging pressure is reached, increases in an exponential manner.
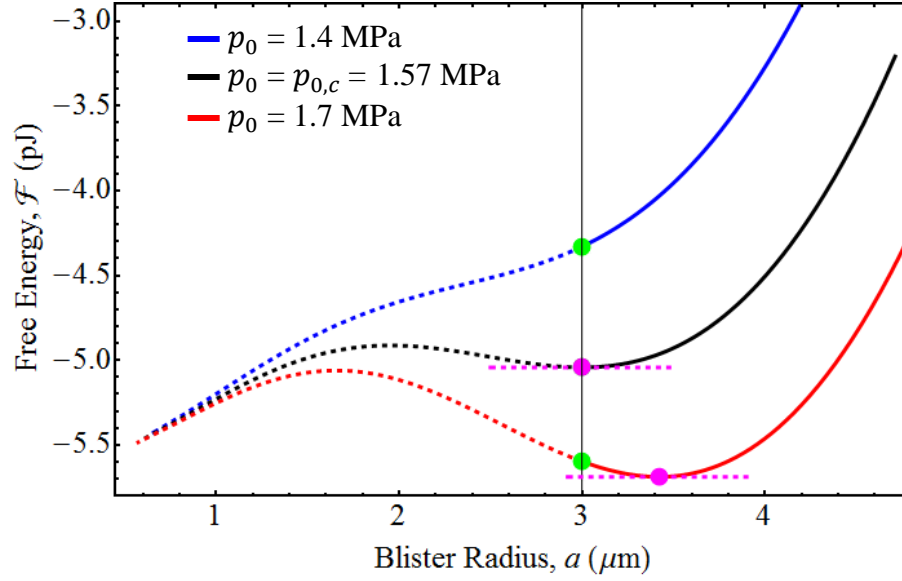
Figure 3.6 Plots showing the variation of free energy, $\mathcal{F}$ with blister radius, "a" at a fixed pressure "p" with $a_0 = 3$ μm and $h = 0.25$ μm0
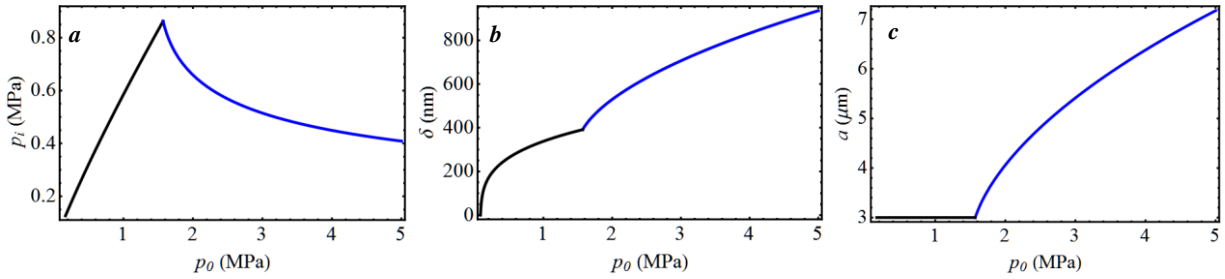
Figure 3.7 (a) Final Equilibrium pressure, p_i (b) Maximum Deflection and (c) Blister radius plotted as functions of the input pressure, p_0 with $a_0 = 3$ μm and $h = 0.25$ μm with the black and blue curves denoting the behavior pre and post-delamination respectively

In the third case we increase a_0 from 2 to 3 μm and see how this affects the system behavior. The critical input pressure is decreased from 1.94 MPa to 1.57 MPa as the membrane becomes more compliant. From the $\mathcal{F}(a)$ plots in Fig. 3.6, at the critical charging pressure the equilibrium now occurs at a minimum rather than at an inflection point. However, this does not affect the system behavior physically as observed in Fig. 3.7 and the system response looks similar to what we have when $a = 2$ μm.
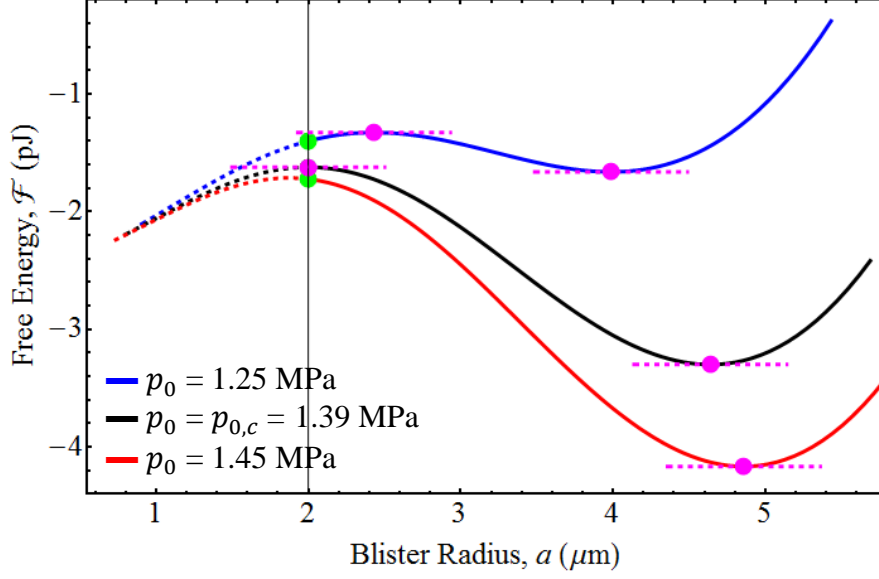
Figure 3.8 Plots showing the variation of free energy, $\mathcal{F}$ with blister radius, "a" at a fixed pressure "p" with $a_0 = 2\ \mu m$ and $h = 1.25\ \mu m$
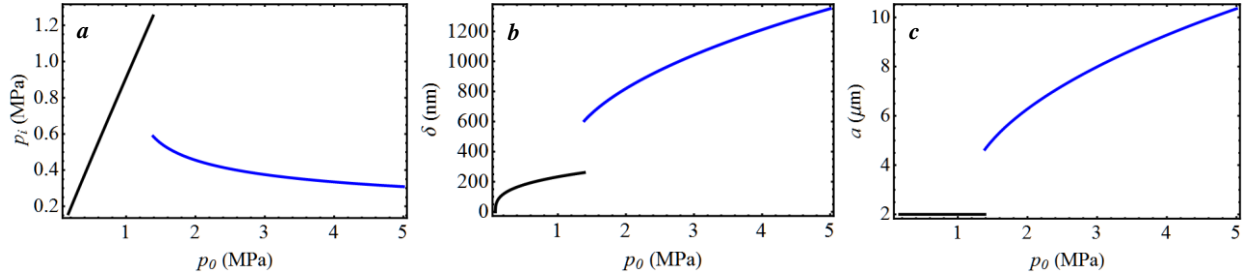
Figure 3.9 (a) Final Equilibrium pressure, p_i (b) Maximum Deflection, δ and (c) Blister radius, a plotted as functions of the input pressure, p_0 with $a_0 = 2\ \mu m$ and $h = 1.25\ \mu m$ with the black and blue curves denoting the behavior pre and post-delamination respectively

We have a different scenario in changing h from 0.25 to 1.25 μm and reverting back to a_0 = 2 μm. The critical charging pressure is again decreased from the original 1.94 MPa to 1.39 MPa. The plot of $\mathcal{F}(a)$ in Fig. 3.8 shows that now when $p_0 < p_{0,c}$ (blue curve), the curve has two possible extrema instead of none as in the previous two cases. But there is an energy barrier and so there is no delamination; but when $p_0 = p_{0,c}$ (black curve), the barrier is no longer there and the initial configuration coincides with a local maximum. This means we have an unstable equilibrium and with a small perturbation we can move the system from the maximum to the minimum available to the right of it accompanied by an abrupt delamination. This behavior is in

contrast to the previous two cases and Figs. 3.9a-c illustrate this. Close to the critical charging pressure as p_0 is increased, we have a discontinuity or "jump" in the system behavior.

In summary, we looked at constant N blister test with three different geometries. In each case, the equilibrium configuration at the critical charging pressure is located on an inflection point, a local minimum or a local maximum on $\mathcal{F}(a)$ respectively. What this suggests for the experiment is that in the first two cases we will see a steady, continuous change in the blister radius from a_0 as the membrane starts delaminating and likewise with p_i and δ. But in the third case due to the unstable maximum, there will be no continuous change but rather a "jump" in the observable/measured quantities of a, p_i and δ.
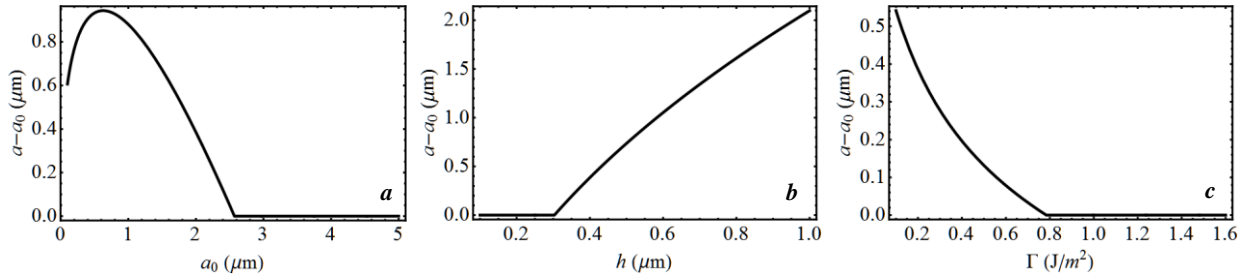
Figure 3.10 Variation of the degree of discontinuity or "jump", $a - a_0$ with respect to (a) Cavity Radius, a_0, (b) Cavity Depth, h and (c) Adhesion Energy, Γ with values of $a_0 = 2$ μm, $h = 0.4$ μm and $\Gamma = 0.2$ J/m^2 when not being varied

The degree of discontinuity or "jump" depends on the cavity geometry as well as the adhesion strength as shown in Figs. 3.10a-c. Values of $Et = 340$ N/m, $a_0 = 2$ μm, $h = 0.4$ μm and $\Gamma = 0.2$ J/m^2 are used when they are not being varied in these plots. It is interesting to see that in Fig. 3.10b, the jump monotonically increases with the cavity depth. This implies that with a finite sized membrane there will be complete delamination of the membrane when the cavity depth is very large. This is to be expected in light of our discussion at the end of the previous section where we concluded that as the cavity volume becomes very large we reach the limiting case of constant N blister test i.e. constant P blister test.

The "jump" is not seen at higher values of a_0 and Γ as shown in Figs 3.10a and 3.10c. It is to be noticed from Figs. 3.10a and 3.10b that increasing the radius and the depth of the cavity independently, both of which result in increasing the cavity volume, has a different effect on the system behavior. The same can be seen from Figs. 3.11a and 3.11b where the critical delamination pressure for constant P and constant N blister tests are plotted in black and red respectively. In Fig. 3.11a, we see that the critical delamination pressure for constant N blister test decreases with increasing cavity depth and reaches a limiting value which equals the delamination pressure for a constant P blister test. While in Fig. 3.11b, we see that the delamination pressure decreases monotonically for constant P case whereas the same for constant N case exhibits a curious behavior. The delamination pressure decreases initially with increasing cavity radius, reaches a minimum and then increases with increasing cavity radius for the constant N case. With increasing adhesion energy, the delamination pressure increases monotonically in both cases as shown in Fig. 3.11c.
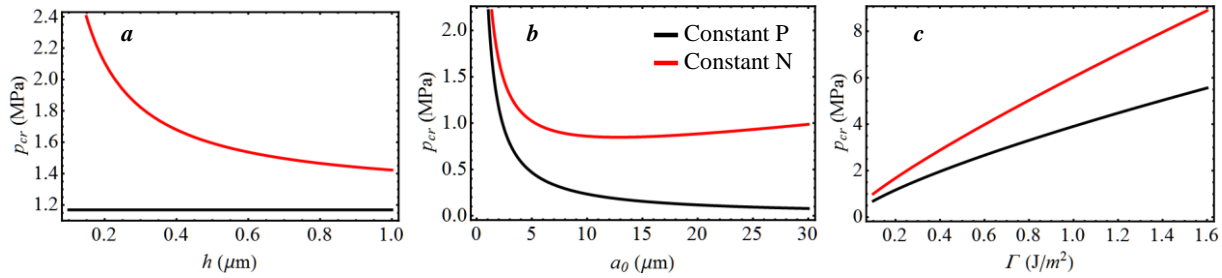
Figure 3.11 Variation of the critical delamination pressure ($p_c/p_{0,c}$) as a function of (a) Cavity Depth (b) Cavity Radius and (c) Adhesion Energy. When not being varied, $h = 400$ nm, $a_0 = 2$ μm and $\Gamma = 0.2$ J/m^2

3.4 Experimental Results
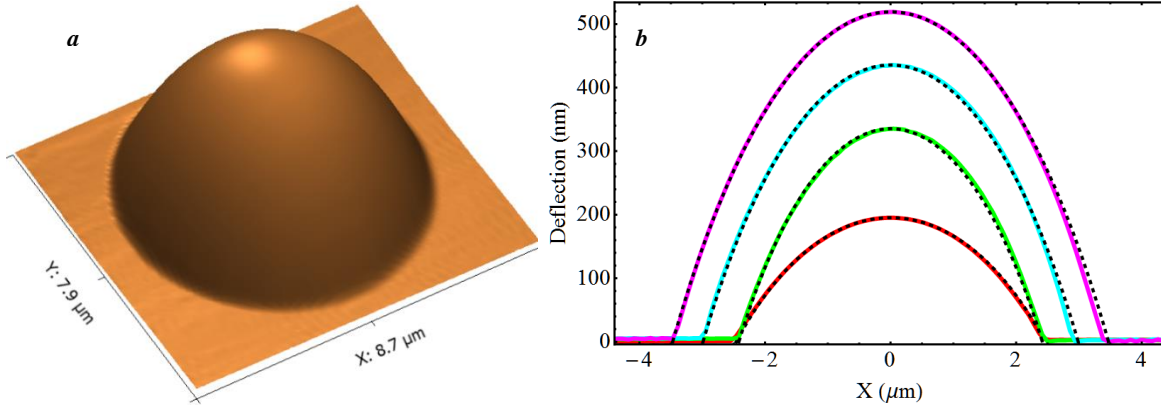
Figure 3.12 (a) Three dimensional rendering of the measured AFM Height data of a device at $p_0 = 2.4$ MPa on Chip C. The maximum height is about 520 nm. (b) AFM image cross sections of a device at different input pressures – 0.48 MPa (red), 1.32 MPa (green), 1.83 MPa (cyan) and 2.4 MPa (magenta). The black dashed curves are the deflection profiles from Hencky's solution with the maximum deflection fit to the measured value.

With the help of the theory developed in the previous section, we analyzed the experimental data in a systematic manner to arrive at the membrane modulus and adhesion energy. We obtained data from three different chips all made using the same fabrication processes. Let us label them as chips – A, B and C. Chip A contained a large piece of graphene flake with the number of layers ranging from 2-5 exfoliated over cavities with radius, $a_0 = 2$ µm and depth, $h = 250$ nm. Chip B contained a graphene flake with both mono and tri-layer graphene with device dimensions $a_0 = 2.32$ µm and $h = 293$ nm (see Appendix A.1 for optical images), while chip C had monolayer graphene with device dimensions $a_0 = 2.55$ µm and $h = 290$ nm. Using the atomic force microscope (AFM) to measure the deformation, we get a full three dimensional height map as shown in Fig. 3.12a. As the deformation is axisymmetric, we just need the maximum deflection (δ) and the radius (a) to characterize the deformation and we just look at a cross section (see Fig. 3.12b) of the full 3D AFM image to get these values. The AFM cross sections (Fig. 3.12b) at different input pressures p_0 compare very well with the profile obtained from Hencky's solution

38

(black dashed curves), thus validating our choice of employing Hencky's solution to describe the

graphene bulge/blister mechanics.
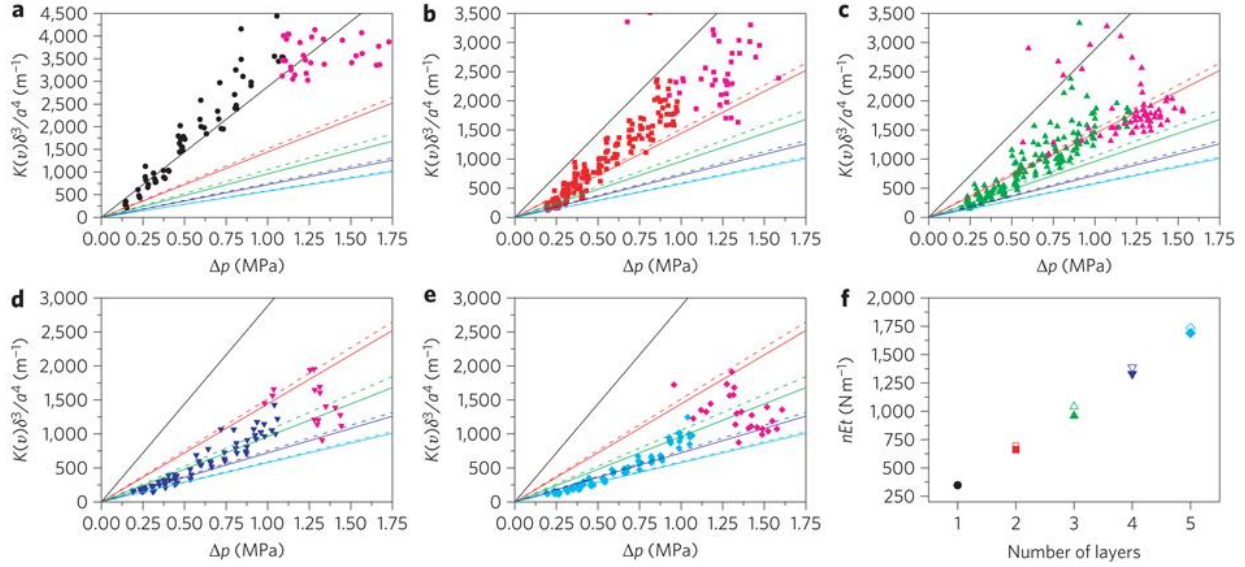
Figure 3.13 (a) $K(v)\delta^3/a^4$ vs p for monolayered graphene sheet before delamination (black symbols) and after delamination (magenta), (b)–(e) Same plots as (a) for two (red symbols, b), three (green, c), four (blue, d) or five (cyan, e) sheets of graphene before and after delamination (magenta symbols in all plots). The solid lines are linear fits to all the data with Et = 347 (black), 694 (red), 1,041 (green), 1,388 (blue) and 1,735 N m^{-1} (cyan). Dashed lines show linear fits to the data for $p < 0.50$ MPa and have slopes corresponding to Et = 661 (red; two layers), 950 (green; three layers), 1,330 (red; four layers) and 1,690 N/m (cyan; five layers). (f) Et versus number of layers. Solid symbols are fitted values; open symbols indicate number of layers times 347.

Combining eqs. (3.5) and (3.12), we get:

$$Et = K(v)\frac{\delta^3}{a^4}p = K(v)\frac{\delta^3}{a^4}\left(\frac{p_0 V_0}{V_0 + C_1(v)\pi a^2 \delta} - p_a\right)^{-1} \tag{3.27}$$

Here $K(v) = C_2(v)^{-3}$ and v=0.16. Having known the ambient pressure (p_a), charging pressure

(p_0) and cavity volume (V_0) and measured δ and a, we plotted $K(v)\delta^3/a^4$ against p and obtained

the best linear fit to determine Et in each case for the devices on Chips A and B. The results are

shown in Fig. 3.13a-e for 1-5 layered devices respectively. We got a value of $Et = 347$ N/m for 1

layered graphene which is in very good agreement with the established value 340 N/m. It is

expected that the value of Et for a n-layered graphene membrane varies as n times the value of the monolayered membrane. We found that our measurements confirm this behavior and the fitted values obtained for multi-layered graphene compare well with the expected linear scaling of Et with number of layers as shown in Fig. 3.13f. For the subsequent part of the experimental data analysis we used the values of Et thus obtained.
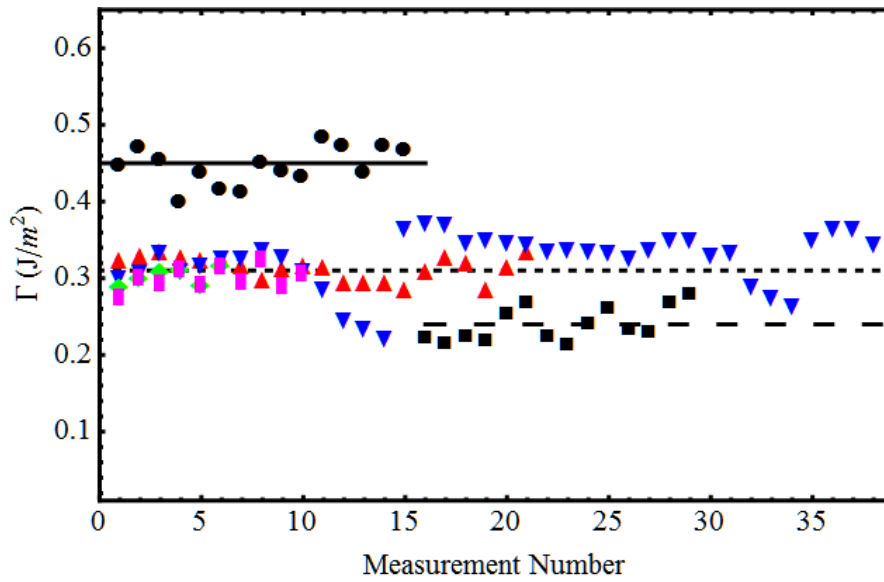
Figure 3.14 Measured adhesion energies Γ for membranes containing one layer of graphene (black circles & black squares), two layers (red triangles), three layers (blue inverted triangles), four layers (green diamonds) and five layers (magenta rectangles). The upper solid line corresponds to $\Gamma = 0.45\,J\,m^{-2}$, the lower dashed line corresponds to $\Gamma = 0.31\,J\,m^{-2}$ and the long dashed line corresponds to $\Gamma = 0.24\,J\,m^{-2}$.

We now proceed to finding the adhesion energy of the membranes using eqs. (3.6) and (3.23). The results are plotted in Fig. 3.14 for all the different layered membranes on the three chips. For 2-5 layered membranes, we got a mean value of 0.31 J/m^2 for the adhesion energy of multi-layered membranes on chips A and B whereas for the monolayered membranes we got values of 0.45 J/m^2 and 0.24 J/m^2 on chips B and C respectively. We plotted δ, a and p_i against p_0 as in Fig. 3.5 and compared with the theory in Figs. 3.15a, 3.15b and 3.15c respectively for two layered devices on chip A (we get similar results for other devices too, see Appendix A.1 for plots).

For the curves after delamination, we used three different values for Γ, 0.31 and 0.31$\pm$0.6 J/m^2. The experimental observations agree well with the $\Gamma = 0.31$ J/m^2 curve. It is to be noticed that not only the experimental data is self-consistent but also agrees very well with the theoretical predictions.
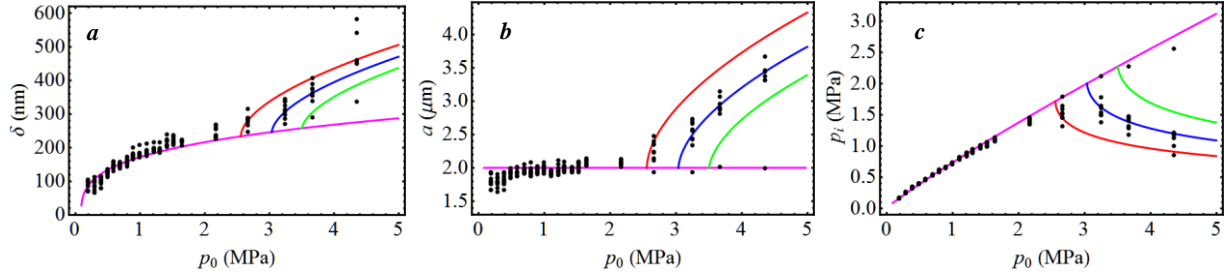
Figure 3.15 Plots showing maximum deflection δ (a), blister radius a (b) and final equilibrium pressure p_i (c) versus input pressure p_0 for all two-layer membranes studied. The magenta colored curve is the theoretical curve assuming no delamination of the membrane for $nEt = 661$ N m^{-1}, $n = 2$. Red, Blue and green curves are the theoretical curves for three different values of the graphene/SiO$_2$ adhesion energy Γ – 0.25, 0.31, 0.37 J/m^2 respectively.

As we discussed earlier, the theory predicts that when the cavity depth h is large, the blister test system may exhibit an unstable delamination with a jump in the system parameters, including the blister radius. We observed such behavior in tests with a geometry for the microcavities similar to the fourth case discussed in the previous section. Specifically, the geometry we used is a cavity of radius $a_0 = 2.2$ µm and depth $h = 5$ µm. We found that with increasing charging pressure p_0, graphene membranes bulge as previously described; but at about $p_0 = 2.8$ MPa, the membrane appears to undergo severe delamination resulting in an irregularly shaped blister that is very large and covers multiple microcavities (see Fig. 3.16). We think that this large blister is a consequence of the unstable delamination as predicted by theory as shown in Fig. 3.9c. Conceivably, the membrane delaminated over a large region, neighboring blisters coalesced, and formed a large irregularly shaped blister. Assuming the adhesion energy is between 0.2-0.4 J/m^2 and graphene is

8 layered, the predicted critical input pressure for delamination is between 1.90-3.15 MPa. This is in reasonable agreement with the experimental observation where delamination was observed at $p_0 = 2.8$ MPa, but not at a lower pressure of $p_0 = 2.2$ MPa. We did not do tests at pressures between these two values.
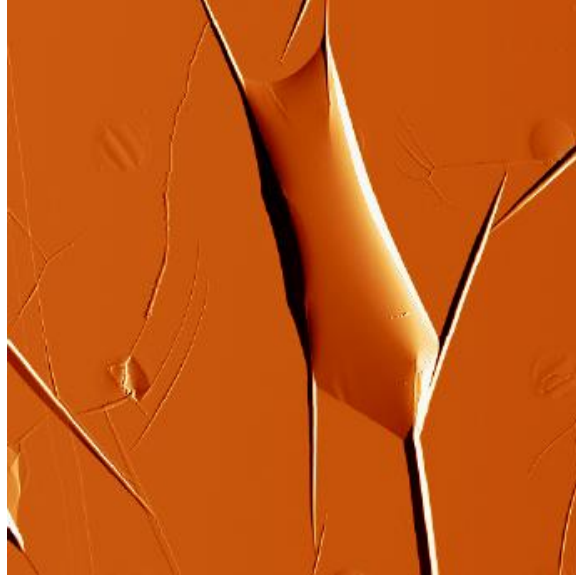
Figure 3.16 AFM amplitude image (40×40 μm) of a graphene membrane that has undergone large-scale delamination at $p_0 = 2.8$ MPa with $a_0 \approx 2.2$ μm and $h \approx 5$ μm.

3.5 Summary

We developed a theoretical model that couples mechanics and thermodynamics of a constant N blister test system comprising an elastic membrane adhered to a substrate while sealing away a micro-cavity filled with pressurized trapped gas under isothermal conditions. This system can be used to measure elastic modulus and adhesion energy between the membrane and the substrate by repeating the experiment with varying pressures i.e. changing the number of molecules N. The effect of various parameters in the system such as elastic modulus, micro-cavity geometry and adhesion energy are thoroughly explored and understood with the help of examples using experimentally accessible representative system parameters.

The theory is validated with experimental data obtained by Bunch group at University of Colorado, Boulder. The experiments use atomically thin graphene membranes on silicon oxide substrates. We used three different exfoliated graphene flakes on three different chips fabricated in the same manner with the number of graphene layers varying from 1-5. The experimental observations agree well with the theory and give an averaged value of 0.31 J/m^2 for adhesion energy for 2-5 layered graphene membranes. For monolayer graphene, on two different chips, we obtained adhesion energies of 0.44 J/m^2 and 0.24 J/m^2. The variation in the adhesion energies might be due to the variations in the properties of the substrate from chip to chip like surface morphology, reactivity, trapped charges etc. These variations in turn might be resulting from variations in the fabrication processes. We also illustrated, both analytically and experimentally, how deep cavities can lead to unstable growth of blisters ultimately leading to "blow-off".

Later we will study the effect of surface morphology on the adhesion energy of graphene membranes using simulations; while the effect on adhesion energy due to substrate chemical activity, trapped charges etc is beyond our scope.

4. Pressurized Graphene Island Blisters

4.1 Introduction

In this chapter, we describe a new type of pressurized graphene blister with switchable shapes controlled by pressure and adhesion. A similar geometry, but with a constant pressure loading, has been previously used in the island blister test (IBT) to measure the mechanical and adhesive properties of soft films[80,81] a few microns thick by Allen and Senturia. Here we adopt this geometry and modify it by using trapped gas with constant number of molecules instead of a constant pressure load, along the lines of a constant N standard blister test that was described in the previous chapter.
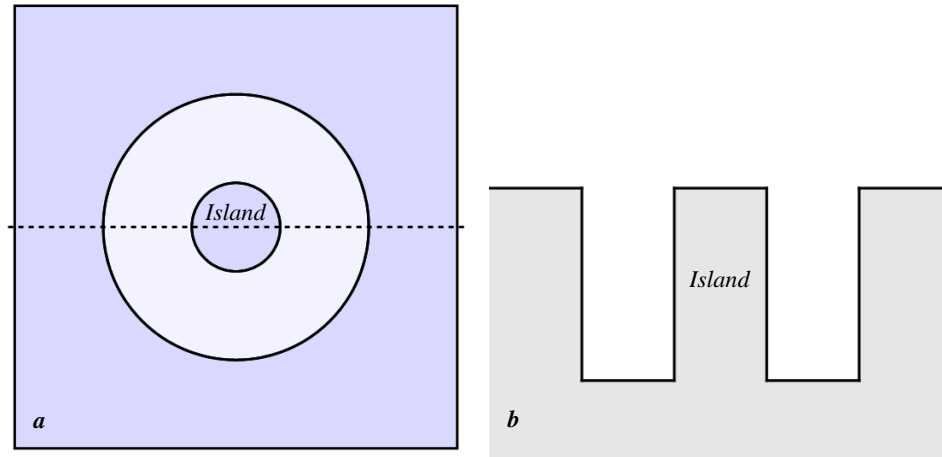
Figure 4.1 Constant N Island Blister Test Geometry (a) Top View (b) Cross-section View along the dashed line shown in (a).

The island blister test involves application of a pressure load across an annularly shaped suspended membrane, held fixed along the edges by adhesive interactions or an adhesive at the interface of the membrane and the substrate. The substrate in the middle of the annular region resembles an island and hence the name island blister test (see Fig. 4.1). As in the previous chapter, we extend the constant P IBT analysis to constant N IBT and validate it through experiments on

graphene membranes. The test was originally devised to overcome the problem of rupturing of low strength films with the stand blister test setup. In our case, the motivation for this study comes from the thought that this geometry with graphene membranes, with switchable shapes tuned and controlled by pressure and adhesion, might prove important for future graphene based nano-electromechanical devices.

4.2 Theory and Simulations
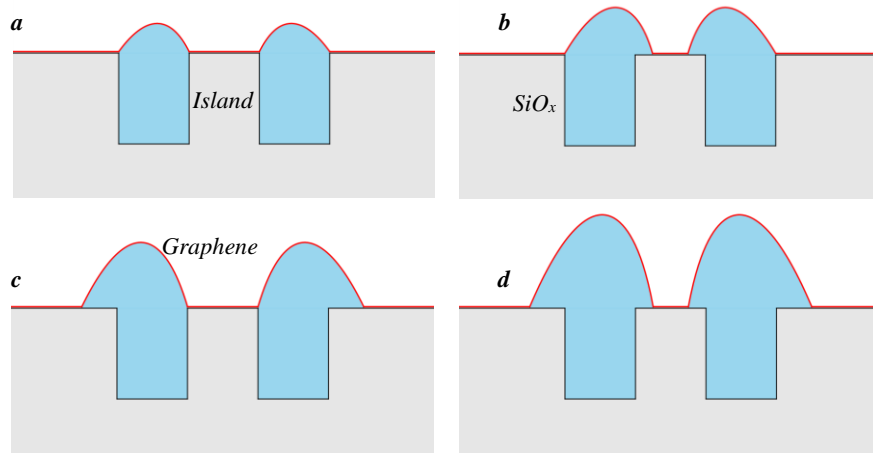
Figure 4.2 Schematics of different configurations possible in the island blister test (a) No delamination, (b) Inwards delamination only, (c) Outwards delamination only and (d) Inwards as well as outwards delamination

The constant N IBT experimental setup consists of cylindrical annular shaped micro-cavities in SiO_x substrate covered by graphene membranes. The graphene membranes adhere to the substrate via adhesive interactions possibly dominated by van der Waals interactions. The graphene membranes are fixed along the outer and inner boundaries of the annular suspended region due to these interactions. Upon pressure loading, there are four possible scenarios as shown in Fig. 4.2:

(a) The membrane deforms forming an annular bulge without delaminating either inwards or outwards.

(b) If the pressure load is high enough, the membrane starts delaminating but only inwards.

(c) The membrane starts delaminating only outwards.

(d) The membrane delaminates in both inward and outward directions.

To be able to predict which of these configurations are favored at a given pressure, we need to first understand the underlying mechanics of the annular bulge.

4.2.1 *Mechanics of Pressurized Annular Graphene*
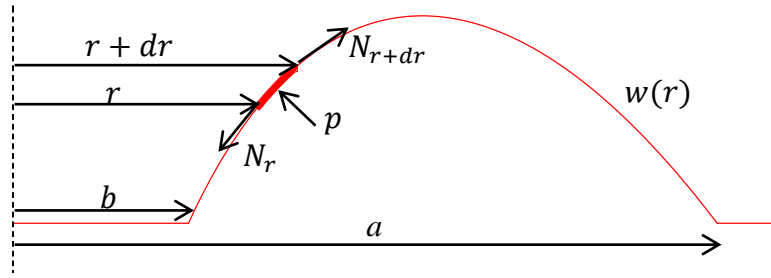
Figure 4.3 Schematic showing a ring element (thicker part of the curve) with the relevant forces

Let the deflection of an axisymmetric annular bulge with outer and inner radii a and b be denoted by $w(r)$, r being the radial coordinate in a cylindrical coordinate system. Let us now look at an infinitesimal ring element as shown in Fig. 4.3. The forces acting on this element are the force due to the pressure load (p), the radial membrane stresses (N_r and N_{r+dr}) along the edges of the ring in the tangential direction. The forces balance out in the radial direction due to symmetry and in the vertical direction we have:

$$N_{r+dr}\left(\frac{dw}{dr} + \frac{d^2w}{dr^2}dr\right)2\pi(r+dr) - N_r\frac{dw}{dr}2\pi r = -p2\pi rdr \tag{4.1}$$

$$N_{r+dr} = N_r + \frac{dN_r}{dr}dr$$

Here we assumed small rotations implying $\text{Sin}[\theta] \approx \text{Tan}[\theta] \approx dw/dr$. Neglecting the second order terms and simplifying eq. (4.1), we get:

$$N_r \frac{dw}{dr} dr + r N_r \frac{d^2 w}{dr^2} dr + r \frac{dN_r}{dr} \frac{dw}{dr} dr = pr dr$$

$$\Rightarrow \frac{d}{dr}\left(r N_r \frac{dw}{dr} \right) = pr \tag{4.2}$$

N_r is a function of r and it is related to its equivalent strain through eq. (3.2). A series solution like the Hencky's solution with the circular membrane is not possible in this case. Hence to obtain an approximate solution we assumed that the hoop strain is zero following Saif et al,[58] giving us $N_r = \nu N_t$ again from eq. (3.2). We also assumed that N_r is constant and denote it by S. Hence through simple integration of eq. (4.2) we get:

$$w = \frac{pr^2}{4S} + c_1 \ln[r] + c_2 \tag{4.3}$$

The integration constants c_1 and c_2 can be determined using the boundary conditions $w(r = a) = w(r = b) = 0$. Thus the membrane deflection profile $w(r)$ is given by:

$$w(r) = \frac{p}{4S}\left((a^2 - r^2) + r_0^2 \ln\left[\frac{r}{a}\right] \right) \tag{4.4}$$
$$r_0^2 = \frac{a^2 - b^2}{\ln[a/b]}$$

The maximum deflection H occurs at $r = r_0/\sqrt{2}$ and is given by:

$$H = w\left(r = r_0/\sqrt{2}\right) = \frac{p}{4S}\left(a^2 - \frac{r_0^2}{2} + \frac{r_0^2}{2}\ln\left[\frac{r_0^2}{2a^2}\right] \right) \tag{4.5}$$

And the volume of the annular bulge V_a is:

$$V_a = \int_b^a w\, 2\pi r dr = \frac{\pi}{2} \frac{p}{4S}(a^2 - b^2)(a^2 + b^2 - r_0^2) \tag{4.6}$$

The radial membrane stress S is still an unknown. To obtain S, we calculate the average radial strain weighted by the area:

$$\bar{\epsilon}_r = \frac{\int_b^a \frac{1}{2}\left(\frac{dw}{dr}\right)^2 2\pi r \, dr}{\int_b^a 2\pi r \, dr} = \frac{S(1-v^2)}{Et} \tag{4.7}$$

Substituting eq. (4.4) in eq. (4.7) and integrating we get:

$$S = \left(\frac{Etp^2}{16(1-v^2)}(a^2 + b^2 - r_0^2)\right)^{\frac{1}{3}} \tag{4.8}$$

Thus from eqs. (4.5) and (4.8), we can see that pressure is still non-linear and proportional to cube of the maximum deflection just as in the circular membrane case but the dependence on the geometrical parameters is much more involved.

4.2.2 Finite Element Simulations of Pressurized Annular Graphene

We assumed that the hoop strain (ϵ_t) is zero and used averaged radial strain (ϵ_r) to obtain an average measure for radial membrane stress (S). While our analysis follows that of Saif et al closely, they averaged the strain along the diameter whereas we averaged it over the entire area of the membrane. Williams[57] assumed equi-biaxial strain condition and obtained an areal average for the total strain – radial and tangential combined. The pressure-displacement relation obtained by us is:

$$H = \left(\frac{p(1-v^2)}{4Et}\right)^{\frac{1}{3}} \left(a^2 - \frac{r_0^2}{2} + \frac{r_0^2}{2} \ln\left[\frac{r_0^2}{2}\right]\right)(a^2 + b^2 - r_0^2)^{-\frac{1}{3}} \tag{4.9}$$

The expression obtained through Saif et al's approach is:

$$H = \left(\frac{p(1-v^2)}{8Et}\right)^{\frac{1}{3}} \left(a^2 - \frac{r_0^2}{2} + \frac{r_0^2}{2}\ln\left[\frac{r_0^2}{2}\right]\right) \left(\frac{a^2+b^2+ab}{3} + \frac{r_0^4}{4ab} - r_0^2\right)^{-\frac{1}{3}} \tag{4.10}$$

Finally the expression obtained Williams is:

$$H = \left(\frac{p(1-v)}{2Et}\right)^{\frac{1}{3}} \left(a^2 - \frac{r_0^2}{2} + \frac{r_0^2}{2}\ln\left[\frac{r_0^2}{2}\right]\right) (a^2 + b^2 - r_0^2)^{-\frac{1}{3}} \tag{4.11}$$

To determine which of the three above mentioned approaches give the best approximation we carried out finite element simulations, the details of which follow.

The finite element (FE) simulations are carried out using the software package Abaqus. We used an axisymmetric model with two different geometries - $a = 2$ µm and $b = 0.5$ or 1 µm. Two noded axisymmetric shell elements (SAX1) with thickness 0.34 nm are used to mesh the membrane to account for both bending and stretching of the membrane. Values of $E = 1$ TPa and $v = 0.16$ are used for material properties which correspond to those of graphene. The "pressure load versus maximum displacement" as well as the deflection profiles are plotted in Figs. 4.4a-c and Fig. 4.5a respectively.
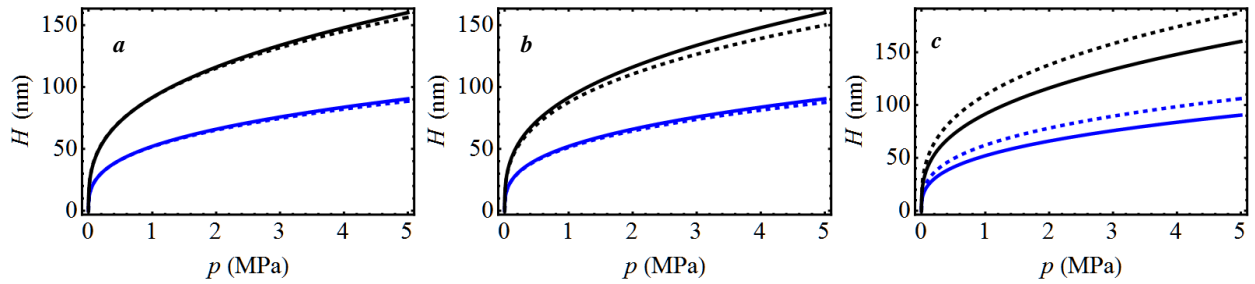
Figure 4.4 Comparison of the FE simulation results through the load, p v maximum deflection, H plots with the different analytical expressions (a) Current analysis (eq. (4.9)), (b) Saif et al's result (eq. (4.10)), (c) Williams' result (eq. (4.11)). In all the cases, the solid curves indicate FE results and the dashed curves the analytical expressions. Also, for the blue curves a = 2 µm, b = 1 µm and for black curves a = 2 µm, b = 0.5 µm with Et = 340 N/m and v = 0.16 in all the calculations.
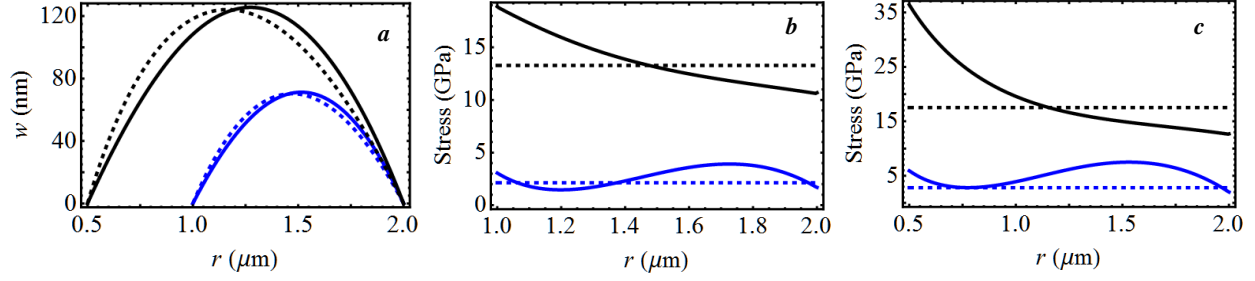
Figure 4.5 (a) Plots comparing the deflection profile at p ≈ 2.51 MPa as obtained from the analysis (eq. (4.4)) and FE (a = 2 μm, Blue – b = 1 μm, Black – b = 0.5 μm, Solid – FE, Dashed – Current Analysis), (b,c) Radial and Tangential stresses in black and blue colored solid curves respectively at p ≈ 2.51 MPa along the radius of the membrane with a = 2 μm and (b) b = 1 μm, (c) b = 0.5 μm. The black and blue dashed curves are the averaged radial and tangential stresses respectively calculated using the current analysis.

The overall load versus deflection response matches quite closely with our analytical result (as shown in Fig. 4.4a), better than with the other two possibilities. Hence we used eq. (4.9) to describe the mechanics of the annular bulge for the rest of the analysis. The figure 4.5a shows the deflection profile from our analysis (dashed curves) compared with the FE results at $p = 2.51$ MPa. We have a reasonably good description of the deflection profile from the theory, even though the radius at which the maximum deflection occurs is not in very good agreement with the FE results. The figures 4.5b and 4.5c show the stresses as obtained from the FE simulations at $p = 2.51$ MPa for the two different geometries ((b) $b = 1$ μm and (c) $b = 0.5$ μm). The average radial stress values in each case as calculated from the analysis are 13.29 GPa and 17.54 GPa respectively and are also shown as dashed lines. They are in good agreement with the averaged values for radial stresses calculated from the simulations – 13.24 GPa and 17.04 GPa respectively. The tangential stresses are also in good agreement and consistent with our assumption that the tangential strain is negligible. Also it is to be noted that the residual stress found in graphene membranes is usually of the order of 0.30 GPa which is small compared to the radial stresses we have here at about $p = 2$ MPa, thereby allowing us to neglect its effect. Even at $p = 100$ kPa, from eq. (4.8) the average radial stress is 1.55 GPa, which is still 5 times the typical values of residual stress in graphene.

4.2.3   Thermodynamics of the Island Blister test
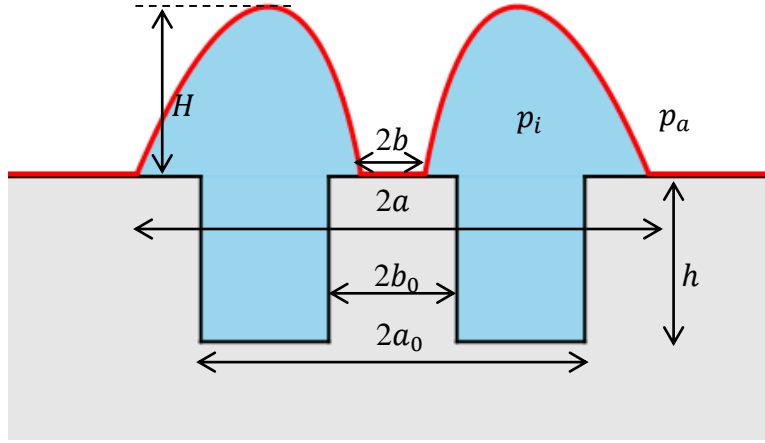
Figure 4.6 Schematic showing the most general blister configuration – blue color indicates gas molecules applying a pressure load on the graphene membrane (shown in red); graphene membrane is adhered to the substrate outside the cavity and on the island.

Now that we understand the mechanics of the annularly deformed membranes, we proceed to understand how delamination occurs at any given pressure load. Just as in the previous chapter, we formulate a thermodynamic free energy ($\mathcal{F}$) for the most general system configuration shown in Fig. 4.6 under constant P and constant N conditions. We determine the extrema of this free energy in order to determine the equilibrium configuration preferred by the system. The free energy as before has four components – membrane elastic strain energy ($\mathcal{F}_{mem}$), free energy due to the work done by gas ($\mathcal{F}_{gas}$), free energy associated with displacing the ambient as the membrane deforms ($\mathcal{F}_{ext}$) and finally the work of adhesion ($\mathcal{F}_{adh}$).

$$\mathcal{F} = \mathcal{F}_{mem} + \mathcal{F}_{gas} + \mathcal{F}_{ext} + \mathcal{F}_{adh} \tag{4.12}$$

As shown in Fig. 4.6, a_0, b_0 and h denote the annular cavity dimensions – outer radius, inner radius and depth, while the blister outer and inner radii are denoted by a and b. The maximum height of the blister is H. The pressure load across the membrane is $p = p_i - p_a$, where p_i is the

pressure inside the cavity and p_a is the ambient pressure outside the cavity. The membrane elastic

energy is equal to the work done by the gas at constant a and b. Hence:

$$\mathcal{F}_{mem} = \int pdV \,\big|_{a,b} = \frac{pV_a}{4} \tag{4.13}$$

where V_a is given by eq. (4.6). At constant a and b, it is easy to see from eq. (4.6) that V_a depends

only on H. Now, p is proportional to cube of H and hence integrating we get ¼ in the final result.

The work done by the gas is given by:

$$\mathcal{F}_{gas} = -\int p_i dV = \begin{cases} -p_0 V_a & const\ P \\ -p_0 V_0 \ln\left[\dfrac{V_0 + V_a}{V_0}\right] & const\ N \end{cases} \tag{4.14}$$

Here $p_0 = p + p_a$ in the constant P case and the initial charging pressure in the constant N case.

V_0 is the initial volume of the gas which is equal to the volume of the cavity, $\pi(a_0^2 - b_0^2)h$. Since

the applied pressure is constant by definition in the constant P case, the work done is simply given

by the product of absolute pressure and change in the volume of the gas. The work done in the

constant N case is obtained using the ideal gas law, $p_0 V_0 = p_i(V_0 + V_a)$ under isothermal

conditions. The work done on the ambient is simply the product of ambient pressure and the

volume by which the ambient is displaced ($= V_a$). This is because the ambient pressure remains

constant at p_a irrespective of whether it is constant P or constant N delamination. So:

$$\mathcal{F}_{ext} = p_a V_a \tag{4.15}$$

The free energy contribution through delamination is simply given by:

$$\mathcal{F}_{adh} = \Gamma_a \pi(a^2 - a_0^2) + \Gamma_b \pi(b_0^2 - b^2) \tag{4.16}$$

Here we assumed different adhesion energies between the membrane and the substrate outside the cavity and on the island. They are denoted by Γ_a and Γ_b respectively. So the final form of the total free energy is:

$$
\mathcal{F} = \begin{cases} -\dfrac{3pV_a}{4} + \Gamma_a\pi(a^2 - a_0^2) + \Gamma_b\pi(b_0^2 - b^2) & const\ P \\[2mm] \dfrac{pV_a}{4} - p_0V_0\ln\left[\dfrac{V_0 + V_a}{V_0}\right] + p_aV_a + \Gamma_a\pi(a^2 - a_0^2) + \Gamma_b\pi(b_0^2 - b^2) & const\ N \end{cases} \tag{4.17}
$$

In the constant P case, the unknown variables are H, a and b while the only independent variables are a and b due to the relation between H, a and b given by eq. (4.9). In the constant N case at a given p_0, the unknowns include H, a, b and p_i. With eqs. (4.6), (4.9) and the ideal gas equation p_i can be expressed in terms of a and b, giving:

$$
\left(\frac{p_0 - p_i}{p_i}\right)^3 V_0^3 = \frac{\pi^3(a^2 - b^2)^3(1 - v^2)}{32Et}\left(a^2 + b^2 - r_0^2\right)^2(p_i - p_a) \tag{4.18}
$$

Hence the unknowns H and p_i are both dependent on a and b. This shows that the independent variables are again a and b implying $\mathcal{F} = \mathcal{F}(a, b)$ in both constant N and constant P cases.

The free energy expression in eq. (4.17) refers to the most general system configuration where we have delamination in both outward and inward directions, as in Fig. 4.2d. Putting $a = a_0$ and $b = b_0$ in $\mathcal{F}(a, b)$, the free energy contribution of the adhesion energy vanishes and the configuration then corresponds to Fig. 4.2a, no delamination in either outward or inward directions making $\mathcal{F} = \mathcal{F}(H)$. By extension, fixing either $a = a_0$ or $b = b_0$ in $\mathcal{F}(a, b)$ corresponds to the configuration in Figs. 4.2b and 4.2c, delamination inwards and outwards respectively making $\mathcal{F} = \mathcal{F}(b)$ and $\mathcal{F} = \mathcal{F}(a)$.

4.2.4 Equilibrium Conditions

In the case of no delamination in either outward or inward direction, the extremum of the free energy $\mathcal{F}(H)$ gives a trivial solution which is the same as the eq. (4.5). In other cases, the equilibrium configuration is obtained by looking at the extrema/extremum of the free energy $\mathcal{F}(a, b)$ as represented in eq. (4.17). Let us first look at the constant P case:

$$\frac{\partial \mathcal{F}(a,b)}{\partial a} = -\frac{3p}{4}\frac{\partial V_a}{\partial a} + \Gamma_a 2\pi a = 0$$
$$\frac{\partial \mathcal{F}(a,b)}{\partial b} = -\frac{3p}{4}\frac{\partial V_a}{\partial b} - \Gamma_b 2\pi b = 0$$

(4.19)

Solving eq. (4.19) leads to the following equations:

$$\Gamma_a = \frac{p}{8}\left(\frac{p(1-v^2)}{4Et}\right)^{\frac{1}{3}}\frac{5a^4 + a^2 b^2 - 5a^2 r_0^2 + r_0^4}{a^2(a^2 + b^2 - r_0^2)^{\frac{1}{3}}}$$

(4.20)

$$\Gamma_b = \frac{p}{8}\left(\frac{p(1-v^2)}{4Et}\right)^{\frac{1}{3}}\frac{5b^4 + a^2 b^2 - 5b^2 r_0^2 + r_0^4}{b^2(a^2 + b^2 - r_0^2)^{\frac{1}{3}}}$$

(4.21)

Let $\Gamma_a = \Gamma_b$ for this part of the analysis. At a given pressure load p, it can be shown that the eqs. (4.20) and (4.21) are simultaneously satisfied only when $a = b$. The condition $a = b$ is not feasible implying that there cannot be simultaneous outward and inward delamination. So, the delamination has to begin exclusively in either outward or inward direction. Putting $a = a_0$ in eq. (4.21) gives the condition for equilibrium configuration when peeling occurs on the island i.e. inward direction. Likewise putting $b = b_0$ in eq. (4.20) gives the condition for equilibrium for outward delamination. In each case putting $a = a_0$ and $b = b_0$, we get two critical pressures denoted by $p_{c,a}$ and $p_{c,b}$ corresponding to eq. (4.20) and eq. (4.21) respectively. These are the

pressures at which delamination begins in the outward or the inward direction and again it can be shown that $p_{c,a} > p_{c,b}$ when $\Gamma_a = \Gamma_b$.

$$p_{c,a} = \left(8\Gamma_a \left(\frac{4Et}{1-v^2}\right)^{\frac{1}{3}} \frac{a_0^2(a_0^2 + b_0^2 - r_0^2)^{\frac{1}{3}}}{5a_0^4 + a_0^2 b_0^2 - 5a_0^2 r_0^2 + r_0^4}\right)^{\frac{3}{4}} \tag{4.22}$$

$$p_{c,b} = \left(8\Gamma_b \left(\frac{4Et}{1-v^2}\right)^{\frac{1}{3}} \frac{b_0^2(a_0^2 + b_0^2 - r_0^2)^{\frac{1}{3}}}{5b_0^4 + a_0^2 b_0^2 - 5b_0^2 r_0^2 + r_0^4}\right)^{\frac{3}{4}} \tag{4.23}$$

In view of the difficulty involved in determining analytically the stability of the equilibrium configurations from the second derivatives of the free energy, we use graphical means to investigate the stability for certain example geometries with graphene membranes. Consider a system with $a_0 = 2$ μm, $b_0 = 0.5$ μm, $Et = 340$ N/m, $v = 0.16$ and $\Gamma_a = \Gamma_b = 0.2$ J/m². The critical pressures are then $p_{c,a} = 1.94$ MPa and $p_{c,b} = 0.99$ MPa. Since $p_{c,b} < p_{c,a}$, delamination should start in the inward direction i.e. on the island. The plots in Fig. 4.7 show the free energy as a function of width of the delaminated annular region, $b_0 - b$ when the delamination is inwards. When $p < p_{c,b}$ (blue curve, Fig. 4.7), the free energy function has an energy barrier implying no delamination at all. It is clear that when $p = p_{c,b}$ (black curve, Figs. 4.7), the free energy has a local maximum at (a_0, b_0). Hence, we have an unstable equilibrium along the b direction i.e. delamination from the island. Finally if $p > p_{c,b}$ (red curve, Figs. 4.7), there is no energy barrier for delamination in the b direction. So at or above the critical pressure $p_{c,b}$, the membrane delaminates from the island and hence we no longer have an annular deformation. As the membrane pops off from the island, it should now assume a spherical bulge shape as in a standard blister test that is described in the previous chapter. Accordingly, the membrane mechanics and the system thermodynamics are described by the analysis developed in the previous chapter. We

had a critical pressure, p_c associated with this configuration given by eq. (3.17) (Γ is replaced with Γ_a). Assuming $p_c > p_{c,b}$, this gives rise to two different scenarios: $p_c > p > p_{c,b}$ and $p_c \leq p$. In the former case, we will have a spherical bulge without any blister formation and in the latter case, the membrane starts to form a circular blister. So to summarize:

(a) $p < p_{c,b}$ − annular bulge with no delamination.

(b) $p_{c,b} \leq p < p_c$ − unstable delamination in the inward direction and spherical bulge.

(c) $p \geq p_c$ − unstable delamination first in the inward direction and then in the outward direction.
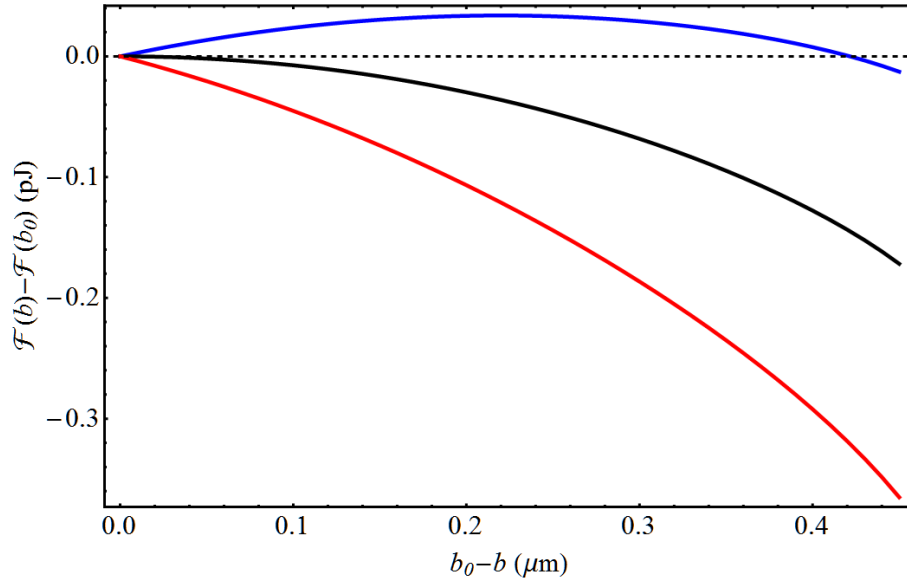
Figure 4.7 Plots showing the free energy variation at fixed $a = a_0$ as a function of the difference of initial inner radius and inner blister radius at different pressures - (blue) $p = 0.6$ MPa, (black) $p = 0.99$ MPa $= p_{c,b}$ and (red) $p = 1.4$ MPa.

If $p_c \leq p_{c,b}$, then there are only two scenarios: $p < p_{c,b}$ meaning no delamination and an annular bulge and $p \geq p_{c,b}$ meaning unstable delamination from both the inward and the outward directions. In this case with $\Gamma_a = 0.2$ J/m^2 and $a_0 = 2$ μm, p_c is 1.17 MPa and hence the applied

pressure has to be less than this value, p_c to avoid blow-off and between $p_{c,b}$ and p_c to just delaminate from the island.
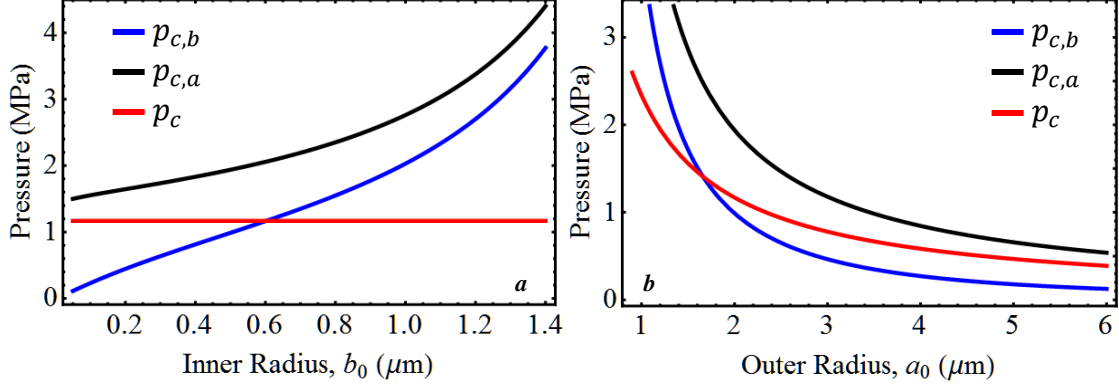
Figure 4.8 Plots of $p_{c,a}$, $p_{c,b}$ and p_c with respect to (a) annular cavity inner radius, b_0 with $a_0 = 2$ μm, $\Gamma_a = \Gamma_b = 0.2$ J/m², (b) annular cavity outer radius, a_0 with $b_0 = 0.5$ μm, $\Gamma_a = \Gamma_b = 0.2$ J/m²

The variation of the three critical pressures involved $p_{c,a}$, $p_{c,b}$ and p_c at fixed a_0 and b_0 are plotted in Figs. 4.8a and 4.8b respectively. It can be seen that in either case $p_{c,a}$ is always greater than $p_{c,b}$. Also, there are special outer and inner radii where $p_c = p_{c,b}$. Let them be denoted by a_0^* and b_0^* respectively. If $b_0 \geq b_0^*$ and $p = p_{c,b}$ at fixed a_0 ($= 2$ μm), then there will be complete blow-off because from Fig. 4.8a $p_c \leq p_{c,b}$; while if $b_0 < b_0^*$, there will be delamination only from the island. Likewise, if $a_0 \leq a_0^*$ at fixed b_0 ($= 0.5$ μm) there will be complete blow-off and if $a_0 > a_0^*$ there will be just delamination on the island when $p = p_{c,b}$.

Now let $\Gamma_a \neq \Gamma_b$. If $\Gamma_a > \Gamma_b$, it has the effect of increasing only p_c and $p_{c,a}$ relative to $p_{c,b}$. Hence the overall mechanics and thermodynamics is not much different from what has been described before. On the other hand if $\Gamma_b > \Gamma_a$, we might have a scenario where $p_{c,a} < p_{c,b}$ depending on the geometry. This means that we will have delamination in the outward direction first as shown in Fig. 4.2c. The plots in Figs. 4.9a,b show how the critical pressures vary with geometry with $\Gamma_a = 0.2$ J/m² and $\Gamma_b = 0.4$ J/m². We changed Γ_b from 0.2 J/m² to 0.4 J/m² and kept

Γ_a the same as in the calculations shown in Fig. 4.8. Hence only the $p_{c,b}$ curve is different from what we have in Fig. 4.8, while the p_c and $p_{c,a}$ curves remain exactly the same. Figure 4.9a shows that at a fixed a_0 (= 2 µm) there exists a critical inner radius b_0' above which $p_{c,a} < p_{c,b}$. This is in contrast to being $p_{c,a} > p_{c,b}$ when $\Gamma_a = \Gamma_b$. Similarly at a fixed b_0 (= 0.5 µm), there exists a critical outer radius a_0' such that below this value $p_{c,a} < p_{c,b}$ and above it $p_{c,a} > p_{c,b}$. As mentioned before, $p_{c,a}$ being smaller than $p_{c,b}$ enables the experimenter to achieve delamination, still unstable, along the outward direction first. But as the membrane delaminates and the blister radius a increases beyond a_0', $p_{c,b}$ will no longer be greater than $p_{c,a}$. This causes delamination inwards too, thus leading to blow-off. If $\Gamma_b \gg \Gamma_a$, we might avoid this by making a_0' very large.
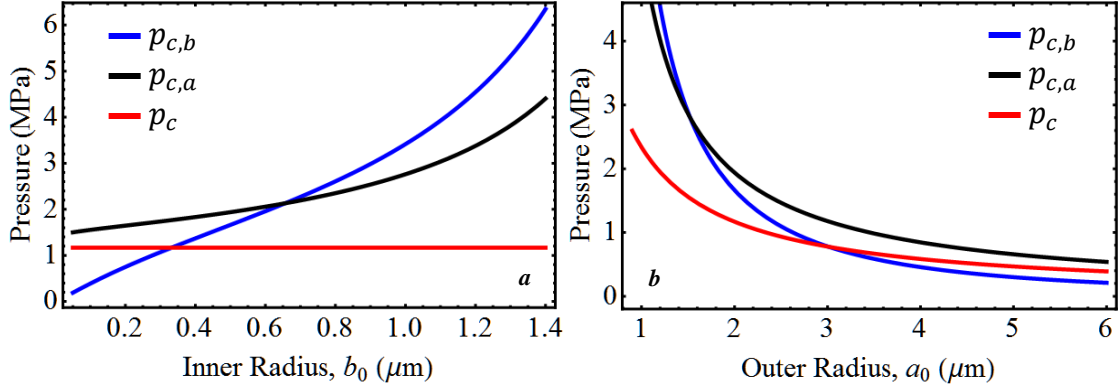
Figure 4.9 Plots of $p_{c,a}$, $p_{c,b}$ and p_c with respect to (a) annular cavity inner radius, b_0 with $a_0 = 2$ µm, (b) annular cavity outer radius, a_0 with $b_0 = 0.5$ µm. In both cases, $\Gamma_a = 0.2$ J/m² and $\Gamma_b = 0.4$ J/m².

Let us now analyze the constant N island blister test. At an equilibrium configuration we have:

$$\frac{\partial \mathcal{F}(a,b)}{\partial a} = -\frac{3p}{4}\frac{\partial V_a}{\partial a} + \frac{V_a}{4}\frac{\partial p}{\partial a} + 2\pi \Gamma_a a = 0$$
$$\frac{\partial \mathcal{F}(a,b)}{\partial b} = -\frac{3p}{4}\frac{\partial V_a}{\partial b} + \frac{V_a}{4}\frac{\partial p}{\partial b} - 2\pi \Gamma_b b = 0$$

(4.24)

Here p $(= p_i - p_a)$ is now not a constant as in the constant P case. From eq. (4.6), we know that V_a is a function of a, b and p (p itself is a function of a and b, eq. (4.18)). So, using the chain rule we get:

$$\frac{\partial V_a}{\partial a} = \frac{\partial V_a}{\partial a} \Big|_{p_i} + \frac{\partial V_a}{\partial p} \Big|_a \frac{\partial p}{\partial a} = \frac{\partial V_a}{\partial a} \Big|_{p_i} + \frac{1}{3} \frac{\partial p}{\partial a}$$
$$\frac{\partial V_a}{\partial b} = \frac{\partial V_a}{\partial b} \Big|_{p_i} + \frac{\partial V_a}{\partial p} \Big|_b \frac{\partial p}{\partial b} = \frac{\partial V_a}{\partial b} \Big|_{p_i} + \frac{1}{3} \frac{\partial p}{\partial b}$$

(4.25)

Putting eqs. (4.25) in eqs. (4.24) gives us:

$$\frac{\partial \mathcal{F}(a,b)}{\partial a} = -\frac{3p}{4} \frac{\partial V_a}{\partial a} \Big|_{p_i} + 2\pi \Gamma_a a = 0$$

(4.26)

$$\frac{\partial \mathcal{F}(a,b)}{\partial b} = -\frac{3p}{4} \frac{\partial V_a}{\partial b} \Big|_{p_i} - 2\pi \Gamma_b b = 0$$

Thus we get back essentially the same equations as in the constant P case (see eq. (4.19)) except that p is now obtained by solving eq. (4.18) at a given input or charging pressure p_0 instead of being a constant. As a result, the eqs. (4.22) and (4.23) which give $p_{c,a}$ and $p_{c,b}$ are still valid. Through eq. (4.18) and with the values of $p_{c,a}$ and $p_{c,b}$, we get two critical charging pressures $p_{0,c}^a$ and $p_{0,c}^b$. Due to the nature of the eq. (4.18), it is not easy to express the critical charging pressures explicitly as functions of a, b and Γ_a or Γ_b.
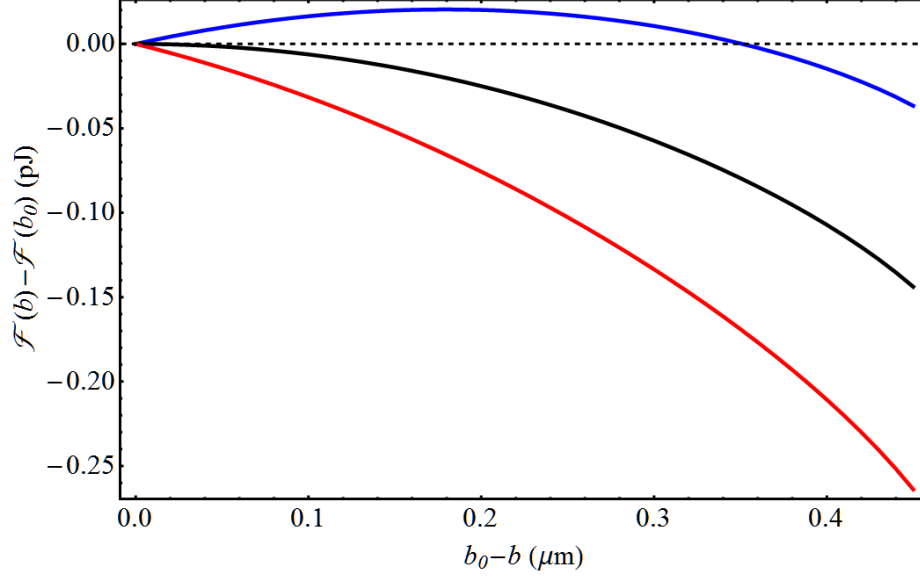
Figure 4.10 Plots showing the free energy variation as a function of the difference of initial inner radius and inner blister radius at different pressures - (blue) $p_0 = 1.0$ MPa,(black) $p_0 = 1.39$ MPa $= p_{0,c}^b$ and (red) $p_0 = 1.8$ MPa.

We again make use of graphical means to investigate the characteristics of the equilibrium configurations. With the same geometry and parameters that are used to plot Fig. 4.7 ($a_0 = 2$ μm, $b_0 = 0.5$ μm, $\Gamma_a = \Gamma_b = 0.2$ J/m², $Et = 340$ N/m, $\nu = 0.16$) and the depth of the cavity $h = 0.2$ μm, we plot the free energy $\mathcal{F}$ at fixed a ($= a_0$) and at different charging pressures p_0 in Fig. 4.10. The values of $p_{0,c}^a$ and $p_{0,c}^b$ in this case are 2.77 MPa and 1.39 MPa respectively. As before with the constant P IBT case, the critical pressure needed to delaminate inwards is smaller than that needed to delaminate outwards. And it is clear from the similarity of the Figs. 4.10 and 4.7 that the situation in this case is not much different. And as in the constant P IBT, we have three scenarios:

(a) $p_0 < p_{0,c}^b$ − energy barrier exists (blue curve, Fig. 4.10) preventing delamination. Hence we just have an annular deformation.

(b) $p_0 \geq p_{0,c}^b$ − energy barrier vanishes when $p_0 = p_{0,c}^b$ and we have an unstable equilibrium at $b = b_0$ (black curve, Fig. 4.10). This means complete delamination from the island with formation of a circular bulge as in the standard blister test. Two different

60

scenarios are possible depending on the value of $p_{0,c}$, the critical input pressure in the case of constant N standard blister test (obtained from eq. (3.26) with $\Gamma = \Gamma_a$):

(1) $p_0 \leq p_{0,c}$ – no delamination along the outer boundary i.e. $a = a_0$.

(2) $p_0 > p_{0,c}$ – there will be stable delamination along the outer boundary too and $a > a_0$. This behavior here is in contrast to the constant P island blister case where there will be complete unstable delamination with blow-off.
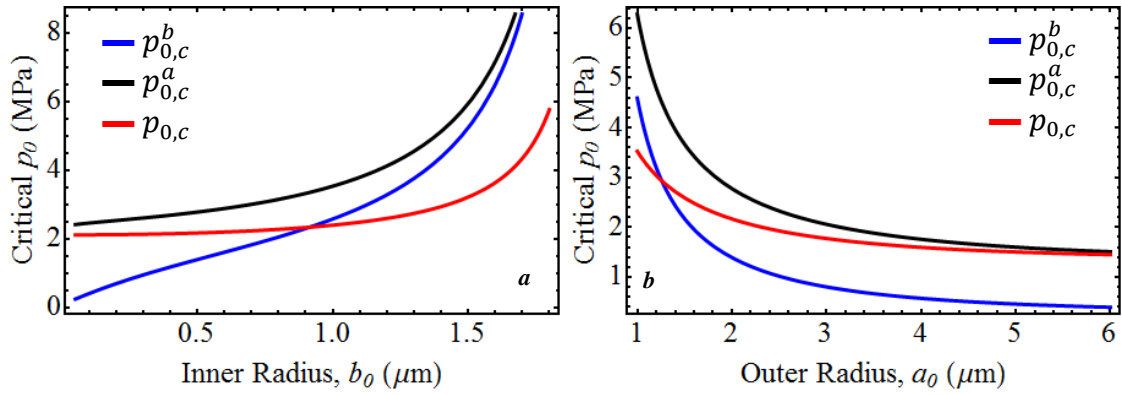
Figure 4.11 Plots of the critical input pressures associated with constant N IBT with respect to (a) annular cavity inner radius, b_0 with $a_0 = 2$ μm, (b) annular cavity outer radius, a_0 with $b_0 = 0.5$ μm. In both cases, $\Gamma_a = 0.2$ J/m², $\Gamma_b = 0.2$ J/m² and $d = 0.2$ μm.
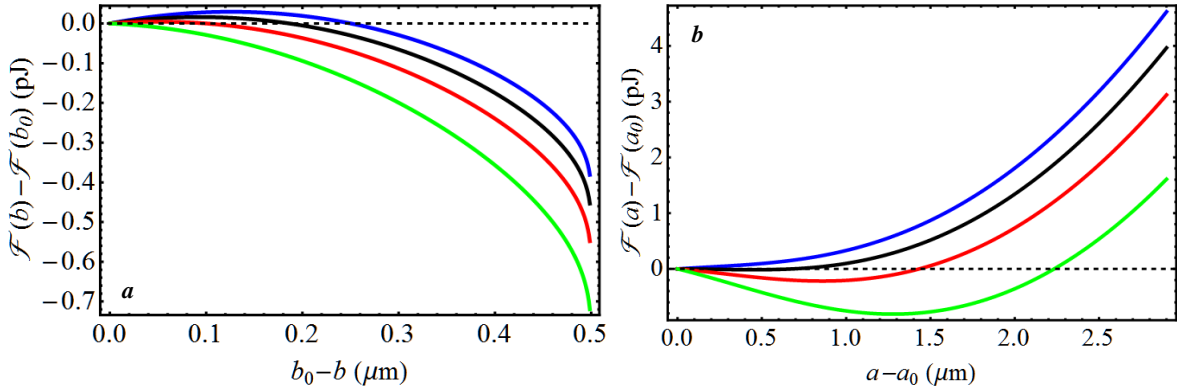
Figure 4.12 Plots showing the free energy variation at fixed (a) $a (= a_0)$ and (b) $b (= b_0)$ as a function of the difference of (a) initial inner radius and inner blister radius and (b) initial outer radius and outer blister radius respectively at (blue) $p_0 = 2.6$ MPa, (black) $p_0 = 2.77$ MPa $= p_{0,c}^a$, (red) $p_0 = 3.0$ MPa, and (green) $p_0 = 3.4$ MPa.

Figures 4.11a and 4.11b show the variation of the critical pressures $p_{0,c}^a$, $p_{0,c}^b$ and $p_{0,c}$ with respect to a_0 and b_0 when b_0 and a_0 are held fixed respectively. This again looks similar to the constant P IBT counterpart Fig. 4.8. Here too, we have a special inner radius b_0^* (outer radius a_0^*) where $p_{0,c} = p_{0,c}^b$ at a given outer radius a_0 (inner radius b_0).

What happens when $p_{0,c}^a < p_{0,c}^b$? Let us look at this case by slightly changing the parameters used in the above example scenario. We change Γ_b to 0.6 J/m^2 from 0.2 J/m^2. This results in no change for $p_{0,c}^a$ (= 2.77 MPa) but $p_{0,c}^b$ increases to 3.25 MPa. This indicates that the delamination will start at the outer boundary while the inner boundary stays attached to the island. The plots of the free energy at input pressures below, equal to and above $p_{0,c}^a$ are shown in Figs. 4.12a and 4.12b. In the case of the free energy plots along the b direction, we have an energy barrier in all the first three cases (blue, black and red curves with $p_0 = 2.6$ MPa, 2.77 MPa and 3.0 MPa respectively in Fig. 4.12a). Hence the membrane stays attached to the island in each of those cases. While along the a direction we see from Fig. 4.12b if:

(a) $p_0 < p_{0,c}^a$ – the free energy has no equilibrium configurations (blue curve with $p_0 = 2.6$ MPa, Fig. 4.12b) and has a local minimum at $a = a_0$. Hence there will be no delamination and we have an annular bulge.

(b) $p_0 \geq p_{0,c}^a$ – the free energy has an equilibrium configuration which is a minimum implying a stable equilibrium and no energy barriers. The equilibrium configuration is at $a = a_0$ when $p_0 = p_{0,c}^a$ (black curve with $p_0 = 2.77$ MPa, Fig. 4.12b). Again we have two scenarios branching from this situation which are, if:

(1) $p_{0,c}^a < p_0 < p_{0,c}^b$ – leads to annular bulge with delamination along the a direction until it reaches the equilibrium on the free energy curve as shown in

62

Fig. 4.12b (red curve with $p_0 = 3.0$ MPa). The membrane stays attached to the island as we still have an energy barrier (as seen in the red curve, Fig. 4.12a) along the b direction in this input pressure range that discourages delamination from the island.

(2) $p_0 \geq p_{0,c}^b$ – leads to delamination from the island completely as the energy barrier is no longer there (green curve with $p_0 = 3.4$ MPa, Fig. 4.12a) and hence leads to a circular bulge or blister depending on the values of $p_{0,c}$. In this case a blister as p_0 exceeds $p_{0,c} = 2.17$ MPa.
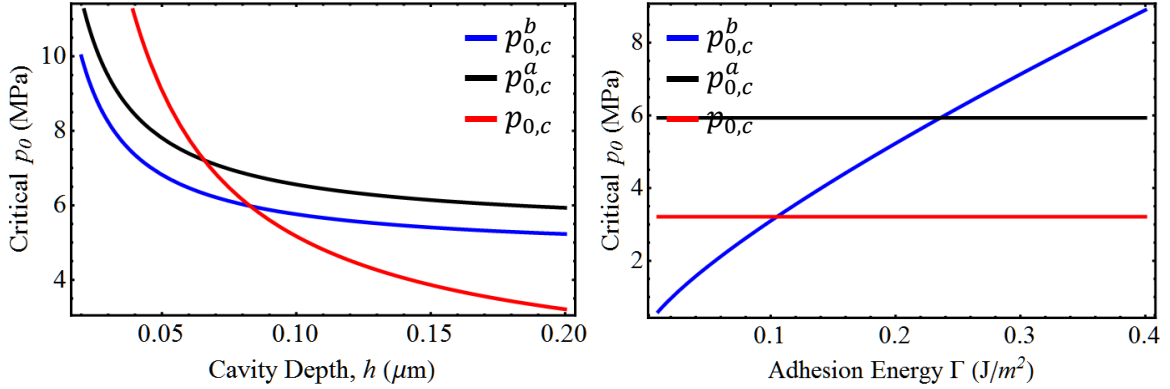
Figure 4.13 Variation of critical charging pressures with cavity depth h and island adhesion energy Γ. When not varied, the values of the other parameters are $Et = 340 \, N/m$, $v = 0.16$, $a_0 = 2 \, \mu m$, $b_0 = 1.5 \, \mu m$, $d = 0.2 \, \mu m$ and $\Gamma = 0.2 \, J/m^2$.

In Fig. 4.13a, we show similar results to those in Fig. 4.11 but we vary the depth of the cavity and the adhesion strength on the island here. The system parameters used in these plots are the same as in Fig. 4.11 except $b_0 = 1.5$ μm here. The variation in the depth of the cavity gives a result which looks similar to the results in Fig. 4.11a. When the adhesion strength on the island (Fig. 4.13b) is varied assuming the adhesion strength on the outer boundary is still 0.2 J/m², there is a critical adhesion strength at which delamination from the outer boundary is favored over island delamination. In other words, as we increase the adhesion strength on the island there is a critical

value above which the energy release rate for island delamination goes below that for delamination from outer boundary.
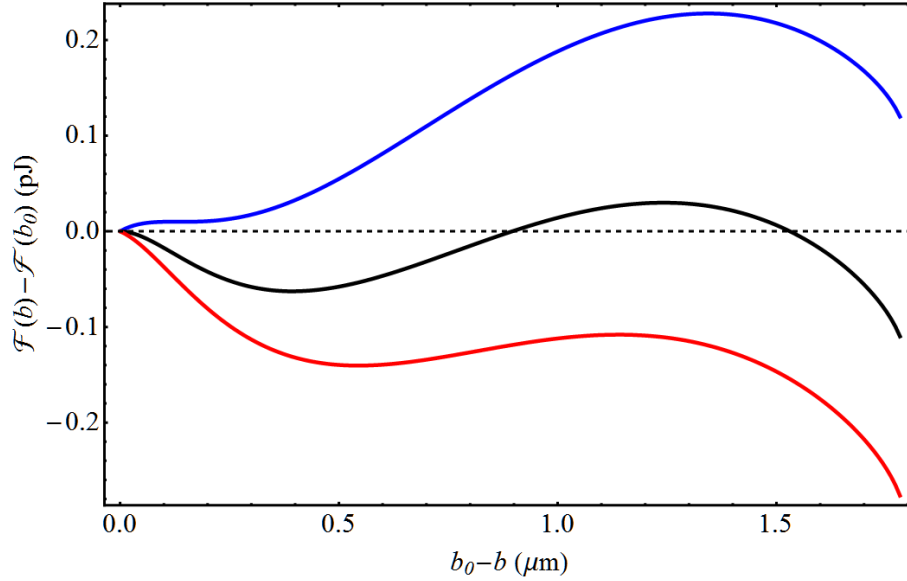
Figure 4.14 Plots showing $\mathcal{F}(a_0, b)$ as a function of the difference of initial inner radius and inner blister radius at (blue) $p_0 = 16$ MPa, (black) $p_0 = 17.74$ MPa $= p_{0,c}^b$ and (red) $p_0 = 18$ MPa.

With the help of the two examples described until now, we notice that the delamination from the island is not stable even though we are using limited number of gas atoms. It can be made stable by carefully choosing the system parameters. As the inward delamination sets in, the stiffness of the system decreases at a faster pace than the critical pressure leading to unstable delamination. However it is possible to arrest this unstable inwards delamination process, one way is to make the inner radius large enough. Hence if we let $a_0 = 2$ μm, $b_0 = 1.8$ μm, $h = 0.02$ μm, $Et = 340$ N/m and $\Gamma_a = \Gamma_b = 0.2$ J/m², we get $p_{0,c}^a = 13.32$ MPa and $p_{0,c}^b = 17.74$ MPa. The free energy at fixed $a(= a_0)$ is plotted in Fig. 4.14 as before. From the three curves in Fig. 4.14, we can say that if:

(a) $p_0 < p_{0,c}^b$ – (as in the blue curve with $p_0 = 16$ MPa, Fig. 4.14) the free energy has an equilibrium configuration at $b < b_0$, but there is an energy barrier and hence no delamination. We will see just an annular bulge.

(b) $p_0 \geq p_{0,c}^b$ – (as in the black and red curve with $p_0 = p_{0,c}^b = 17.74$ MPa and $p_0 = 18$ MPa respectively, Fig. 4.14) the energy barrier vanishes and now we have a local minimum at $0 < b \leq b_0$ on the free energy curve implying a stable equilibrium without complete delamination. In addition, we also have an inaccessible equilibrium configuration which is a maximum. When $p_0 = p_{0,c}^b$, there is an equilibrium configuration which is a maximum at exactly $b = b_0$.

Hence with this geometry, we have what is initially an unstable delamination from the island leading to a stable equilibrium configuration. It is to be noted that as the charging pressure is increased, the minimum and the maximum to the right move closer and coalesce. When this happens we will have a complete delamination from the island.

Now if in the previous case the depth of the cavity is changed to 0.01 μm keeping everything else the same, we see a different behavior from the system as shown in Fig. 4.15. The free energy in this case has a minimum at the critical charging pressure ($p_{0,c}^b = 23.32$ MPa) at $b = b_0$ meaning the delamination from the island will be stable. But as in the previous case, the minimum vanishes at a specific charging pressure again resulting in unstable delamination.
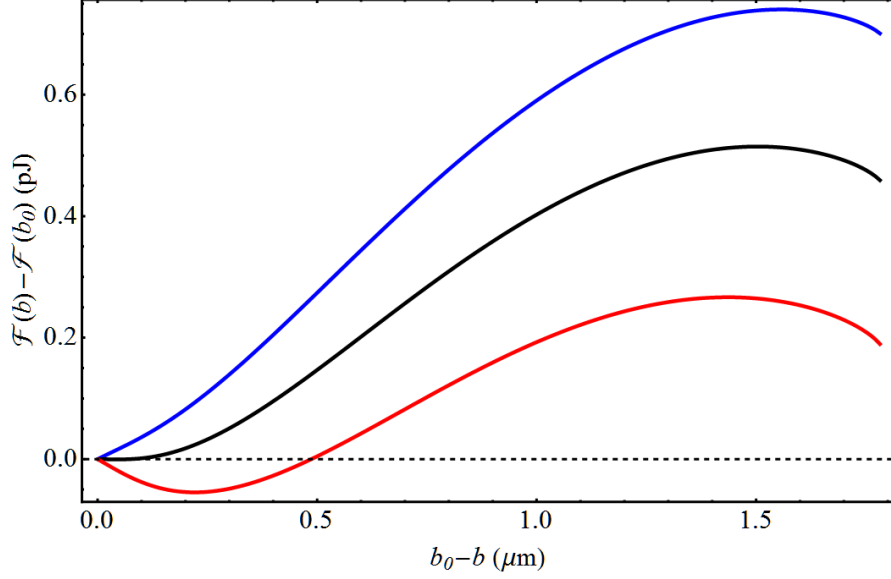
Figure 4.15 Plots showing $\mathcal{F}(a_0, b)$ as a function of the difference of initial inner radius and inner blister radius at (blue) $p_0 = 20$ MPa, (black) $p_0 = 23.32$ MPa $= p_{0,c}^b$ and (red) $p_0 = 27$ MPa.

In summary, the constant N island blister delamination is unstable for most geometries but can be made stable for a given outer diameter by decreasing the depth of the cavity and increasing the radius of the island. This in effect decreases the initial volume occupied by the pressurized gas. Mathematically speaking, the delamination is unstable because the stiffness of the membrane as it delaminates decreases at a larger rate than the pressure of the expanding gas. But having a large inner radius b and small initial volume can reverse this trend, albeit only for a specific range of pressures. In each scenario, the common feature is that the membrane goes from being flat to being annularly deformed under a pressure load and at a sufficiently higher pressure, the membrane delaminates from the island to form a spherical bulge or blister.

4.3 Experiment
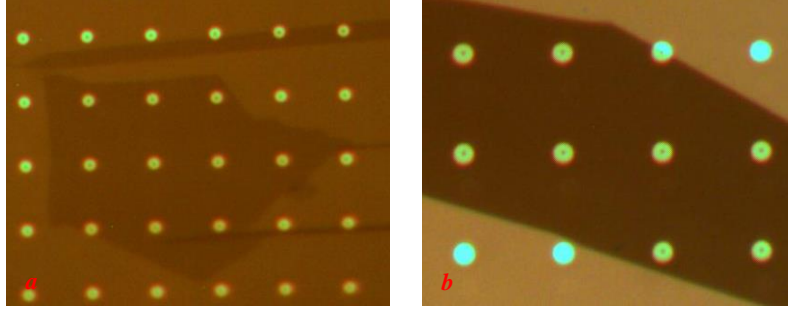
Figure 4.16 Optical images of the devices covered with (a) monolayered graphene flake, (b) five layered graphene flake.

The goal is to observe the annular deformations of the graphene membrane and find the critical delamination pressure for the island ($p_{0,c}^b$) at lower pressures. In conjunction, we also perform the standard blister test by extending the input pressure beyond $p_{0,c}^b$ and above $p_{0,c}$. This allows us to evaluate the accuracy of the island blister test in measuring adhesion energy and simultaneously enables us to showcase the variety of mechanical deformations possible with this geometry under a pressure load. The ability for a membrane to assume different configurations under a pressure load might have applications in micro/nano scale devices.

The experimental setup is almost exactly the same as described in section 3.2. For the sake of completeness, it is described again in brief. Annular cavities are lithographically patterned onto a silicon chip with a thermally grown silicon oxide of thickness 90 nm. Graphene flakes are mechanically exfoliated onto the chip and the number of layers in each graphene flake is determined using Raman spectroscopy (see Appendix, A.2.1). We fabricated eight mono-layered devices, the optical image of which is shown in Fig. 4.16a, with outer radius $a_0 = 1.50$ μm, inner radius $b_0 = 0.35$ μm and depth $h = 112$ nm and eight five-layered devices with dimensions $a_0 = 1.70$ μm, $b_0 = 0.25$ μm and $h = 106.5$ nm. The devices are charged with nitrogen molecules at a given input pressure in a pressure chamber. After giving sufficient time for the pressures inside

and outside the cavity to equilibrate, we take them out and measure the deformation of each device that is a result of the change in the pressure outside the cavity using an atomic force microscope (AFM). The input pressures applied range between approximately 290 kPa to 4.10 MPa with the experiment proceeding from lower to higher values.

4.4 Experimental Results
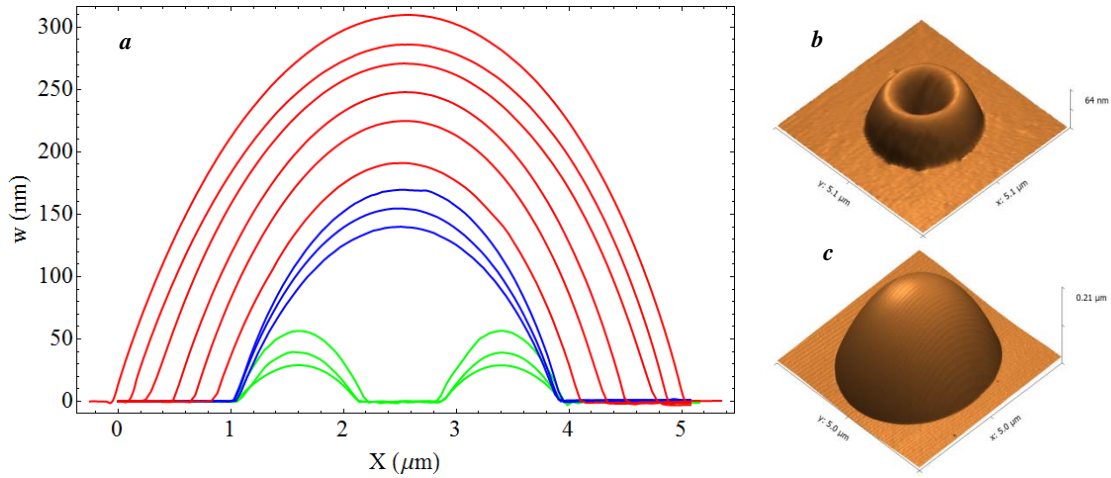
Figure 4.17 Cross-sections of AFM height images for mono-layered graphene blisters: green (annular), blue (spherical with no delamination), and red (spherical with delamination). The pressures at which they are obtained in increasing order are p_0 = 289.8 kPa, 512.6 kPa, 733.0 kPa, 929.0 kPa, 1223.0 kPa, 1659.0 kPa, 2051.0 kPa, 2557.0 kPa, 3010.0 kPa, 3431.0 kPa, 3755.0 kPa, and 4165.0 kPa. (b, c) Three dimensional rendering of annular and spherical blisters obtained by AFM respectively.

Full-field measurements of deformed blisters show that the deformations are axisymmetric (see Appendix, A.2.2 for full AFM images), allowing us to describe the deformed configurations using just the deflection along a diametrical chord. Measured deflection profiles at different charging pressures for a representative device are plotted in Fig. 4.17a. At charging pressures below 750 kPa for this particular device (green curves), the membrane is adhered to the island, and as we gradually increase the charging pressure it delaminates from the island (at 929 kPa). At even higher pressures (about 2 MPa, red curves), the membrane then starts delaminating in the

outward direction. Also shown in Figs. 4.17b,c are full-field 3D AFM height scans of an annular and a spherical blister, demonstrating the axisymmetric deformation.

Charging Pressure, p_0 (kPa)	289.8	512.6	733.0	929.0
Mono-layered Island radius, b (nm) ($b_0 = 350.0$ nm)	335.0	335.0	295.0	270.0 (2 devices)
Multi-layered Island radius , b (nm) ($b_0 = 250.0$ nm)	185.0	195.0	150.0 (3 devices)	-

Table 4.1   *Averaged radii of the region of the membrane still attached to the island at different charging pressures.*

Charging Pressure, p_0 (MPa)	Mono-layered Devices ($a_0 = 1.5$ μm)		Multi-layered Devices ($a_0 = 1.7$ μm)	
	Averaged Blister Radius, a (μm)	Adhesion Energy, Γ (mJ/m^2)	Averaged Blister Radius, a (μm)	Adhesion Energy, Γ (mJ/m^2)
2.05	1.61	112.13	-	-
2.56	1.86	126.97	1.80	128.78
3.01	1.99	141.28	1.88	153.66
3.43	2.20	142.40	2.07	161.13
3.76	2.37	139.51	2.24	161.05
4.16	2.52	141.58	2.41	162.36

Table 4.2 Calculated adhesion energies along with the blister radii at different charging pressures

From these measurements, we first find the critical island delamination pressure, $p_{0,c}^b$ and using eqs. (4.18) and (4.21), we find the adhesion energy on the island. We found that mono-layered membranes delaminated completely from the island at a charging pressure between 733 kPa and 1223 kPa (see Table 4.1 above). Based on the observation that two of the eight mono-

layered devices remain attached to the island at 929 kPa, we took this value to be our best estimate of the critical charging pressure for island delamination, $p_{0,c}^b$. This is because from Table 4.1 it is evident that the membranes are slowly delaminating from the island and at 929.0 kPa all but two of them delaminate completely. Other devices conceivably could have been still attached to the island at slightly lower charging pressures. Employing a similar argument, we assume that $p_{0,c}^b$ is 733.0 kPa for multi-layered devices. With $p_{0,c}^b = 929.0$ kPa and $b = 270.0$ nm, the adhesion energy on the island is estimated to be 102.6 mJ/m^2 for mono-layered membranes. It is 123.8 mJ/m^2 for multi-layered membranes with $p_{0,c}^b = 733.0$ kPa and $b = 150.0$ nm.

Now, we look at the measurements made after delamination begins to take place along the outward direction to obtain both the adhesion energy and critical delamination pressure, $p_{0,c}$. In Table 4.2, we tabulated the averaged blister radii at different charging pressures and calculated the adhesion energy using eq. (3.23). For mono-layered devices, it can be seen that the calculated adhesion energy increases from 112.13 mJ/m^2 at 2.05 MPa to about 140 mJ/m^2 at 3.01 MPa and then remains at about this value at higher pressures. Likewise for multi-layered devices, the apparent adhesion energy is 128.78 mJ/m^2 at 2.56 MPa and reaches a stable value of about 160 mJ/m^2 at and above 3.43 MPa. Thus the apparent adhesion energy near the edge of the cavity is lower than that in the regions sufficiently away from the edge. Also, note that the adhesion energy close to the edge is about the same as that found on the islands. This suggests that perhaps the apparent adhesion energy varies along the radial direction due to topographic variations near the perimeter of the cavity (as well as near the island boundary), including a non-ideal circular boundary, a boundary that is not sharp (as assumed in our model), and roughness variations near the perimeter of the cavity. In order to estimate the critical charging pressure, $p_{0,c}$ with our theory, we used the lowest apparent adhesion energy with $a = a_0$ and plugged in these values into eq.

(3.26). This results in $p_{0,c} = 2.0$ MPa for mono-layered membranes and 2.14 MPa for multi-layered ones.
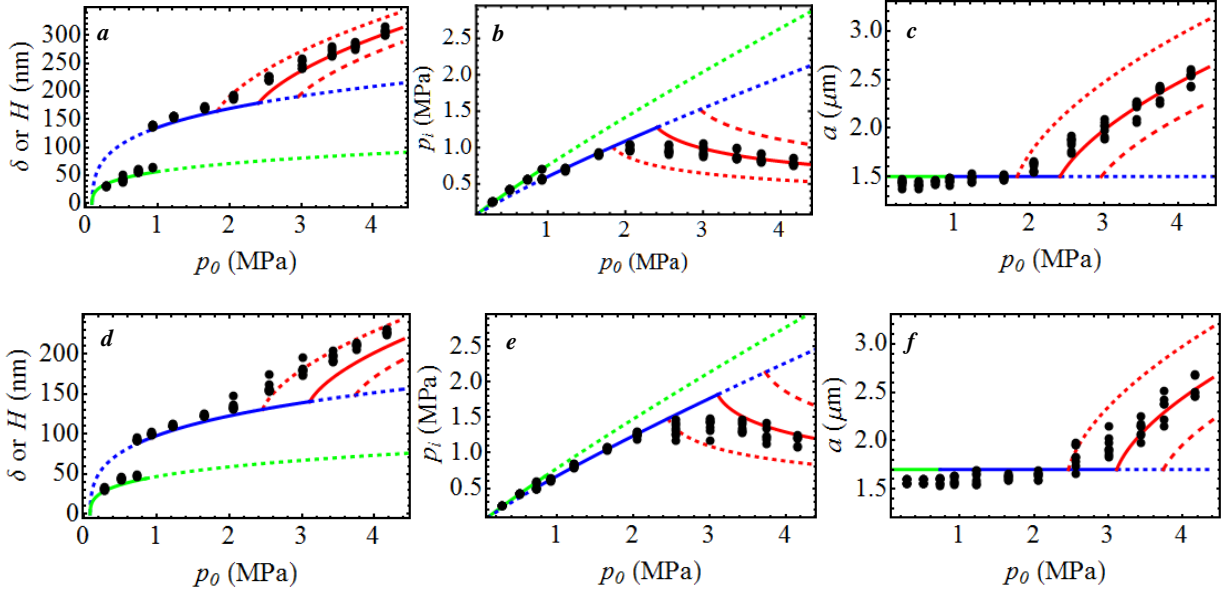
Figure 4.18 (a, d) Maximum deflection (δ = spherical, H = annular); (b, e) equilibrium pressure in the microcavity (p_i); and (c, f) outer radius of the circular bulge (a) versus the charging pressure (p_0). Figures (a,b,c) are for graphene monolayers and (d,e,f) are for multilayers. In each case the symbols are measurements and the curves are theory. The green curve is for the annular deformation, the blue curve for the spherical deformation without delamination, and the red curves are for spherical deformation with delamination for different values of adhesion energies: dashed – 100 (120) mJ/m², solid – 140 (160) mJ/m² and long dashed – 180 (200) mJ/m² for monolayer (multilayer) membranes.

Figures 4.18a,b,c show the experimentally-determined maximum deflection (H or δ), the final equilibrium internal cavity pressure (p_i) and the blister outer radius (a) for the monolayer devices as a function of charging pressure (p_o). Theoretical estimates are also shown in each figure. Both experiments and theory show three configurations: i) annular blisters (green lines), ii) spherical blister before delamination (blue lines), and iii) spherical blisters after delamination from the outer boundary (red lines). The solid, dashed and long-dashed red curves in the figures are calculated with different values of adhesion energy which are 140 ± 40 mJ/m² where 140 mJ/m² is the average adhesion energy for monolayer membranes obtained using the last four data points

(see Table 4.2) where significant outward delamination occurs and thus our model is expected to be most accurate. It can be seen that our measurements for mono-layered devices are self-consistent among H or δ, p_i, and a and show good agreement with the theory.

Corresponding results for the five-layer devices shown in Figs. 4.18d,e,f are similar qualitatively, but differ from the monolayers in two ways. First the best-fit value of adhesion energy is 160 mJ/m^2, we think the difference in adhesion energies for mono-layer and fiver-layers may result from the complicated dependence of adhesion energy on the number of layers, surface topography and interfacial forces[82–84]. Second, the behavior is not as self-consistent among H or δ, p_i, and a; while the agreement between experiment and theory is reasonable, it is not as good as for the monolayer. We attribute this to wrinkling that appears to occur during deformation of the multilayer devices (see Appendix, A.2.3). While the broad nature of the axisymmetric deformation exists, the wrinkling indicates that our analytical model is not likely to work as well. Physically we think the wrinkling is facilitated by sliding of the membrane near the perimeter of the blister. We can approximate the effect of sliding by relaxing our assumption that the membranes are clamped by the adhesive interactions at the boundaries. Instead if we assume that the membranes are constrained from vertical movement, but allowed to slide on the substrate, then the membrane behaves softer than an equivalent clamped membrane with no sliding[85]. Incorporating the sliding boundary condition into our analysis results in good agreement between theory and experiment that is also self-consistent among H or δ, p_i, and a.

It is noteworthy that these adhesion energies are lower than the ones that we obtained in the experiment described in the previous chapter, 310-450 mJ/m^2 with the same substrate material. We do not fully understand the reasons for these differences but note that the fabrication process

details were different here, and it would not be surprising that this lead to different surface conditions and thus adhesion energy.

4.5 Summary

In conclusion, we performed the island blister test as well as standard blister test on monolayered and five-layered graphene membranes. At the same time, we demonstrated graphene blisters that can be switched and tuned by the combination of pressure and adhesion. Our measurements showed that graphene membranes can be switched from an annular to a spherical shape with varying lateral size using the pressure exerted by a fixed mass of trapped gas. We modeled the experimental system using a new nonlinear membrane model (for the annular blister) and ideal gas behavior in a thermodynamic framework to determine the deformation characteristics and the critical charging pressures at which the blisters switch shapes as a function of system parameters (geometry, elastic properties, pressure, and adhesion energy). This ability of graphene blisters to switch configurations can be potentially used to create surfaces with tunable topography when covered with a patterned array of these devices. The devices can potentially be made individually addressable, thereby making the tuning process dynamic. Such devices with dynamically tunable topography can be used to make smart surfaces that can change their surface/interfacial properties, for instance wettability. This device geometry can be extended to making electromechanical devices where electrostatic force between the graphene membrane and the substrate can be used to control the switching while keeping the pressure inside the cavity fixed for improved control and faster operation.

5. Effect of Interfacial Forces on Graphene Mechanics

5.1 Introduction

We know that at atomic scales, atoms are held together via very strong ionic or covalent bonds to form solids. The atoms which form the bulk of such solids are very stable and do not interact otherwise. However, the atomic species that form the surfaces of such solids behave differently than their bulk counterparts. They have higher energy due to the fact that these atoms bond with fewer atoms compared to the bulk atoms. Hence surfaces have special properties due to their active nature and interact with other surfaces to form interfaces. These interactions are usually mediated by either capillary, electrostatic, van der Waals, Casimir forces etc or a combination of these forces.

The van der Waals (vdW) force is the attractive force that arises between any two species of atoms, due to the interaction of electric dipoles, induced or instantaneous (quantum mechanical fluctuations), at very small separations (few Å). Casimir force is the macroscopic equivalent of the vdW forces at larger separations (tens of nanometers to several microns). A complete treatment of the vdW and Casimir forces is given by Lifshitz's theory. These forces have an electromagnetic origin and hence are inversely proportional to the separation between interacting bodies. At micro and nano-scales, vdW and Casimir forces dominate interfacial interactions between two mostly neutral surfaces in the absence of liquid layers. Futhermore, it is known that at separations smaller than a few nm's the dominant forces are the vdW forces.

A simple and effective way of describing vdW forces is the familiar Lennard-Jones 12-6 pair potential, given by:

$$U_{LJ}(r) = \frac{C_1}{r^{12}} - \frac{C_2}{r^6} \qquad (5.1)$$

Here C_1 and C_2 are constants dependent on the species of the pair of atoms interacting and r is the separation between them. The force due to this potential is attractive above an equilibrium separation and repulsive below it.
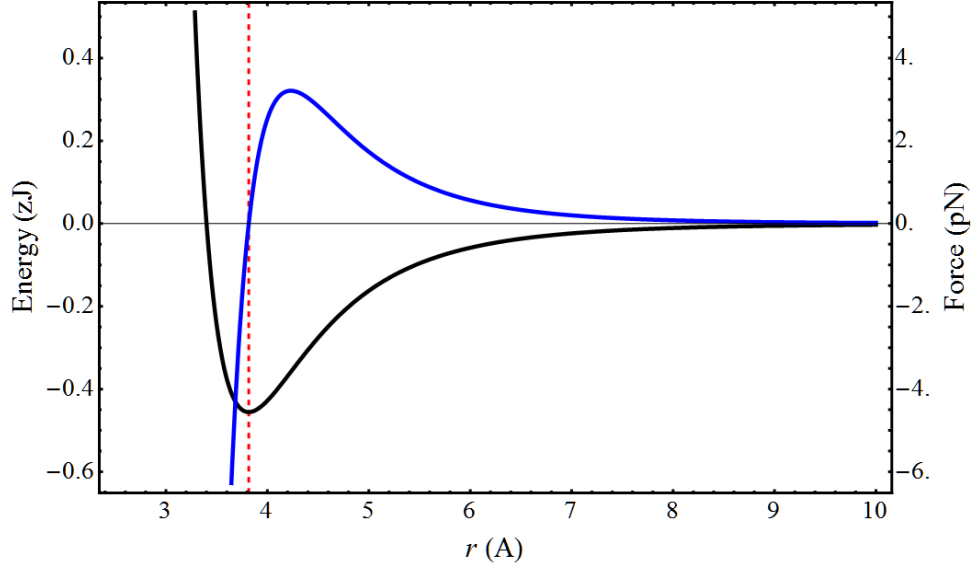
Figure 5.1 Lennard-Jones 12-6 potential (black Curve) and force (blue Curve) for C-C vdW interactions. The vertical red line intersects the two curves at the equilibrium separation, r_e=3.82 Å.

The LJ potential is shown in Fig. 5.1 (black curve) with $C_1 \approx 4.35 \times 10^{-135}$ and $C_2 \approx 2.82 \times 10^{-78}$ in MKS units corresponding to Carbon-Carbon interactions. Also the force due to this potential, $F_{LJ} = dU_{LJ}/dr$ is plotted in blue (positive force is attractive). The equilibrium separation in this case is $r_e = 3.82$ Å where $F_{LJ} = 0$. Ignoring any multi-body effects, we can sum these pair interactions for a large number of atoms constituting two macroscopic bodies to give the interfacial force between them due to vdW interactions. Hence for two plane parallel sheets of atoms as in graphene and other 2D materials separated by a distance d, the cumulative potential per unit area would be:

75

$$U_{LL}(d) = \rho_L^2 \int U_{LJ}(r) dA = 2\pi \rho_L^2 \left(\frac{C_1}{10d^{10}} - \frac{C_2}{4d^4} \right) \qquad (5.2)$$

The subscript 'L' is to signify layer and ρ_L is the density of atoms in a layer. This potential results in a traction equivalent to about 1.5 GPa at a separation of 4 Å and decreases to 250 Pa at about 10 nm separation for two parallel monolayer graphene layers. Likewise, the potential for a layered material with a bulk semi-infinite solid (denoted by subscript 'B') is given by:

$$U_{LB}(d) = \frac{\pi \rho_L \rho_B}{90} \left(\frac{2C_1}{d^9} - \frac{15C_2}{d^3} \right) \qquad (5.3)$$

With the advent of graphene and other 2D materials, numerous nano-devices have been proposed and realized where it is very common to have graphene suspended over a substrate with the separations being as small as few nanometers to hundreds of nanometers. It becomes very important to factor in the vdW and other similar interactions to account for the overall mechanics and electro-mechanics of these devices. Also, it is very essential to understand and characterize the dominant interfacial forces at a given length scale for fundamental physics metrology to be able to differentiate the dominant interaction from other interactions. To this end an experiment is devised to measure the operant interfacial forces acting on a graphene membrane due to a substrate. The experiment and the theory behind it are described in the rest of this chapter.

5.2 Experiment

Earlier attempts at measuring vdW or Casimir forces usually included aligned parallel plates, one fixed and the other connected to a spring through which the magnitude of the attractive force is measured. Since alignment at micro and nano-scales is inaccurate, one or both of the parallel plates is replaced by a spherical or cylindrical surface. This enabled experimentalists to measure the vdW or Casimir forces within a range of 100 nm to above 10 micron separations.[67,86]

In the case of 2D materials like graphene, it is very difficult to use this approach. However, using the experimental setup described in the previous chapter, we were able to measure the operant interfacial force between graphene membranes and SiO_x substrate at a separation of about 10 nanometers. The experiment has been performed entirely by Xinghui Liu under the guidance of Scott Bunch.
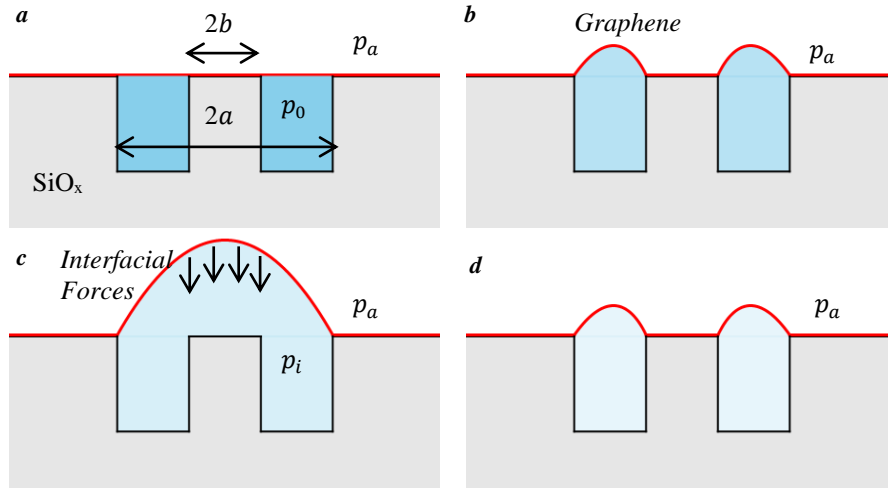
Figure 5.2 A device is charged to an initial pressure p_0 such that $p_0 > p_{0,c}^b$ and taken out of the pressure chamber. Each schematic shows the dynamics of the experimental process. (a) Initially the graphene membrane stays flat, (b) Deforms to form an annular bulge, (c) Delaminates off of the island and (d) Annular bulge following pull-in as the gas leaks out of the cavity. The color of the gas indicates decreasing pressure.

The experimental setup is shown in Fig. 5.2 and the device geometry is exactly the same as that used in the island blister test. The devices are charged to a pressure higher than the critical input pressure for delamination from the island, $p_{0,c}^b$ in a pressure chamber. Once the gas inside the cavity reaches equilibrium, the devices are taken out of the pressure chamber. The trapped gas expands due to the pressure difference forming an annular bulge deformation in the membrane followed by delamination to form a circular bulge during the transient response (Fig. 5.2b,c). The gas inside the cavity is now allowed to leak out through the oxide and this leaking process is

continuously monitored using an atomic force microscope (AFM). In this configuration, the graphene membrane directly above the island experiences not only the pressure load but also the forces due to the attractive interfacial interactions between the graphene membrane and the island made of SiO_x/Si. The operant interfacial forces, we assume, are either electrostatic forces, vdW or Casimir forces and try to pull down the membrane towards the island while the gas pressure opposes it. Initially, the separation between the membrane and the island is large enough that the effect of the interfacial forces is negligible. But as more and more atoms of the gas leak out, the deflection decreases due to lowering gas pressure implying a decreasing separation between the membrane and the island. This results in a continuous increase in magnitude of the interfacial forces owing to their inverse power law relationship with separation. The combined effect of decreasing gas pressure and gain in the strength of the surface interactions results in a pull-in instability at a critical separation. If the initial input pressure is carefully chosen and smaller gas atoms employed for charging, the entire process takes a few hours. The experiment is repeated with graphene membranes with varying number of layers (n) ranging from 1 to 5 and each time the pull-in distance recorded through the continuous AFM height scans. The experiments are also done with a layer of gold on the island on top of SiO_x.

5.3 Theory and Simulations

5.3.1   *Effect of Interfacial forces on Pressurized Graphene - Theory*

We assume that the interactions between the graphene membrane and the island are dominated by either the electrostatic or vdW or Casimir forces. Here, we develop our analysis in such a way such that we can account for any of these interactions interchangeably. We refer to the pressure due to the attractive interfacial forces between the membrane and the island by p_{att}. We neglect the effect of the bending rigidity of graphene membranes and develop a simple analytical

model based on membrane mechanics to describe the interrelationship of the system parameters in the experiment and we use it inversely with the measurements to infer the operant surface force.
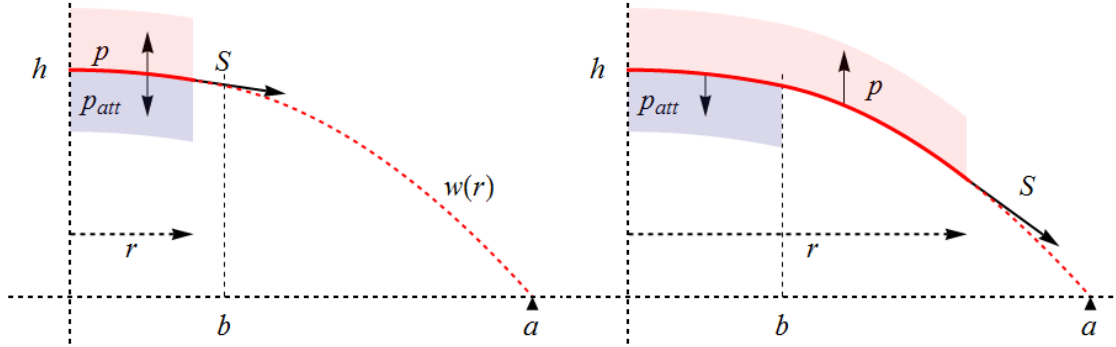
Figure 5.3 Schematics showing the forces acting on the membrane – p_{att} acts only on the membrane region where $r < b$ and the whole of the membrane experiences the gas pressure (p). The difference of p and p_{att} is balanced by the force exerted by the membrane tension S.

Owing to the axial symmetry of the geometry, we can look at the mechanics in a cylindrical coordinate system with r being the radial coordinate and $w(r)$ denoting the vertical deflection of the membrane. We look at two regions on the membrane separately – the region directly above the island and the rest of the membrane. We assume that only the region above the membrane experiences the attractive forces, although the interactions in reality diffuse over to a region slightly larger than this region. The different forces acting on each of these regions are shown in Fig. 5.3. The whole membrane is being pressurized uniformly by the trapped gas atoms which continuously decreases over the course of the experiment; let this pressure load be denoted by p. Then there is the pressure due to the attractive forces p_{att} acting over the region $r < b$. These forces are balanced by the force due to the membrane tension S. This membrane tension S has two components – the initial or residual tension (S_0) and the incremental tension in the membrane in the radial direction due to the deformation caused by the pressure loads (S_r). Hence force equilibrium in the vertical direction assuming small rotations gives:

$$(p - p_{att})r^2 = -2\,S(r)\,r\frac{dw(r)}{dr} \qquad r < b \tag{5.4}$$

$$pr^2 - p_{att}b^2 = -2\,S(r)\,r\frac{dw(r)}{dr} \qquad r \geq b$$

The key assumptions of our treatment are:

(1) The incremental membrane tension S_r, the initial tension S_0 and hence S are all uniform.

(2) The pressure due to the interactions acting between the island and the membrane, p_{att}, is uniform. This is reasonable if the membrane curvature is small.

In order to understand the validity and impact of these assumptions, we also carry out high-fidelity finite element simulations where these assumptions are not made; these are described in the next sub-section. The negative sign on the right hand side is due to dw/dr being negative. Integrating eqs. (5.4) with respect to r with appropriate limits while using the continuity condition for $w(r)$ at $r = b$, yields:

$$w(r) = h - \frac{p - p_{att}}{4S}r^2 \qquad r < b \tag{5.5}$$

$$w(r) = h + \frac{1}{4S}\left(p_{att}b^2\,\mathrm{Log}\left(\frac{r^2}{b^2}\right) + p_{att}b^2 - pr^2\right) \qquad r \geq b$$

Here $h = w(r = 0)$. Applying the boundary condition $w(r = a) = 0$, we get

$$h = \frac{1}{4S}\left(pa^2 - p_{att}b^2\left(1 + \mathrm{Log}\left(\frac{a^2}{b^2}\right)\right)\right) \tag{5.6}$$

Substituting eq. (5.6) in eq. (5.5) gives finally:

$$w(r) = \frac{1}{4S}\left(p(a^2 - r^2) - p_{att}(b^2 - r^2) - p_{att}b^2\text{Log}\left(\frac{a^2}{b^2}\right)\right) \qquad r < b \tag{5.7}$$

$$w(r) = \frac{1}{4S}\left(p(a^2 - r^2) + p_{att}b^2\text{Log}\left(\frac{r^2}{a^2}\right)\right) \qquad r \geq b$$

To determine S, we assume that the membrane is in an equi-biaxial state. This means that the incremental radial (ϵ_r) and tangential strains (ϵ_t) are given by $\epsilon_r = \epsilon_t = \frac{S_r}{Et/(1-v)}$ and recalling eqs. (3.2):

$$\epsilon_r + \epsilon_t = \frac{du}{dr} + \frac{u}{r} + \frac{1}{2}\left(\frac{dw}{dr}\right)^2 = \frac{2\,S_r}{Et/(1-v)} \tag{5.8}$$

Integrating eq. (5.8) with respect to an area element $2\pi r dr$ over the interval $(0, a)$, leads us to an average measure of S_r.

$$\int_0^a d(ur) + \int_0^a \frac{r}{2}\left(\frac{dw}{dr}\right)^2 dr = \frac{2\,S_r}{Et/(1-v)}\int_0^a r dr$$

The first integral on the LHS is zero due to the boundary conditions and evaluating the rest gives us:

$$S_r\,S^2 = \frac{Et}{32\,a^2(1-v)}\left((p - p_{att})^2 b^4 + p^2\left(a^4 - b^4\right) + p_{att}^2 b^4\text{Log}\left(\frac{a^4}{b^4}\right)\right.$$
$$\left. - 4\,p\,p_{att}b^2\left(a^2 - b^2\right)\right) \tag{5.9}$$

We know that by definition $S_r = S - S_0$. Hence for a given a, b, Et and v, by eliminating S from eqs. (5.6) and (5.9), we get an equation relating h with S_0, p_{att} and p. When we specify S_0 and p_{att}, this yields an expression for the load-deflection behavior i.e., p as a function of h or vice-versa.

$$\frac{Et}{32\,a^2(1-v)}\left(\left(p-p_{att}\right)^2 b^4 + p^2\left(a^4-b^4\right) + p_{att}^2 b^4 \mathrm{Log}\left(\frac{a^4}{b^4}\right)\right.$$
$$\left. -4\,p\,p_{att}b^2\left(a^2-b^2\right)\right)$$
$$+\left(S_0\left(\frac{1}{4h}\left(pa^2 - p_{att}b^2\left(1+\mathrm{Log}\left(\frac{a^2}{b^2}\right)\right)\right)\right)^2\right)$$
$$=\left(\frac{1}{4h}\left(pa^2 - p_{att}b^2\left(1+\mathrm{Log}\left(\frac{a^2}{b^2}\right)\right)\right)\right)^3 \tag{5.10}$$

The pull-in instability, by definition, occurs when:

$$\frac{dp}{dh} = 0 \tag{5.11}$$

When eqs. (5.10) and (5.11) are solved simultaneously at given p_{att} and S_0, the solution gives us p_c and h_c – the critical pressure and the critical separation at which the pull-in instability occurs. In the experiment, h_c is measured while p_{att}, S_0 and p_c are unknown. Consistent with the vdW potential for a layer of atoms with a semi-infinite substrate given by eq. (5.3) and neglecting the repulsive term, we assume p_{att} is given by (β is a constant):

$$p_{att} = \frac{\beta}{h^4} \tag{5.12}$$

On the other hand if the attractive forces are assumed to be caused by purely electrostatic interactions, then we use (α is a constant):

$$p_{att} = \frac{\alpha}{h^2} \tag{5.13}$$

Using either eq. (5.12) or (5.13) we can replace the unknown p_{att} in eqs. (5.10) and (5.11) with an unknown constant β or α. Thus by specifying S_0 and having measured h_c, we can determine p_c and β (or α).

5.3.2 Effect of Interfacial forces on Pressurized Graphene - Simulations
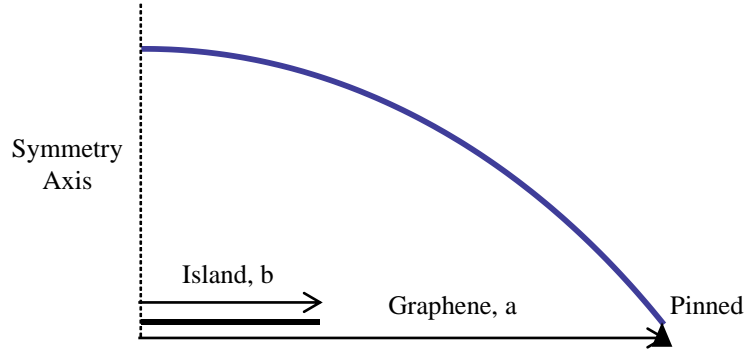
Figure 5.4 Schematic showing the axisymmetric finite element model consisting of a rigid fixed island and the graphene membrane pinned on the outer boundary

To validate the analytical model, we carried out finite element simulations of the experimental configuration using the finite element software Abaqus where we remove the assumptions used to develop the analytical model. The model used in the simulations is as shown in Fig. 5.4. It consists of a graphene membrane pinned at the outer boundary and a substrate (island) with which the membrane interacts. Axisymmetric shell elements (that permit both bending and membrane behavior) are used and the Young's modulus (E), thickness (t) and Poisson's ratio (v) are set to 1 TPa, 0.34 nm and 0.16 respectively. The outer edge of the membrane is pinned and the substrate/island is modeled as a fixed analytical rigid body. A prescribed initial tension (S_0) is applied and the attractive interactions between the island and the membrane are modeled as surface-to-surface contact/adhesive interactions with the island being the master surface. The contact interaction properties are supplied through the user subroutine "UINTER" of Abaqus. The slave nodes experience a stress (σ_z) in the vertical direction given by,

$$\sigma_z = -\frac{\beta}{w^4}$$

Here, β is the interaction parameter and σ_z plays the same role as that of p_{att} for vdW interactions; while w is the deflection of the node measured from the substrate. Both σ_z and w are functions of the radial position, in contrast to the analytical model where they are assumed to be independent of position.

The simulation is split into two steps – both static steps with nonlinear geometric effects included. In the first step, the contact/adhesive interactions are suppressed and the membrane is allowed to deform upwards under the influence of a uniform pressure load acting on the entire area of the suspended membrane. The magnitude of this load is set such that the deflection is just high enough to neglect the interaction pressure if the interactions were not suppressed. This simulates the state of affairs at the beginning of the experiment before the gas begins to leak from the cavity. In the second step, which is a Static-Riks step, a second uniform pressure load is added the maximum magnitude of which is the same as the previous pressure load but in the opposite direction and the surface interactions between the substrate and the membrane are switched on. Hence, apart from the force due to the contact interactions, the membrane has the uniform pressure load from the previous step and a uniform pressure in the opposite direction whose magnitude is given by the load proportionality factor (calculated by the Riks procedure). The superposition of these two uniform pressure loads mimics the leaking of the gas in the experiment. As the simulation progresses, the load across the membrane decreases and it comes closer to the substrate. This increases the interaction between the island and the membrane. The results of this step are plotted in Fig. 5.5a,c (solid curves) along with the analytically calculated results (dashed curves) with two different geometries. In both the geometries, the outer diameter is taken to be 3 μm while the diameter of the island is set to 0.5 μm and 1.5 μm respectively. Other parameters are set to S_0 = 0.07 N/m and β = 0.02 nN-nm^2. It can be seen that in the simulations the pressure load across

the membrane initially decreases until a limit point is reached and then it starts increasing. In reality, if the pressure is reduced below the pressure at the limit point, the interaction forces takeover and the membrane is pulled in. In other words, the membrane jumps into contact with the island deforming into an annular bulge.
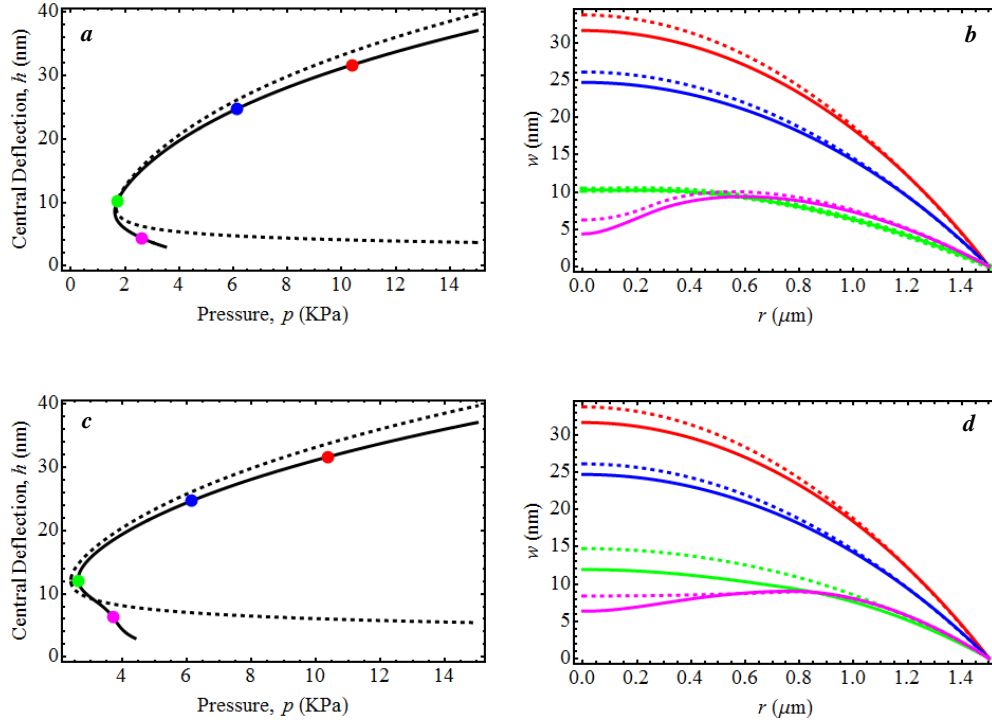
Figure 5.5 (a) Plots comparing p vs h behavior as obtained from the FE simulations (solid curve) and the analytical calculations (dashed curve) with a = 1.5 μm, b = 0.25 μm, Et = 340 N/m, ν = 0.16, S_0 = 0.07 N/m and β = 0.02 nN-nm², (b) The deflection profiles at different pressures (solid – FE, dashed – Analytical) (Red – 10.38 kPa, Blue – 6.12 kPa, Green – 1.72 kPa and Magenta – 2.61 kPa). For convenience, the corresponding points on p vs h plot are also shown. (c) and (d) The same as (a) and (b) except b = 0.75 μm. The different pressures used in this case are: Red – 10.39 kPa, Blue – 6.14 kPa, Green – 2.63 kPa and Magenta – 3.70 kPa.

When a = 1.5 μm and b = 0.25 μm, the pull-in pressure (p_c) and central deflection (h_c) are 1.63 kPa and 8.06 nm respectively, as obtained from the FE simulation. While the analysis gives values of p_c = 1.67 kPa and h_c = 9.21 nm for the same geometry. Similarly with a = 1.5 μm and b = 0.75 μm, from simulation p_c = 2.63 kPa and h_c = 11.94 nm whereas from theory p_c = 2.39 kPa

and h_c = 12.10 nm. This shows that the analytical result gives a fairly accurate description of the physical phenomena.

We also compared the deflection profiles at different pressures as obtained from the FE simulations (solid curves) and as predicted by the theory (dashed curves) in Figs. 5.5b and 5.5d. Away from the limit point and when the central deflection is high (red and blue curves), the membrane essentially behaves like a uniformly pressurized membrane with a nearly spherical bulge. As the membrane comes closer to the island (as the system approaches the limit point), the increasing strength of interactions between the membrane and the island deform the membrane locally over the region above the island. This local deformation manifests as flattening of the membrane just above the island as shown in Figs. 5.5b,d (green curves). The magenta colored curves shown in Figs. 5.5b,d are the deflection profiles of experimentally inaccessible configurations. These can only be realized through very careful control of displacement or pressure. In these configurations, the localized membrane deformation above the island is more accentuated and no longer parallel to the island. The theory does predict qualitatively this phenomenon beyond the limit point but due to the assumption of uniform p_{att}, the predicted behavior diverges away from the FE simulation results as is clearly evident in the p versus h plots.

In conclusion, the assumptions used in developing the theory do not really limit its ability in describing the pull-in phenomenon accurately. Since the underlying assumptions in the theory are not about the nature of the interactions, the simulations done similarly with any other inverse power law instead of the vdW type of interactions should in principle agree with the theory.

5.4 Experimental Results
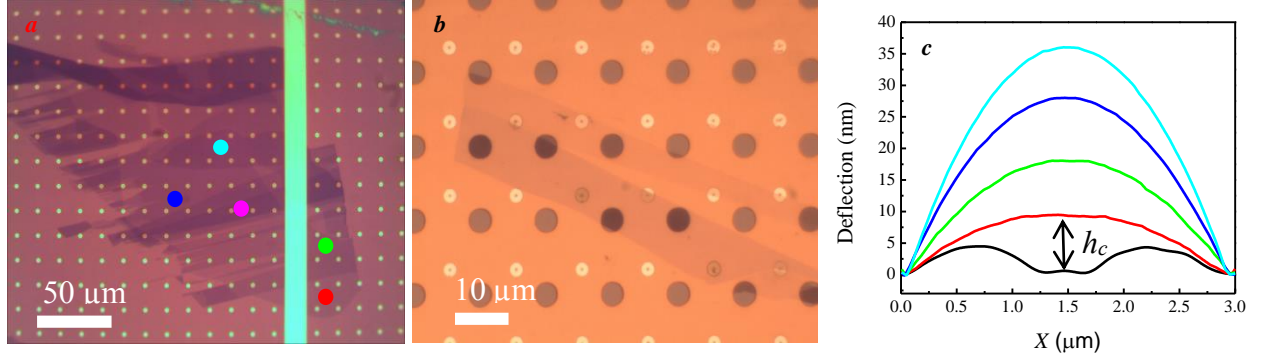
Figure 5.6 (a) Optical image showing one of the graphene flakes with devices on which measurements were done. The colored circles denote the number of layers confirmed using Raman spectroscopy (red-1 layer, green-2 layers, blue-3 layers, and cyan-4 layers, magenta-5 layers). (b) Optical image of few layer graphene flake on Au substrate. (c) A series of AFM line cuts through the center of a pressurized graphene membrane during pull in. The outer radius, 2a = 3.0 µm, and inner radius, 2b = 0.50 µm.

Some of the devices used in this experiment are as shown in the optical images in Figs. 5.6a and 5.6b on SiO_x and Au substrates respectively. We measured the pull-in distance (h_c) using the process described in section 5.2 using an AFM in real time, initially for 34 devices with varying number of layers of graphene on SiO_x (1 layer -13, 2 layer – 8, 3 layer – 5, 4 layer – 5 and 5 layer – 3) but with the same geometry $2a = 3.0$ µm and $2b = 0.50$ µm . A series of AFM cross sections are shown in Fig. 5.6c. As the gas leaks out, the membrane deformation goes from the cyan to green through the blue colored curve. The red curve is the deflection profile right before the membrane pulls-in towards the island. Immediately after the pull-in, the membrane assumes the annular bulge deflection profile shown in black. The difference in the central deflection for the red and black colored curves i.e., the central deflections right before and after the pull-in is taken to be the pull-in distance, h_c. We assumed p_{att} to be exclusively due to either vdW forces given by eq. (5.12) or electrostatic forces described by eq. (5.13). We cannot directly measure S_0 so we assume values in the range of $S_0 = 0.03$ - 0.15 N/m with an average values of $S_0 = 0.07$ N/m,

consistent with numerous experimental measurements for exfoliated suspended graphene membranes with a similar geometry.[22,78,79]

So in each case, using an estimate of $S_0 = 0.07$ N/m, describing p_{att} with either eq. (5.12) or eq. (5.13) and measured h_c, we solve eqs. (5.10) and (5.11) to get p and β or p and α. The usual values of $Et = n \times 340$ N/m and $\nu = 0.16$ are used for the elastic properties for n layered graphene. The results are plotted in Fig. 5.7. Figure 5.7a shows the experimental observations, while Figs. 5.7b and 5.7c show the average of calculated values of β and α for each n layered graphene membrane device along with standard deviation. In the case of vdW forces, the interaction parameter β varies almost linearly with n. It has an average value of about 0.02 nN-nm^2 for monolayer and about 0.09 nN-nm^2 for graphene with 5 layers. The best linear fit with a slope of 0.017 nN-nm^2/layer is also plotted in Fig. 5.7b. On the other hand, we also see that the magnitude of electrostatic interaction parameter α scales almost linearly with n from 0.48 pN to 1.71 pN. This kind of scaling can be justified in the case of the vdW interactions but not for electrostatic interactions. The reasons for this assertion follow later on in this section.
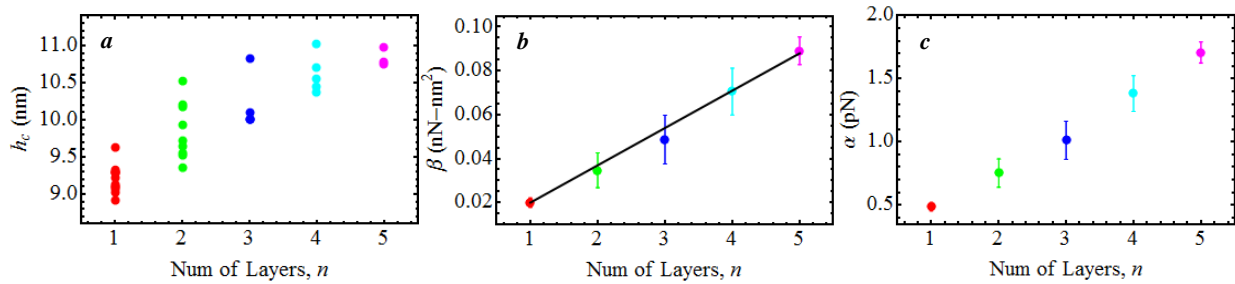
Figure 5.7 (a) Pull in distance, h_c, vs. number of layers for devices with $2a = 3.0$ μm and $2b = 0.50$ μm. (b) The calculated values of β vs. number of layers using the data in (a) assuming $p_{att} = \beta/h^4$ and $S_0 = 0.07$ N/m. A best fit line through the data is also shown which has a slope of 0.017 nN-nm^2/layer. (c) The calculated values of α vs. number of layers using the data in (a) assuming $p_{att} = \alpha/h^2$ and $S_0 = 0.07$ N/m.
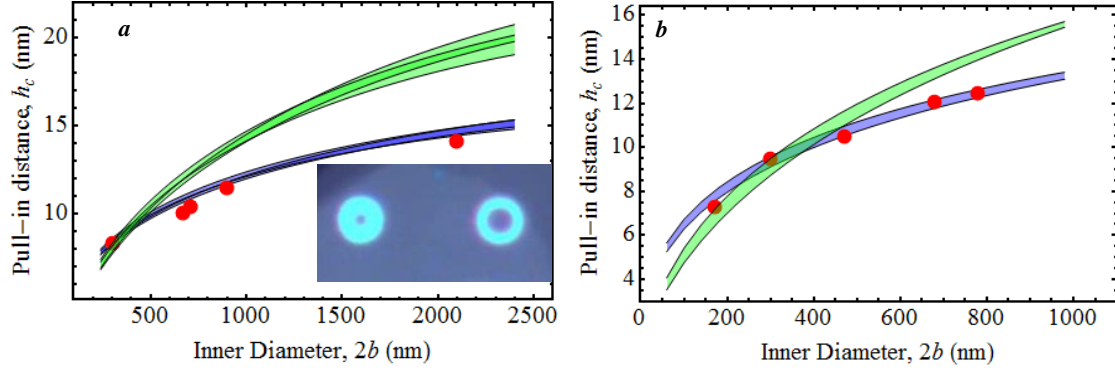
Figure 5.8 Pull in distance, h_c, vs. inner diameter, $2b$, for (a) 1 layer (b) 2 layer graphene membranes with identical/similar outer diameter but different inner diameters. The blue and green shaded lines are the calculated results for two different power law dependences $p_{att} = \beta/h^4$ (black) and $p_{att} = \alpha/h^2$ (blue) with $S_0 = 0.03 - 0.09$ N/m. The inset shows two devices with different inner island diameters.

To further give strength to our assertion that the attraction is due to vdW interactions, we performed pull-in experiments with different geometries where we fixed the outer diameter and varied the inner diameter. The pull-in distance for five such bi-layer devices with the same outer diameters ($2a = 5.2$ µm) and different inner diameters ranging from 170 nm to 680 nm are plotted in Fig. 5.8b against the inner diameter $2b$. Also plotted are the analytical predictions with vdW and electrostatic interactions in blue and green shaded regions respectively. These regions encompass all possible solutions with S_0 values between 0.03-0.09 N/m. The calculated average α and β values as shown in Figs. 5.7b,c are used in the analytical calculations. The pull-in distance increases with increasing inner diameter. This is because at a fixed a, the stiffness of the system remains the same; while the total force exerted by the vdW interactions increases with the island diameter resulting in pull-in at a higher deflection. It can be seen that the experimental observations are explained better by vdW interactions than the electrostatic interactions.

Similar comparison is done with mono-layer graphene devices too in Fig. 5.8a. However here the outer diameter is not exactly the same, it varies from 4.7-5.3 µm. Even so, the region encompassed by the theoretical predictions for the pull-in distance on h_c-$2b$ plane is narrow

enough as shown in Fig. 5.8a (green – electrostatic, blue – vdW). The range of values for S_0 is also accounted for in the theoretical calculations. Again, the experimental observations are better explained by the vdW interactions.

The electrostatic interactions are believed to originate from patch potentials due to puddles of charged particles on the substrate. The charged particles can come from vacancies, charged absorbed/adsorbed particles etc. and their distribution is random. We believe that this induces image charges in graphene and a rough estimate for the resultant pressure due to electrostatic forces can be expressed as:

$$p_{att}^e = \frac{1}{4\pi\epsilon_0} \frac{q_e^2}{4h^2} \rho \tag{5.14}$$

Here, ϵ_0 is the vacuum permittivity, q_e is the electron charge, h is the separation and ρ is the average charge density. Comparing eq. (5.14) with eq. (5.13) tells us that α should be proportional to ρ. This implies that the from the experimental observations, if the forces between the graphene membranes and the island are due to electrostatic interactions, the charge density should scale with the number of layers and vary with the island diameter. This is highly unlikely. Hence the attractive interactions should not have been caused by an electrostatic potential.

On the other hand, the vdW forces can be approximated to be additive interactions. Hence for an n layered membrane, we may write that the total interaction pressure as:

$$p_{att} = \sum_{i=1}^{n} \frac{\beta_m}{(h + it)^4}$$

Here $t = 0.34$ nm, is the thickness or the separation between graphene membranes and β_m the interaction parameter for monolayer graphene. As the separation h is of the order of 10 nm, it

90

means that for two layered graphene p_{att} is approximately twice that of mono-layered graphene. This is consistent with the experimental observations. Hence justifies our assertion that the interactions between the graphene membranes and the island are dominated by the vdW interactions. Of course, this kind of scaling has to stop when the graphene is very thick ($n > 10$ in this case).

To test the material dependence of the vdW interactions with graphene, we carried out experiments where we measured the pull-in distance between graphene and a gold coated annular ring structure made of SiO_x/Si. 2-5 layers graphene membranes (18 devices in 6 similar geometries from 4 chips) are measured. The pull in distance varies between 9 nm and 18 nm for devices with $a = 1.0$-1.75 μm and $b = 0.15$-0.6 μm, slightly larger than the measured pull-in distances for uncoated SiO_x posts of a similar geometry. Using the same theoretical analysis as with the graphene/SiO_x data, we determine the average value of β between the Au coated island and graphene to be 0.104 ± 0.031 nN-nm^2/layer; this is about an order of magnitude higher than that for graphene interacting with SiO_x (0.0179 ± 0.0037 nN-nm^2/layer). The graphene/Au value agree reasonably well with the theoretical predictions based on a Lifshitz formula of monolayered graphene interacting with gold at 15 nm separation, $\beta = 0.08$ nN-nm^2.[87] Similarly the average value of β obtained for graphene/SiO_x agrees closely with recent theoretical calculations for monolayered graphene and SiO_2 at 10 nm separations, $\beta = 0.0115$ nN-nm^2 for an intrinsic graphene doping density of 10^{16} m^{-2} at T $= 300$ K.[88]

The values of β/n for each device are plotted in Fig. 5.9 for both Au and SiO_x substrates. A comparison is made with the magnitude of the ideal Casimir force per unit area between two perfectly conducting plates through β_0, the ideal interaction parameter.[89]

$$p = \frac{\pi^2 \hbar c}{240} \frac{1}{h^4} = \frac{\beta_0}{h^4} \qquad (5.15)$$

Here, $\hbar$ is the reduced Planck's constant, c is the speed of the light and h is the separation.

Hence, $\beta_0 = \pi^2 \hbar c / 240 = 1.3$ nN-nm^2. Although in our case we have a plate interacting with a

semi-infinite space as opposed to two parallel plates, since the distance dependence is exactly the

same as the one we used in our calculations we directly compare β with β_0. The graphene/Au

value for averaged β is about 8% of the ideal value while graphene/SiO$_x$ value is about 1.4% of it.
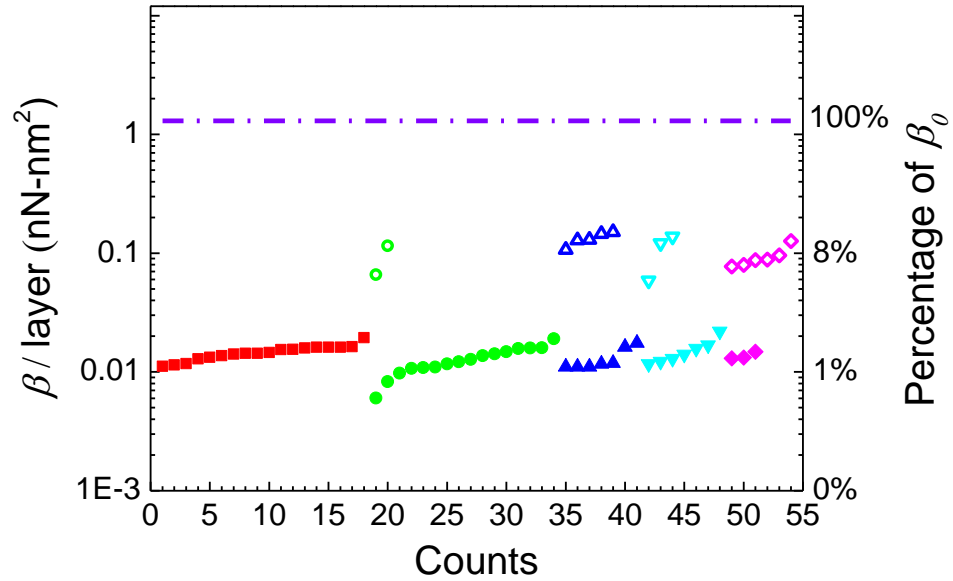
Figure 5.9 Measured β / Number of graphene layers between SiO$_x$ and 1 layer graphene (solid red squares), 2 layer graphene (solid green circles), 3 layer graphene (solid blue up triangles), 4 layer graphene (solid cyan down triangles), 5 layer graphene (solid magenta diamond), and β / number of graphene layers between Au and 2 layer graphene (hollow green circles), 3 layer graphene (hollow blue up triangles), 4 layer graphene (hollow cyan down triangles), and 5 layer graphene (hollow magenta diamond). The violet dash dot line indicates the value of β$_0$, where β$_0$ is the theoretical value for 2 perfectly conducting plates, β$_0$=π^{2}ℏc/240=1.3 nN-nm^2. The right axis corresponds to the percentage of the measured β / Number of graphene layers relative to β$_0$. The average and standard deviation of β / Number of graphene layers between SiO$_x$ and graphene are 0.0179 ± 0.0037 nN-nm^2 / layer, 1.38 ± 0.28 % of β$_0$. The average and standard deviation of β / Number of graphene layers between Au and graphene are 0.104 ± 0.031 nN-nm^2 / layer, 8.0 ± 2.38 % of β$_0$.

5.5 Summary

In conclusion, we measured long range surface forces between graphene and SiO_x and graphene and gold i.e. a dielectric and a metal. We found our measurements to agree with a form $p_{att} = \beta/h^4$, consistent with recently calculated values of vdW forces. We assumed that the attractive interactions are solely due to vdW forces, but in reality it might be a combination of vdW forces and electrostatic interactions. Due to our limited scope, we could not independently measure the electrostatic contribution. That said, the experimental setup used here uniquely allows for self-alignment of the membrane parallel to the substrate without the use of any sophisticated methods. Furthermore, we observed that the strength of the deduced surface force scales linearly with layer number as it should, suggesting a very limited influence of electrostatic interactions if any. This experimental configuration can also be used to measure the vdW force acting on other atomically thin, two-dimensional materials with a variety of substrates. These experiments can guide the development of nano-mechanical devices based on thin films, membranes and two-dimensional materials where these longer range forces are critical to their effective operation.

The theory developed to analyze the experimental results relies on a membrane model for the graphene sheets. It compares well with the finite element simulations where the assumptions in the analytical model are not included. The theory does a good job in describing the experimental results and trends and it suggests that it is possible to achieve pull-in through a fairly good range of values of h_c by varying a and b. We achieved a range of h_c=10-15 nm in this experiment. According to the theory, with increasing a, b and n (or Et), the pull-in distance increases; while with increasing S_0, the pull-in distance decreases. This can be explained thus - increasing a or decreasing S_0, makes the membrane more compliant leading to increased h_c. On the other hand, increasing b increases the force exerted by the interaction forces leading to increased h_c.

Increasing n, has a dual effect – it increases stiffness and the magnitude of the interaction forces (although this depends on n as well as geometry). The theory indicates that for similar geometries used in the experiments and small enough n, the pull-in distance increases linearly as is observed in the experiments.

6. Graphene Island Blister Nano-mechanical devices

6.1 Introduction
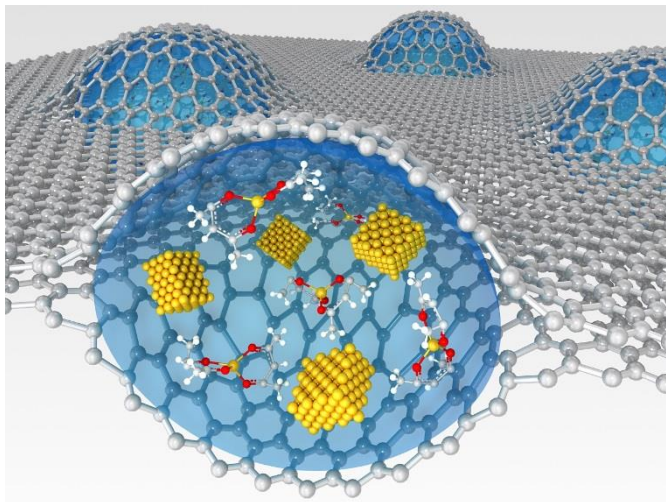
Figure 6.1 Graphene liquid cell – schematic showing two graphene sheets encapsulating a Pt growth solution (credit: KAIST)[90]

In the previous three chapters, we performed and modeled experiments using graphene nano-mechanical structures. Specifically, we used pressurized graphene blisters to measure elastic and adhesive properties of graphene membranes. These graphene nano-mechanical structures also find potential in nano-electro-mechanical systems (NEMS). Graphene, as mentioned before, with its ultimate thickness and low mass among other useful properties is an ideal candidate for NEMS applications. Graphene blisters of various shapes have found potential use in strain engineering[91] and sensors.[92] The most significant use of graphene blisters to date is a graphene liquid cell where graphene blisters provide a real-time window in transmission electron microscopy (TEM) to monitor chemical reactions in liquid phase.[93] A similar device is a hydrothermal graphene anvil cell to spectroscopically probe the dynamics of a supercritical fluids.[94] Here in this chapter, we propose a novel graphene NEMS device based on the island blister architecture that is described and used in the previous two chapters. This is really an extension of the device used in the previous

experiment where we overwhelm the van der Waals (vdW) interactions between graphene and the substrate by introducing electrostatic interactions to achieve pull-in instability. We then study the resulting interplay between adhesion, pneumatic pressure and electrostatic interactions while varying the strength of the electrostatic interactions to bring about changes in the graphene blister configuration. This is in contrast to what we described in Chapter 4 where we used the pneumatic pressure to control the shape.

6.2 Pressure Assisted Graphene NEMS Switch
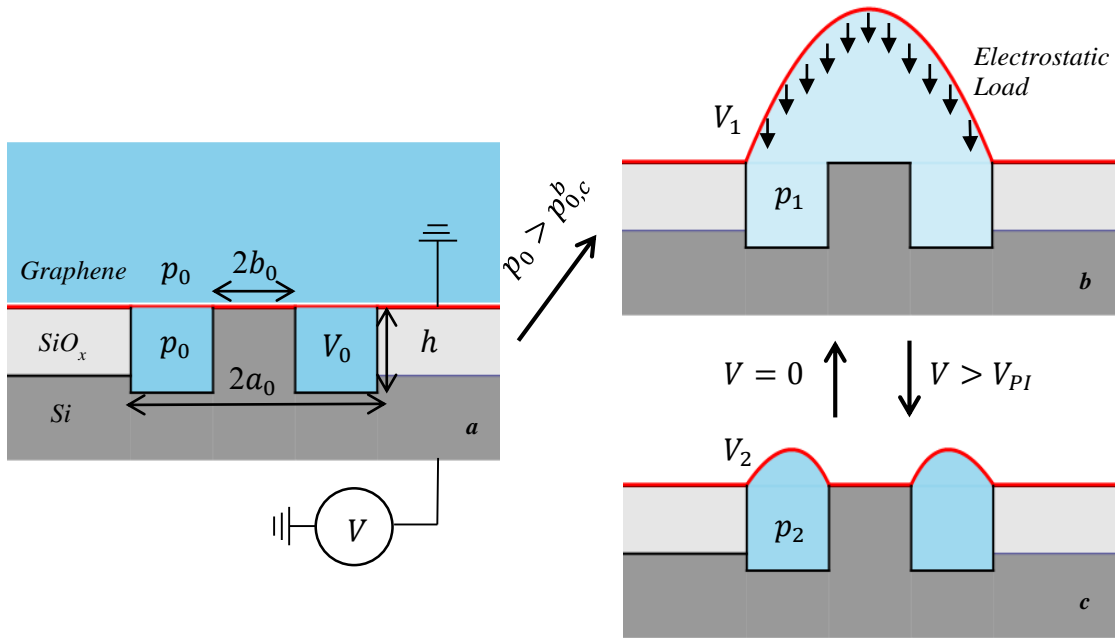
Figure 6.2 Schematics of the design and working principle of the pressure assisted graphene NEMS switch - (a) The device is charged with gas beyond the critical delamination pressure, $p_{0,c}^b$ (b) Graphene delaminates and the electrostatic load, V is switched on (c) If the voltage, V between graphene and the Si electrodes is beyond a critical value, V_{PI} graphene comes into contact with the Si electrode while compressing the gas and when the voltage is reduced to zero, the gas expands delaminating graphene to come back to configuration in (b).

We demonstrated in Chapter 4 island blisters which can be switched between different configurations at different pressure loads with the switching loads being determined by the

graphene-substrate adhesion energy. Pressure loads due to compressed gas, however, react slowly and high switching speeds with precise control cannot be achieved when compared to electrical signals. Furthermore, from a technological point of view addressing individual devices with a pressure load is difficult. Electrical loads, on the other hand, are much more responsive and all the graphene NEMS switches[27,28] in the literature to date have used electrical loads. These switches however suffer from stiction problems after only a few switching cycles. Here, we propose graphene NEMS switches with combined pressure and electrical loads that have the potential to overcome stiction.

6.2.1 Design and Working Principle

Figure 6.2 shows schematically the design and the basic working principle of our proposed device. As described in the previous chapters, we will start with graphene sealed axi-symmetric annular cylindrical micro-cavities of volume V_0. A key difference here is that there will be no thermal oxide on the surface of the micro-cavities. This allows the island to be electrically connected to the Si substrate. The Si substrate will act as the fixed electrode to which the control voltage, V will be applied. Graphene, on the other hand, will be grounded and will act as the flexible electrode. As before, the devices will be charged initially in a pressure chamber to a prescribed input or charging pressure, p_0. It is made sure that this charging pressure is greater than the critical delamination charging pressure from the island i.e. $p_0 > p_{0,c}^b$. This will allow the two electrodes to be separated from each other as shown in Fig. 6.2b when the devices are taken out of the charging pressure chamber. In this configuration, the switch is off as there is no electrical connection between the two electrodes. Let the pressure and volume of the gas molecules be denoted by (p_1, V_1) in this configuration. Introducing an electric field will create an attractive electric pressure load on the graphene membrane in a manner very similar to the vdW attractive

97

pressure described in the previous chapter except the magnitude here will be much larger. As the voltage is increased, the membrane will be pulled down towards the substrate while compressing the trapped gas molecules at the same time. When the voltage will reach a critical value, the membrane should pull-in and come into contact with the island (see Fig. 6.2c). Let us call this voltage the pull-in voltage denoted by V_{PI}. After pull-in, the graphene membrane should be adhering to the island forming an annular blister. Let the pressure and volume in this configuration be (p_2, V_2). In this state, the device is switched on due to the mechanical contact established between the two electrodes.

Reducing the voltage back to zero should let the compressed gas to expand and delaminate the membrane from the island assuming no loss of gas molecules throughout this entire process. When contact occurs due to pull-in, the electrostatic interactions inflate the adhesion energy between graphene and the substrate and when voltage is reduced to zero, the normal adhesion energy is restored and pressure, p_2 should be high enough to trigger delamination. After the pull-in, the membrane presumably takes an annular blister shape similar to the one described in Chapter 4. In this case however, we have an additional load in the form of electrostatic interactions which act against the pressure load exerted by the gas molecules. The volume under this blister then should be smaller than the annular blister discussed in Chapter 4. Assuming isothermal conditions and calculating V_2 using eq. (4.6), $p_2 \geq p_0 V_0 / V_2$ since V_2 is overestimated. Now, $p_{c,b} = p_0 V_0 / V_2$ (V_2 calculated using eq. (4.6)) is the equilibrium pressure inside the annular blister when $p_0 = p_{0,c}^b$. Hence p_2 is higher than the pressure required to trigger delamination given $p_0 > p_{0,c}^b$. After delamination we should get back to the configuration (p_1, V_1) assuming isothermal conditions persist. This process can be repeated as many times by changing the voltage, V between V_{PI} and zero thereby switching the devices between on and off states. In short, the device will be in:

(i)   On-state – when $V \geq V_{PI}$, the membrane is pulled-in while compressing the trapped gas and contact is established between the graphene and the underlying Si electrode.

(ii)   Off-state – when $V = 0$, the compressed trapped gas expands isothermally while delaminating the graphene and breaking the contact.

It is to be noted that it is implicitly assumed that during this whole process the gas molecules will not diffuse out of the micro-cavity. But in reality, there will be diffusion and hence the devices should stop switching back to off-state when the pressure is reduced considerably inside the micro-cavity. This can be overcome by recharging the devices in a pressure chamber back to p_0. We are aware that for technological applications a more comprehensive engineering solution needs to be worked out.

6.2.2 Finite Element Simulations – Model & Setup
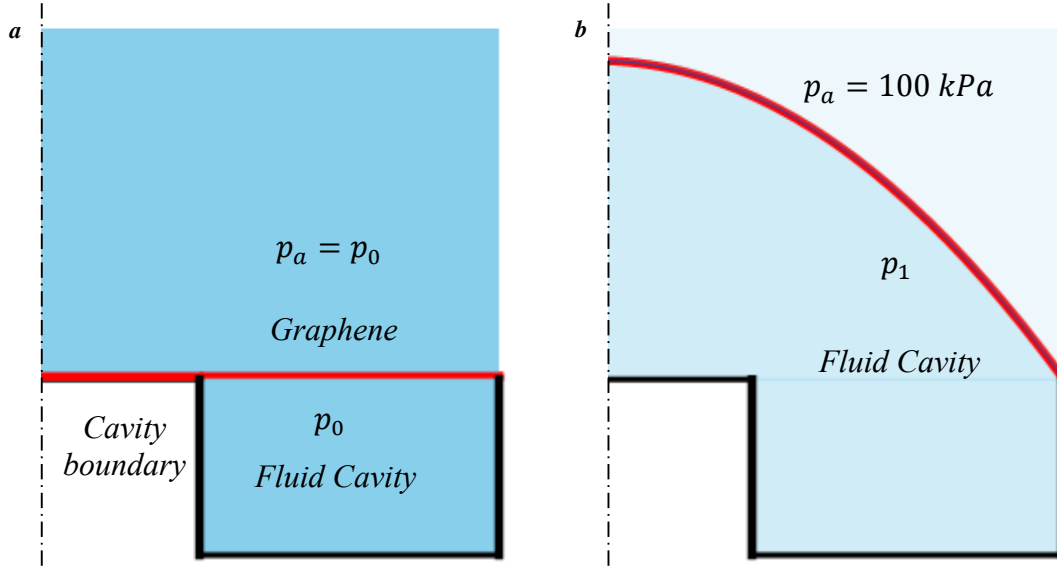
Figure 6.3 (a) Schematic of the initial condition of the FE model which mimics the initial configuration of the devices in the charging pressure chamber, (b) Schematic of the configuration achieved at the end of first step in FE simulations

The mechanics of the graphene membrane can in principal be described by the theory we developed in the previous chapter (Section 5.3). But the assumptions that we made there, namely that the membrane stress and the attractive pressure load are uniform, do not hold good in general in this case. So we took the route of finite element (FE) method to simulate the behavior and study the effect of the parameters in the problem (like geometry, adhesion energy and material properties) on the overall mechanics. Abaqus is our FE simulation tool of choice. We use a non-linear 1D model as shown in Fig. 6.3 in the FE simulations taking advantage of the axi-symmetric nature of the problem. The model consists of a rigid surface that mimics the surface of the micro-cavity (shown in black) and a linear elastic deformable surface which is the graphene membrane (shown in red). The graphene and the micro-cavity surfaces enclose a fluid cavity[95] which is a feature in Abaqus that simulates a fluid filled structure. Through this feature, Abaqus provides the ability to couple the deformation of the structure (membrane and the rigid micro-cavity in our case) to the thermodynamics of the fluid cavity (trapped gas in our case). The pressure and temperature of the fluid are the degrees of freedom for the fluid cavity. Hence, changing the pressure or temperature of the fluid cavity results in a deformation of the membrane and vice versa.

The membrane is pinned at the edge of the micro-cavity because in the device graphene will be adhering to the substrate and assumed to be constrained by the adhesive interactions. Values of 1 TPa, 0.16 and 0.34 nm are used for Young's modulus (E), Poisson ration (ν) and thickness (t) of graphene respectively which are all well accepted in the literature. Axi-symmetric shell elements with two nodes (SAX1) are used to mesh the membrane which account for both bending and stretching of graphene. The geometry of the micro-cavity (i.e. a, b, h) is allowed to vary in these simulations and the exact values used will be mentioned later.

The simulation is divided into two Abaqus static steps with non-linear geometric effects included. In the first step, the initial condition mimics the equilibrium configuration of the devices inside the charging pressure chamber when the membrane is flat and the pressure inside and outside the cavity is equal to p_0 (see Fig. 6.2a). We fixed the fluid-cavity temperature at 300 K throughout the simulation thus making the fluid cavity simulate ideal gas behavior under isothermal conditions. The pressure value of the fluid cavity is set at an initial value 20% higher than the critical island delamination pressure, $p_{0,c}^b$ for the given cavity geometry and an adhesion energy of 0.15 J/m². It is to be noted that the adhesive interactions between the membrane and the substrate are not simulated in this model. In this first step, the pressure outside the fluid cavity is gradually decreased from its initial value of p_0 to ambient pressure p_a (set at 100 kPa in these simulations). This sets up a pressure load on the membrane and it deforms to a spherical blister as illustrated in Fig. 6.3b. The pressure of the gas at the end (and along each point) of this step, p_1 is given by the pressure associated by Abaqus with the fluid cavity.

In the second step, we now introduce electrostatic interactions between the graphene and the substrate through DLOAD sub-routine of Abaqus. We assume that the electrostatic pressure load at a node that is deflected by $w(r)$ can be approximated by the equivalent pressure exerted between two parallel plate capacitors:

$$p_e(r) = \begin{cases} -\dfrac{1}{2}\dfrac{\epsilon_0 V^2}{w(r)^2} & r \leq b \\ -\dfrac{1}{2}\dfrac{\epsilon_0 V^2}{(w(r)+h)^2} & b < r \leq a \end{cases} \tag{6.1}$$

Here, a, b, h are the cavity outer radius, inner radius and depth respectively, ϵ_0 is the vacuum permittivity and V is the voltage between the two electrodes. The value of V is gradually increased

linearly with the step time from zero to a prescribed value. As the voltage is increased, the membrane gets pulled towards the micro-cavity surface and at a critical value of V we see pull-in.

6.2.3 Finite Element Simulations - Results

As mentioned before, we carried out a series of simulations each time varying the geometry of the micro-cavity. We varied the outer radius from 1 µm to 3 µm in steps of 1 µm. The inner radius is varied from 0.1 µm to a-0.5 µm i.e. for $a = 2$ µm, we varied the inner radius from 0.1 µm to 1.5 µm in steps of 0.1 µm. Similarly, we varied the depth of cavity from 50 nm to 500 nm in steps of 50 nm. The resultant set of geometries are similar to the ones we have used in the previous experiments and most of them can be readily fabricated. We eliminated the geometries that would result in delamination from the island as well as the outer boundary at our prescribed input pressure $1.2p_{0,c}^b$. This left us with 224 different geometries that were all simulated.
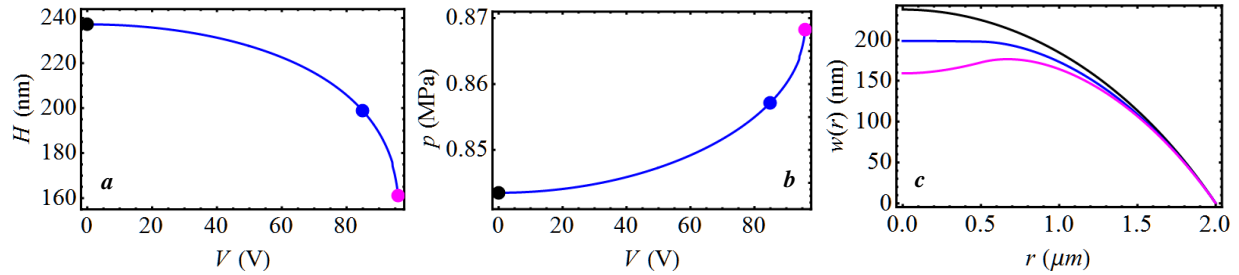
Figure 6.4 Plots showing (a) Central deflection, H and (b) Cavity pressure, p against the applied voltage, V for the geometry with a = 2 µm, b = 0.5 µm and h = 500 nm. The plots in (c) are the deflection profile of the membrane at 0 V (black), 85 V (blue) and at pull-in voltage, $V_{PI} = 95.9$ V (magenta). These points are highlighted in plots (a) and (b) with the same colors.

Let us look at an example where $a = 2$ µm, $b = 0.5$ µm and $h = 500$ nm. Figure 6.4 shows the results obtained from the FE simulations. It can be seen from Figs. 6.4a and 6.4b how the central deflection, H ($=w(0)$) of the membrane and the pressure inside the micro-cavity, p varies respectively. The pull-in voltage can be identified from Fig. 6.4a as the voltage at which the slope

of the $H \, v \, V$ curve approaches a large value i.e. a limit point where $dV/dH = 0$. Beyond this voltage, the simulations diverge and the pull-in voltage in this case is found to be 95.9 V. As the magnitude of the electrostatic pressure is the maximum on the island, the region of the membrane above the island is deformed the most as can be seen in Fig. 6.4c where the deflection profiles at different voltages are plotted. The membrane goes from a near spherical cap shape at 0 V (black curve) to being flat at the center at 85 V (blue curve) to having a "dip" at the center at the pull-in voltage (magenta curve). As the membrane comes closer to the island, the electrostatic pressure which is the strongest on the region of the membrane above the island deforms it in a very localized manner over the island causing the "dipping" behavior.
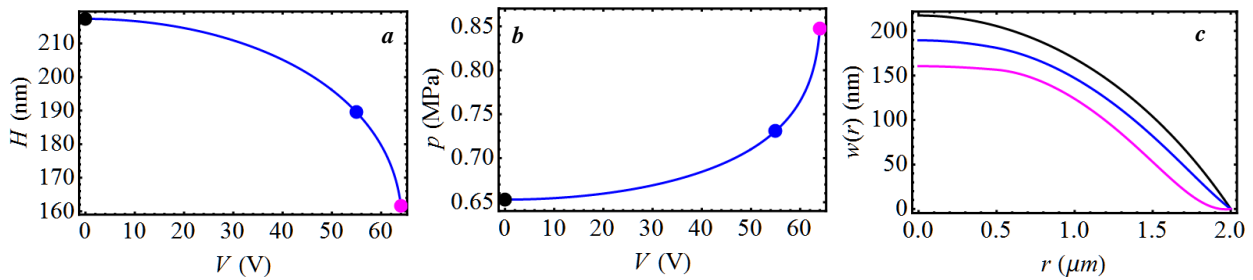
Figure 6.5 Plots showing (a) Central deflection, H and (b) Cavity pressure, p against the applied voltage, V for the geometry with a = 2 μm, b = 0.5 μm and h = 100 nm. The plots in (c) are the deflection profile of the membrane at 0 V (black), 55 V (blue) and at pull-in voltage, V_{PI} = 64.1 V (magenta). These points are highlighted in plots (a) and (b) with the same colors.

At the same a and b but with a different $h = 100$ nm, we see a slightly different pull-in behavior. The pull-in voltage in this case is lowered to about 64.1 V. As the depth of the cavity is decreased, the region of the membrane that is suspended over the cavity experiences a higher electrostatic pressure even as the region above the island experiences about the same electrostatic pressure. This causes localized deformation not just above the island but also close to the outer boundary of the micro-cavity as seen in Fig. 6.5c. As before, we plotted in Fig. 6.5c the deflection profiles at three different voltages. At 0V, the membrane has a near spherical cap shaped deflection

(black curve) which is still largely not perturbed at 55 V (blue curve). This is similar to what we have seen in the previous case in Fig. 6.4c. However at $V_{PI} = 64.1$ V, the membrane is deformed at the center as well along the outer boundary due to the electrostatic pressure in contrast to just at the center in the previous case. We noticed that this behavior is common to those devices where the depth of the cavity (≤ 100 nm) and the size of the island (compared to the outer radius) is small.
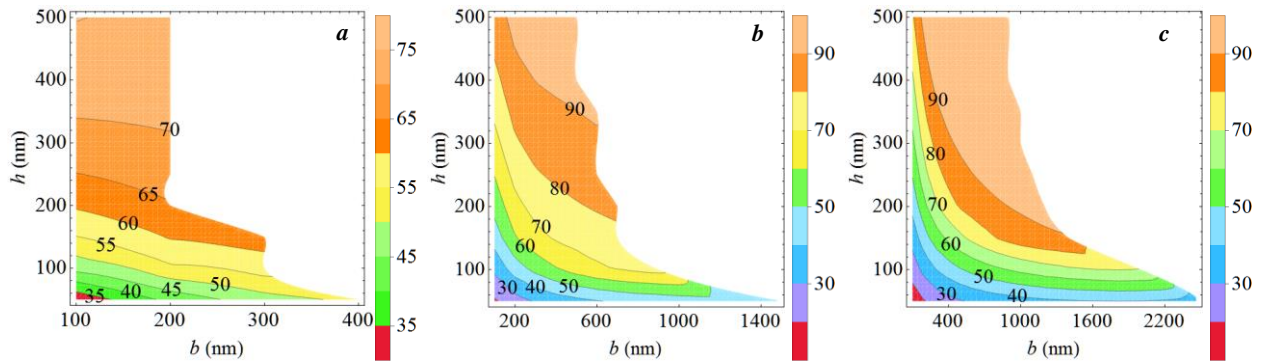
Figure 6.6 Contour plots showing the pull-in voltage variation in Volts with different inner radii, b and cavity depths, h at a fixed outer radius (a) a = 1 μm, (b) a = 2 μm, (c) a = 3 μm

The contour plots in Fig. 6.6 show the variation of pull-in voltage at different inner radii, b and cavity depths, h for a given outer radius, a. The white regions in each plot are the configurations that are not simulated for aforementioned reasons. It has to be noted that to the lower right part of the plots, there are artifacts from interpolation of the data which need to be ignored. From these plots, in general, we can conclude that increasing the outer radius, decreasing the inner radius or the depth of the cavity has the same effect of decreased pull-in voltage, V_{PI}. The decrease in V_{PI} with decrease in h can be explained by the increased electrostatic pressure (remember $p_e \propto 1/w(r)^2$). Decrease in h brings the membrane closer to the surface of the fixed Si electrode and thus increased electrostatic pressure.

Increasing the outer radius or decreasing the inner radius decreases the overall stiffness of the membrane/gas system thus decreasing the magnitude of the electrostatic pressure thereby the applied voltage needed to induce pull-in. Thus the devices can be scaled down so as to operate these switches at lower actuation voltages and increased device densities. But it has to be noted that with shallow cavities ($h\sim10$ nm), van der Waals forces will have an important role in the overall working of these devices which is not considered in these simulations. Additionally, the membranes might adhere to the bottom of the micro-cavity with shallow cavities which is not addressed here in these models.

The pressure assisted switch that we described here could be transformed to a pneumatic check valve. A check valve is a fluidic device that allows flow in one direction only. The transformation from a switch to check valve can be brought about just by etching a small hole (smaller than the island) on the graphene membrane that is on top of the island. When the device is switched off, the hole on the graphene membrane will be exposed and gas can flow freely. The flow rate, of course, will be determined by the pressure difference and the size of the hole. When the device is switched on i.e. when the membrane is attached to the island, the hole will now be closed due to the contact with the island and there will be no gas flow.

6.3 Summary

Taking advantage of the knowledge we gained in our experiments using graphene nano-mechanical structures, we proposed and analyzed (through finite element simulations) a pressure-assisted graphene NEMS switch. The switch makes use of trapped pressurized gas to overcome stiction that mars the development of reliable NEMS switches. We did a parametric study to determine the dependence of the switching voltage on the geometry of the devices. We found that the switching voltage can be reduced by scaling down the device dimensions.

7. Mechanisms of Graphene Adhesion

7.1 Introduction and Objective

Through chapters three and four, we understood adhesion of graphene at the micro-scale with the help of experiments. And we speculated at the end of chapter three that the adhesion energy might be effected by nano-scale topography of the substrate amongst other possible reasons. In this chapter, we focus on this roughness aspect and investigate the mechanics of adhesion at the atomistic scale.

Experiments like Lui et al's[96] have shown that graphene conforms to its substrates well (see Fig. 7.1) and other studies have realized that graphene's electronic properties can be altered in an interesting manner using mechanical strain.[39,91,97,98] Understanding what makes a graphene membrane conform well or otherwise will help in designing novel electronic devices that will take advantage of the strains that are developed as a result of adhesion.
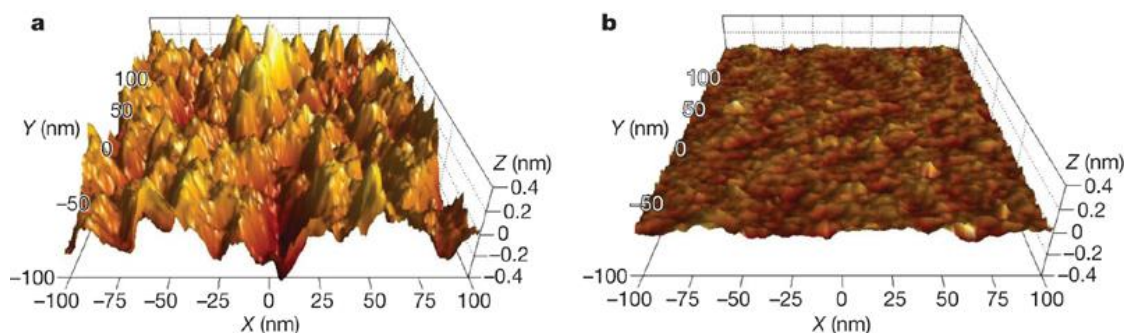
Figure 7.1 Three dimensional 200nm×200nm AFM height scan of graphene on (a) SiO₂ and (b) mica[96]

In the literature, the effect of substrate morphology on membrane (especially biological/soft membranes) adhesion has been extensively studied in the continuum setting.[65,66,99] The general strategy is to construct a free energy functional, *F* which includes the elastic bending

and stretching strain energies of the membrane (F_{ben} and F_{str}) along with the adhesion energy due to the membrane's interactions with the substrate (F_{adh}). If the substrate topography is described by a function $z_s(x, y)$, then mathematically the goal is to obtain the shape attained by the membrane, $z_m(x, y)$ so as to minimize the free energy functional, F.

$$F\big(z_m(x, y)\big) = F_{ben} + F_{str} + F_{adh} \tag{7.1}$$

$$
\begin{aligned}
F_{ben} &= \int dA \, \frac{1}{2} D\left(\left(\kappa_x + \kappa_y\right)^2 - 2(1 - v)\left(\kappa_x \kappa_y - \kappa_{xy}^2\right)\right) \\
F_{str} &= \int dA \, \frac{1}{2} C\left(\left(\epsilon_x + \epsilon_y\right)^2 - 2(1 - v)\left(\epsilon_x \epsilon_y - \epsilon_{xy}^2\right)\right) \\
F_{adh} &= \int dA_m \int dA_s V_{pot}(z_s, z_m)
\end{aligned}
\tag{7.2}
$$

Here, dA is the area element on undeformed membrane, dA_m and dA_s are area elements on the membrane and substrate respectively, D and C are bending and stretching rigidities respectively, κ_α and ϵ_α are the membrane curvature and strain along α ($\alpha = x$, y or xy) and V_{pot} is the inter-atomic interaction potential between the atoms of the substrate and the membrane. With any realistic potential functions, this is a complicated problem to solve even numerically. Hence the problem is usually reduced, with companion simplifications, to one dimension with a periodic pattern for the substrate like a sine function.

With the advent of 2D crystals like graphene and the ability to examine their morphology accurately using scanning probe techniques like AFM, this problem has been revisited recently in the literature[82–84,100] with essentially the same continuum approach as described. Each work made the necessary simplifications to arrive at their primary conclusion that the conformity of graphene on a given substrate depends on the substrate morphology, adhesion strength and the number of layers. It has been found that on 1D sinusoidally corrugated substrates, there is a snap through phenomenon where a graphene membrane goes from being non-conformal to conformal as the

amplitude or wavelength of the corrugation is changed. Here in this case, conformal is the configuration where the ratio of corrugation amplitudes of graphene membrane and the substrate is close to 1; while non-conformal is the configuration where it is close to zero. This phenomenon has also been observed experimentally.[101] Here in this chapter, we solve this same problem and others to obtain a general understanding of roughness effects on adhesion both analytically as well as numerically. The analytical approach we take here will differ from the existing ones in literature in how the adhesion energy is calculated and we compare our approach with other analytical approaches. The numerical approach will depart from the continuum setup altogether by using 'molecular mechanics/statics' simulations. This also allows us to look at the atomistic details of the mechanisms of adhesion of the graphene membranes while validating the continuum model.

7.1.1 Background – Molecular Mechanics

At length scales where continuum assumptions are not quite valid, we have grown to rely on numerical simulations involving modeling of systems from bottom up with atoms, molecules or particles forming the basic modeling units. In these simulations, the atoms (or the basic units) are allowed to interact through inter-atomic potentials (or force fields) which determine the elastic and thermal properties as well as the adhesive properties among others. The atoms with their potentials and the prescribed conditions are treated as a statistical thermodynamic system. There are two different approaches to these simulations – molecular dynamics and molecular mechanics (or statics). In molecular dynamics, the trajectories of atoms under the influence of inter-atomic potentials and any external stimuli are calculated over a period of time with the help of Newton's laws of motions. On the other hand in molecular mechanics, the total potential energy of the system (a function of the atom coordinates) is minimized using minimizing schemes like conjugate gradient or steepest descent to obtain a local minimum for the system under consideration with no

regards to its time evolution. The minimization procedure stops when the change in energy or the total force go below specified tolerances. Alternatively, it is terminated when there is only nominal change in the atoms coordinates even if the forces are non-zero.

The most commonly used inter-atomic potential for carbon based systems in the literature[102–104] is AIREBO[105] (Adaptive Intermolecular Reactive Empirical Bond Order). It includes a combination of potentials that describe short range covalent bonding (~ 2 Å) as well as longer range van der Waals bonding (> 3 Å) between carbon atoms. The van der Waals interactions between the atoms which leads to adhesion between surfaces is described by the Lennard-Jones 6-12 potential which takes the form:

$$V_{pot}(r) = 4\epsilon \left(\left(\frac{\sigma}{r} \right)^{12} - \left(\frac{\sigma}{r} \right)^{6} \right) \tag{7.3}$$

Here, r is the separation between two atoms, ϵ is the depth of the potential well and σ is the interatomic separation at which the potential equals zero. The default values for ϵ and σ are 2.84 meV and 3.4 Å respectively. The value ϵ can be varied to vary the depth of the potential well thereby the adhesion energy. Additionally, an independent LJ 6-12 potential can be added to the existing AIREBO potential to mimic increased adhesion energy. We used the software package LAMMPS (Large-scale Atomic/Molecular Massively Parallel Simulator) for all our simulations.[106]

7.2 Morphology of Graphene on Corrugated Substrates

7.2.1 Theory
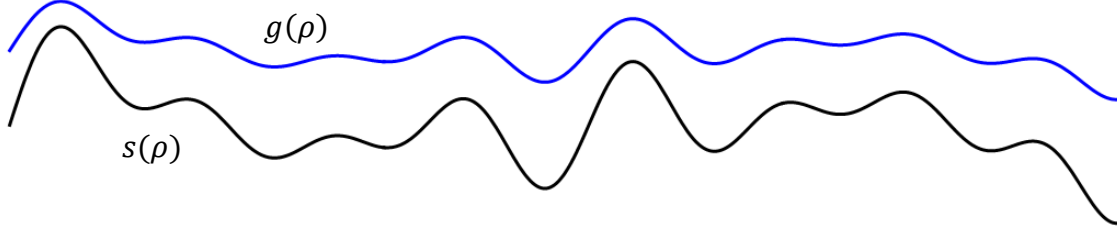
Figure 7.2 Illustration showing the morphology of a graphene membrane (blue) on a corrugated substrate (black)

To briefly describe the problem setup, we have a graphene membrane adhered to a rigid substrate as illustrated in Fig. 7.2. Given the functional form of the substrate surface $s(\rho)$, the goal is to find the functional form of the graphene membrane $g(\rho)$ (ρ being the position vector) with a given operant adhesive potential, V_{pot} between the substrate and graphene at the interface. This potential is assumed to be van der Waals interactions between atoms. Starting with Lennard-Jones 6-12 potential in eq. (7.3), one can then arrive at a continuum expression via direct integration for the potential, V_f that acts between two flat atomic surfaces separated by a distance h (the subscript f is to signify that this is the potential for two flat surfaces):

$$V_f(h) = \rho_A^2 \int_0^\infty 4\epsilon \left(\left(\frac{\sigma}{(r^2 + h^2)^{\frac{1}{2}}} \right)^{12} - \left(\frac{\sigma}{(r^2 + h^2)^{\frac{1}{2}}} \right)^6 \right) 2\pi r \, dr \qquad (7.4)$$

$$= -\gamma \left(\frac{5}{3} \left(\frac{h_0}{h} \right)^4 - \frac{2}{3} \left(\frac{h_0}{h} \right)^{10} \right)$$

Here, the integration is done in cylindrical coordinates with the radial coordinate being denoted by r and ρ_A is the areal density of the atoms. It can be easily verified that here $h_0 = \sigma$ is the equilibrium separation where the potential has a minimum and the force between the two flat surfaces is zero. The adhesion energy per unit area, γ is related to other terms via $\gamma = 6\pi \rho_A^2 \sigma^2 \epsilon / 5$.

For two arbitrarily shaped surfaces such as the ones shown in Fig. 7.2, the vdW potential is fully nonlocal i.e. it depends on the functional forms of the interacting surfaces ($V_{pot} = V_{pot}(g(\rho), s(\rho))$) and as mentioned before, is very difficult to calculate even numerically. Hence, we borrowed and extended the approach used by Swain and Andelman[65] where they used Derjaguin approximation to simplify the problem. Derjaguin approximation expresses the energy between two surfaces or bodies due to an adhesive interaction like vdW attraction, V_{pot} as a function of the local separation only. In mathematical terms:

$$V_{pot}\big(g(\rho), s(\rho)\big) \approx V_f\big(g(\rho) - s(\rho)\big) \tag{7.5}$$

Now, we can write the free energy of the system, $F\big(g(\rho)\big)$ as:

$$
\begin{aligned}
F\big(g(\rho)\big) &= F_{ben} + F_{adh} \\
&= \int dA \frac{D}{2}\left(\big(\kappa_x + \kappa_y\big)^2 - 2(1-\nu)\big(\kappa_x \kappa_y - \kappa_{xy}^2\big)\right) + \int dA \, V_f\big(g(\rho) - s(\rho)\big)
\end{aligned}
\tag{7.6}
$$

Here the contribution due to stretching is neglected completely as it is assumed that the interfacial friction is very small and the graphene membrane should be able to slide on the substrate quite freely. The Derjaguin approximation in effect replaces the surfaces with a series of parallel flat plates and calculates the total adhesion energy by adding the interaction potentials between these sets of parallel plates. Even with these simplifications the potential is still not tractable to solve for $g(\rho)$. Swain and Andelman expanded the integrand in the second integral about the equilibrium separation h_0 to the second order:

$$V_f\big(g(\rho) - s(\rho)\big) = V_f(h_0) + \frac{d^2 V_f(h)}{dh^2}\Big|_{h=h_0} \frac{(g - h_0 - s)^2}{2} \tag{7.7}$$

Here they assumed that the mean height of the substrate is zero and that of the membrane is h_0 and that $g - h_0 - s \ll 1$. We extend this further by expanding the potential about yet to be determined equilibrium separation h to an arbitrary number of terms, n $(z(\rho) = g(\rho) - h)$:

$$V_f\big(h + z(\rho) - s(\rho)\big) = V_f(h) + \sum_{i=1}^{n} \frac{d^i V_f(h)}{dh^i} \frac{(z - s)^i}{i!} \tag{7.8}$$

Swain and Andelman using eq. (7.7) showed that sinusoidal substrates allow for sinusoidal membrane profiles and a one-to-one correspondence does not hold good for arbitrary functions. We assumed that this still holds good here. Sinusoidal surfaces, though a poor representation of randomly rough surfaces, enable us to simplify the analysis while capturing most of the physics qualitatively. Let us first deal with one dimensional sinusoidal surfaces i.e. $s(x) = c \operatorname{Sin}[q\,x]$ where c and q are the amplitude and wave numbers of the sinusoid respectively. Hence assuming $z(x) = a \operatorname{Sin}[q\,x]$, the free energy per unit area is:

$$F(a, h) = \int_0^\lambda \frac{dx}{\lambda} \frac{D}{2} \left(\frac{d^2 g}{dx^2}\right)^2 + \int_0^\lambda \frac{dx}{\lambda} V_f(h + z - s) \tag{7.9}$$

$$= \frac{D}{4} a^2 q^4 + V_f(h) + \sum_{i=1}^{n} \frac{d^i V_f(h)}{dh^i} \frac{(a - c)^i}{i!} \int_0^{2\pi} \operatorname{Sin}[x]^i \frac{dx}{2\pi}$$

Here $\lambda = 2\pi/q$ is the wavelength and it is fairly straightforward to formulate the free energy as shown here using a computer algebra system (CAS) and then numerically optimizing gives us the equilibrium configuration of the membrane for any arbitrary one dimensional sinusoidal corrugation. The form of V_f allows us to calculate the integrals directly for this particular case (see Appendix A.3.1), thus allowing us to verify the accuracy of this series approach of ours where we use a series expansion of the adhesion energy contribution to the free energy.

112
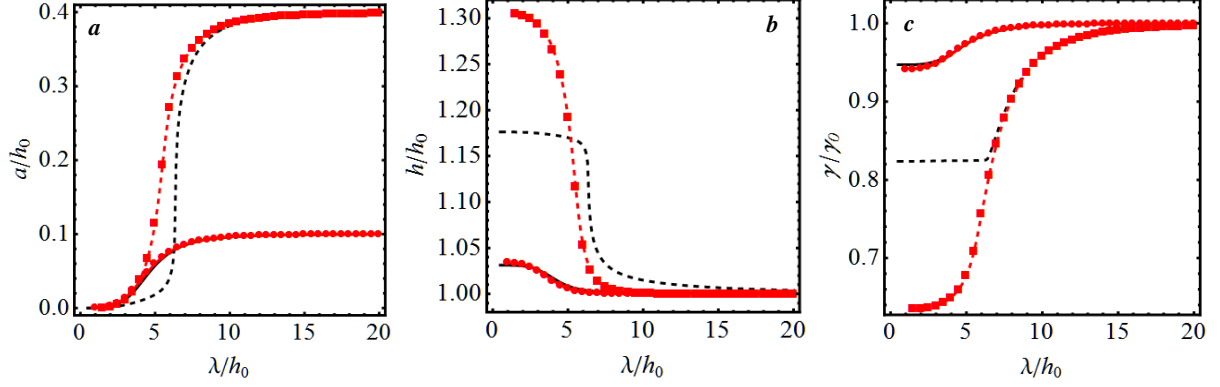
Figure 7.3 Plots comparing our calculations with those of Aitken and Huang: non-dimensional (a) Amplitude, (b) Mean separation and (c) Adhesion energy are plotted against the non-dimensional wavelength. The red curves (from optimization of eq. (7.9)) and the circle/square symbols (from direct integration) are our results while the black curves are the results of Aitken and Huang. Here the solid curves and circular symbols are calculations done with $c/h_0 = 0.1$; the dashed curves and square symbols are calculations done with $c/h_0 = 0.4$.

We compared the results from our calculations with those of Aitken and Huang[100] where they do not use the Derjaguin approximation but approximately calculate the adhesion energy from the non-local V_{pot} for sinusoidal surfaces. We used the same potential and parameters that were used in their paper for the purpose of this comparison. The potential they used is different from V_f in eq. (7.4); it accounts for interaction between a surface of atoms with a semi-infinite body. It is straightforward to replace V_f with the potential they used. The parameters used are $\frac{D}{\gamma h_0^2} = 6.94$ and

$\frac{c}{h_0} = 0.1$ or 0.4.

The results are shown in Fig. 7.3. The plots from left to right show the non-dimensional amplitude, mean separation and the adhesion energy as a function of the wavelength of the substrate. The membrane conforms to the substrate very closely at higher wavelengths while it is relatively flat at lower wavelengths. The transition from being conformal to flat occurs sharply and if the wavelength of the substrate corrugation can be changed continuously, the membrane should snap-in to or snap-out of close conformation with the substrate. This is due to the competition

between the adhesion and the bending strain. While the adhesive interactions pull the membrane towards to substrate, the bending strain prevents the membrane from completely conforming to the corrugated substrate. The final equilibrium configuration is attained as a balance between these two opposing tendencies is reached. At smaller wavelengths, the bending strain is too high leading to poor conformity and at higher wavelengths, bending strain is small enough for the membrane to achieve high conformity.

It can be seen that there is a good agreement in general between the three methods shown here – Aitken and Huang's (black curves), our method with F_{adh} calculated by direct integration (circle and square symbols) and our method where we use the expression in eq. (7.8) with 40 terms to calculate F_{adh}. For the lower amplitude ($c/h_0 = 0.1$, solid curves and circular symbols), the three methods give the exact same result; while for the higher amplitude ($c/h_0 = 0.4$, dashed curves and square symbols) though our two approaches still agree quite well, our results differ considerably from Aitken and Huang's results. At the higher amplitude, Aitken and Huang's calculations underestimate (overestimate) the mean separation (adhesion energy) compared to our calculations even as the amplitude predicted is quite similar. This might be attributed to the approximations used by Aitken and Huang ($c \ll h_0$) which limits the use of their method at high amplitudes ($c < 0.5h_0$) or to the Derjaguin approximation we used.

This method can easily be extended to 2D sinusoidal substrates as well, $s(x, y) = c \sin[q_x x] \sin[q_y y]$ where q_x and q_y are the wave numbers in x and y directions respectively. The free energy in this case, assuming the membrane will follow $g(x, y) = h + a \sin[q_x x] \sin[q_y y]$, will then be:

$$F(a,h) = \frac{D}{8}\left(q_x^2 + q_y^2\right)^2 a^2 + V_f(h) + \sum_{i=1}^{n} \frac{d^i V_f(h)}{dh^i} \frac{(a-c)^i}{i!} \left(\int_0^{2\pi} \text{Sin}[x]^i \frac{dx}{2\pi}\right)^2 \quad (7.10)$$

This looks very similar to the free energy expression in eq. (7.9) for 1D sinusoidal corrugations. Hence again by optimizing the free energy numerically to find a and h, we should be able to arrive at the equilibrium configuration of graphene membranes.

This approach can be generalized to work with a full or truncated Fourier series that involves multiple sine or cosine waves of different amplitudes and wavelengths in superposition. If the substrate is represented by the function $s(x) = \sum_{i=1}^{m} c_i \text{Sin}[q_i x] + d_i \text{Cos}[q_i x]$ and assuming the graphene membrane takes the form $g(x) = h + \sum_{i=1}^{m} a_i \text{Sin}[q_i x] + b_i \text{Cos}[q_i x]$, then the free energy per unit area in this case will be:

$$F(a_i, b_i, h) = \frac{D}{2} \sum_{i=1}^{m} \left(\frac{q_i^4 a_i^2}{2} + \frac{q_i^4 b_i^2}{2}\right) + V_f(h) \quad (7.11)$$

$$+ \sum_{j=1}^{n} \frac{d^j V_f(h)}{dh^j} \frac{1}{j!} \int_0^L \frac{dx}{L} \left(\sum_{i=1}^{m} (a_i - c_i)\text{Sin}[q_i x] + (b_i - d_i)\text{Cos}[q_i x]\right)^j$$

Here, c_i and d_i are the Fourier coefficients in the truncated Fourier series that represents the substrate while a_i, b_i and h are the same with regards to $g(x)$. The last term in the free energy expression can be calculated by expanding the integrand using multinomial theorem which results in an algebraic expression involving products of sine and cosines that can be easily integrated. However, the number of such terms and the complexity increases with m and n. An alternate expression can be found using complex Fourier series which is presented in the Appendix (see A.3.2). Also following this approach, similar expression for the free energy can be arrived at for two dimensional substrates represented by a full or truncated 2D Fourier series. With m terms in

the truncated Fourier series, the free energy has $2m+1$ unknowns which can be found as before by optimizing the free energy. Later we will use these free energies to numerically calculate the equilibrium membrane profiles for different corrugated substrates and compare the results with molecular mechanics simulations.

7.2.2 Simulations – 1D Sinusoidal Corrugations

We carried out molecular mechanics simulations initially with 1D sinusoidally corrugated rigid substrates where we varied the amplitude (c) and wavelength (λ) of the substrates in a systematic manner to determine the effect on the graphene membrane conformity. The simulation setup consists of a fictitious graphene-like substrate with just a single layer of atoms. The substrate atoms are pre-arranged in a sinusoidal manner with the desired amplitude and wavelength. The atoms in the graphene membrane interact via AIREBO potential which accounts for covalent bonding at short distances (~2 Å) and van der Waals (vdW) interactions at larger distances (> 3 Å) through a prescribed Lennard-Jones (LJ) 12-6 potential with a cut-off distance of 10.2 Å (the cut-off distance is the distance beyond which the interaction is zeroed). The whole initial setup is as shown in Fig. 7.4 with black colored dots denoting the substrate atoms and blue colored dots denoting the graphene atoms. Initially, the graphene atoms in a flat configuration are vertically set apart by 20.4 Å from the substrate well beyond the LJ cutoff distance so that there are no vdW interactions. Periodic boundary condition is applied along the width direction while the graphene atoms are free to move in the length direction. The substrate is made slightly longer than the graphene membrane to accommodate vdW interactions near the graphene membrane edges. The reason for choosing to represent the substrate with just one layer of atoms is primarily that it saves computational effort. It is also easier to setup in comparison to a substrate with bulk atoms and should be able to capture the essential physics even without any bulk atoms.
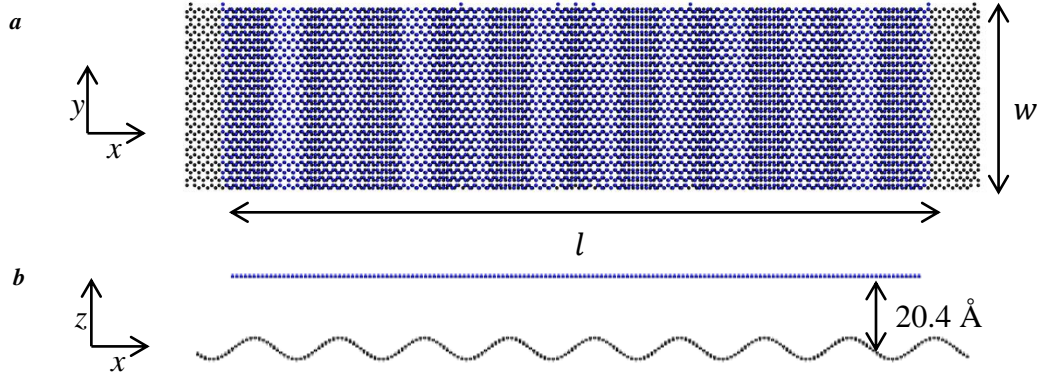
Figure 7.4 The initial configuration of the atoms (blue - graphene, black - substrate): (a) Top view (b) Side view with c = 3 Å and λ = 24 Å.
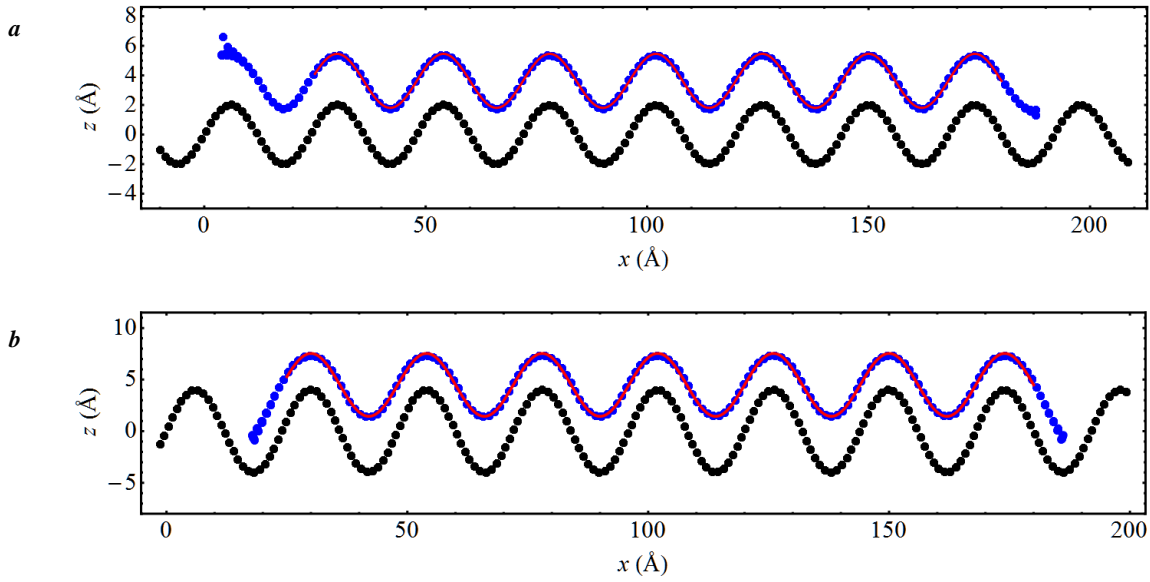
Figure 7.5 The final equilibrium configurations for (a) c = 2 Å and (b) c = 4 Å with l = 194 Å, w = 50 Å, λ = 24 Å and γ = 0.3 J/m2. The blue and black dots are atoms in graphene and the substrate respectively while the red curve is the fitted sine curve.

w (Å)	$c = 2$ Å			$c = 4$ Å		
	a (Å)	h (Å)	γ (J/m^2)	a (Å)	h (Å)	γ (J/m^2)
49.59	1.8249	3.6360	0.2656	3.0464	4.4910	0.1888
62.15	1.8249	3.6360	0.2641	3.0462	4.4911	0.1878
74.71	1.8262	3.6356	0.2633	3.0446	4.4918	0.1875

Table 7.1 The results of the simulations with varying widths for the graphene membrane with the length fixed at about l = 194 Å, λ = 24 Å and γ = 0.3 J/m²

After setting up the atoms, the interaction potentials and the boundary conditions, the graphene atoms are allowed to relax while fixing the substrate atoms. At the end of this minimization step, the graphene atoms in their relaxed configuration are moved closer to the substrate atoms by about 13 Å from the initial mean separation of 20.4 Å. The graphene atoms, now within LJ potential cut-off, start to interact with the substrate atoms while the substrate atoms are still rigidly fixed. Under the influence of these interactions, in what will be the second energy minimization step, the graphene membrane moves closer to the substrate until an equilibrium configuration is reached. The difference between the total energies at the end of the second and the first minimization steps gives the apparent adhesion energy; dividing it by the area of the graphene sheet gives apparent adhesion energy per unit area, γ. This is because at the end of the first minimization step, the graphene atoms are in a relaxed flat configuration and are not interacting with the substrate atoms; while at the end of the second minimization step the atoms are deformed and adhere to the substrate. Hence, the difference of energies of these two configurations gives us the apparent adhesion energy which in turn is the energy gained by the system due to adhesive interactions between the substrate and graphene atoms and the energy lost due to bending of the graphene atomic bonds.

All the simulations are performed at a temperature of 0 K, any effects of finite temperature are not considered here. We used conjugate gradient method for all the minimization steps. The initial set of simulations are performed with $\lambda = 24$ Å, $c = 2$ and 4 Å and for monolayer graphene while varying the length (l) and the width (w) of the graphene membrane. This exercise is done to make sure that the results are not sensitive to the size of the system. First, the width of the graphene sheet is varied from about 50 Å to 62 Å to 75 Å while keeping the length fixed at about 194 Å. For each simulation, assuming the graphene membrane takes the form $g(x) = h + a \, \mathrm{Sin}[\frac{2\pi}{\lambda} x]$,

the amplitude (a) and mean separation (h) for the graphene membrane are extracted (details in Appendix A.3.3) from the final equilibrium configuration along with the effective adhesion energy per unit area (γ). The results of these simulations are shown partially in Fig. 7.5 and tabulated completely in Table 7.1. The figure shows that the graphene atoms (blue dots) follows a sine curve (in red) very closely. From the table, it is clear that we get about the same result in each case even with fewer atoms when the width is about 50 Å.

l (Å)	$c = 2$ Å			$c = 4$ Å		
	a (Å)	h (Å)	γ (J/m^2)	a (Å)	h (Å)	γ (J/m^2)
193.7	1.8249	3.6360	0.2656	3.0464	4.4910	0.1888
290.4	1.8021	3.6398	0.2641	2.2880	4.9947	0.1643
387.1	1.8085	3.6367	0.2597	1.9052	5.2855	0.1497

Table 7.2 The results of the simulations with varying lengths for the graphene membrane with the width fixed at about w = 50 Å, λ = 24 Å and γ = 0.3 J/m²
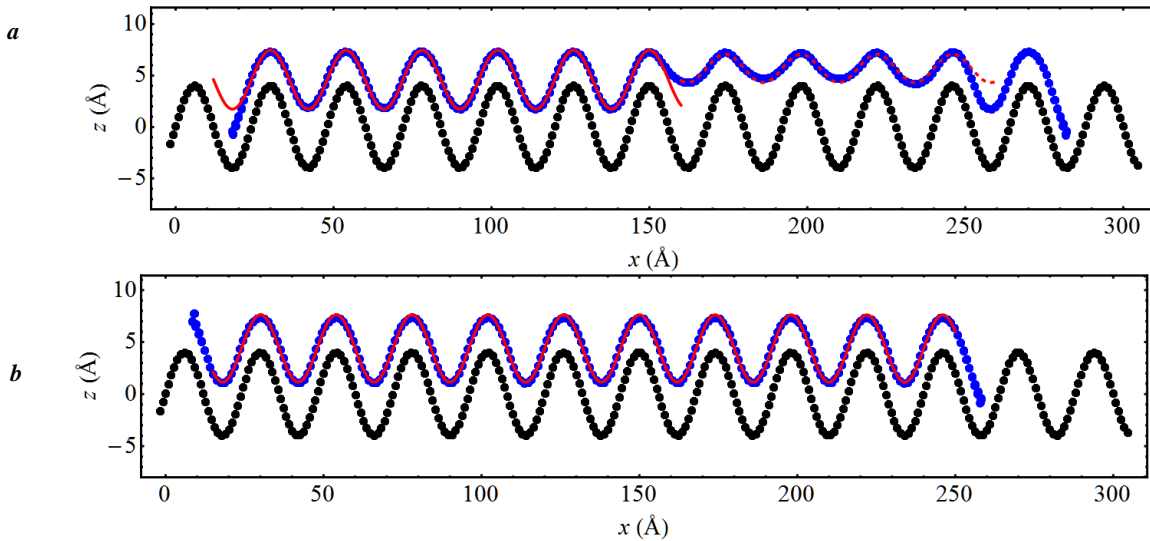
Figure 7.6 The final equilibrium configurations for a graphene membrane of l ≈ 290 Å with c = 4 Å, w = 50 Å, λ = 24 Å and γ = 0.3 J/m² – (a) with flat initial configuration, (b) with sinusoidal initial configuration. The blue and black dots are atoms in graphene and the substrate respectively while the red curves are the fitted sine curves.

Similar study is done with varying lengths for the graphene membrane while keeping the width fixed at about 50 Å. The results are shown partially in Fig. 7.6 and tabulated completely in Table 7.2. We can see that with $c = 2$ Å, the results are practically the same with different lengths; however with $c = 4$ Å, the results differ with the shorter graphene membranes conforming better than the longer ones. This is probably due to the inability of the energy minimization step to reach the absolute minimum. The graphene membrane reaches what might be an intermediate equilibrium configuration where the conformity is not quite uniform as seen in Fig. 7.6a for $l = 290$ Å case. The figure also shows the sine curve fitting done to the two different regions of the membrane in red and the solid curve is closer to the result obtained with shorter graphene membrane. To ascertain which of these two fitted sine curves with (a, h) = (2.86, 4.59) Å and (1.38, 5.69) Å corresponds to the actual minimum, we repeated the simulation with the graphene atoms initially along one of the aforementioned fitted sinusoidal curves instead of a flat shape. The simulations in each case produced results of (3.23, 4.39) Å and (3.11, 4.45) Å for the initial configurations of (2.86, 4.59) Å and (1.38, 5.69) Å respectively. These results are in turn are close to the one obtained for the shorter membrane i.e. (3.05, 4.49) Å.

In view of the above discussion and results shown in Tables 7.1 and 7.2, we concluded that we get about the same results with different lengths and widths for graphene. So we used $l \approx 194$ Å and w ≈ 50 Å for the rest of our simulations knowing that we lose very little in terms of accuracy. Now, we varied the wavelength, λ of the substrate from 12 Å to 36 Å in steps of 6 Å while keeping the amplitude, c fixed at either 1 or 2 Å. We also solve for the equilibrium configuration in each case using our theory where we used 1 eV for monolayer graphene membranes bending rigidity in line with the values found in the literature[48]. We arrived at this value using molecular mechanics simulations, the details of which are presented in the Appendix

(see A.3.4). The results of these simulations (red dots) are shown in Fig. 7.7 along with the theoretical calculations (black curves). We see good agreement between the simulations and the theory in general. As discussed before, we see here that with increasing wavelength the conformity of the graphene membrane to the substrate changes from poor to good leading to increase in the membrane amplitude, decrease in the equilibrium separation and increase in the adhesion energy.
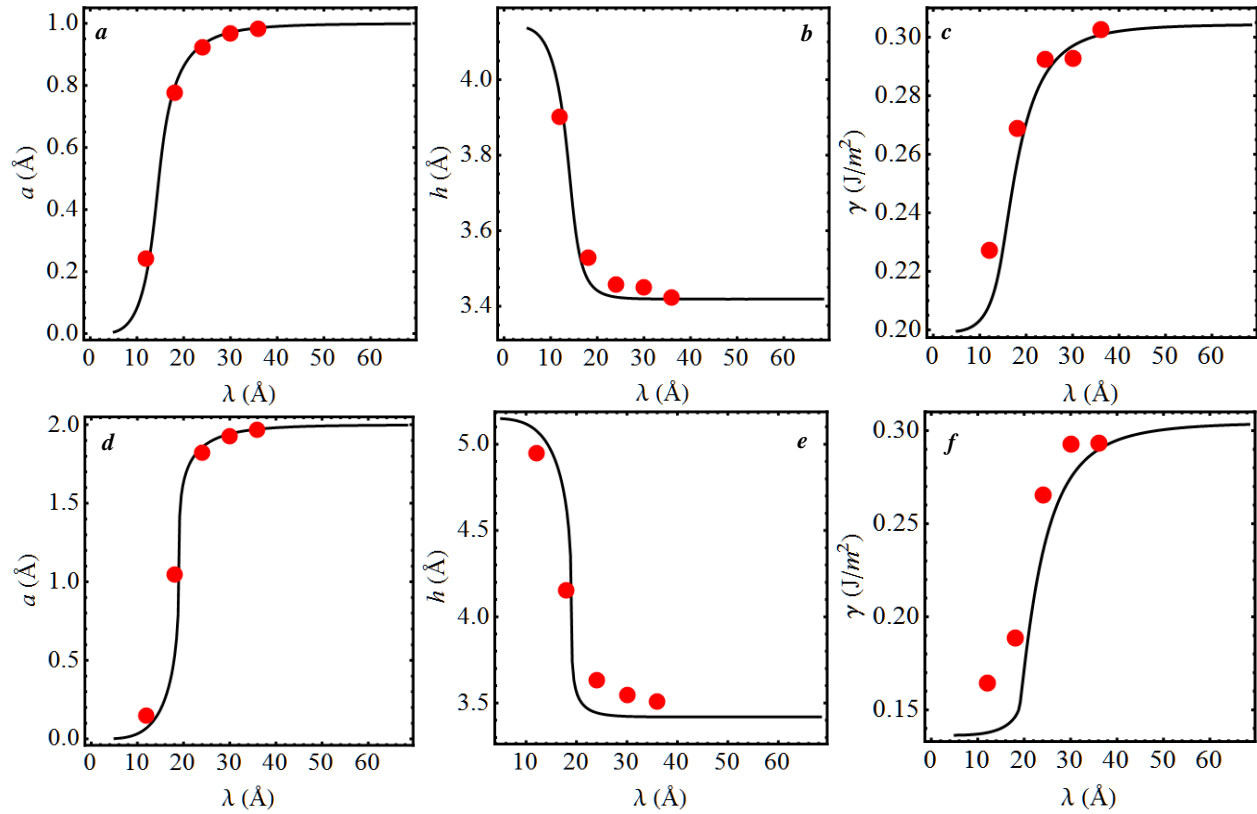
Figure 7.7 Plots showing the variation of equilibrium (a,d) amplitude, a, (b,e) separation, h and (c,f) adhesion energy, γ with the substrate wavelength, λ. The black curve is from our theory and the red dots are from the simulations. The top (a,b,c) and the bottom rows (d,e,f) show results for substrate amplitude $c = 1\,\text{Å}$ and $2\,\text{Å}$ respectively.
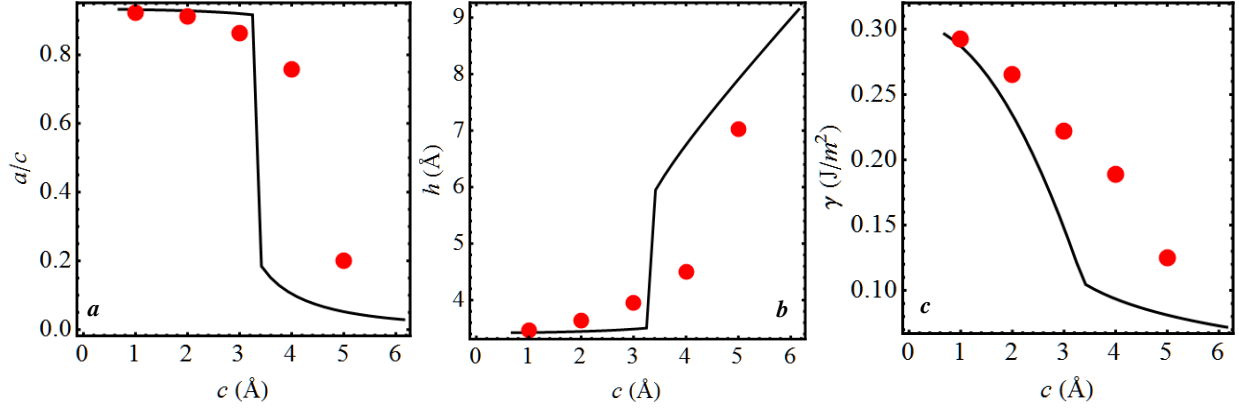
Figure 7.8 Plots showing the variation of equilibrium (a) amplitude, a (normalized with respect to substrate amplitude, c), (b) separation, h and (c,f) adhesion energy, γ with the substrate amplitude, c. The black curve is from our theory and the red dots are from the simulations. For these simulations, the substrate wavelength is fixed at $\lambda = 24$ Å.

We also carried out simulations where we varied the substrate amplitude, c while fixing the wavelength, λ and using the same values for l, w and γ as before. The results are shown in Fig. 7.8. Again it can be seen that the theory performs reasonably well at predicting the equilibrium configurations of the graphene membrane as well as the transition from good to poor conformity. In essence, as we increase the curvature of the substrate, either by increasing c or decreasing λ, the conformity of the graphene membrane decreases. This is due to the tradeoff between bending strain and the adhesive forces as discussed before.

Figure 7.9 Plots showing the variation of equilibrium (a) amplitude, a, (b) separation, h and (c,f) adhesion energy, γ with the number of layers, n. The black curves are from our theoretical calculations with different bending rigidities and the red dots are from the simulations. For these simulations, the substrate amplitude and wavelength are fixed at $c = 2$ Å and $\lambda = 24$ Å while $\gamma = 0.3$ J/m².

122

Next, we varied the number of layers from 1 to 5 in the graphene membranes. For these set of simulations we fixed the amplitude and wavelength of the substrate at 2 Å and 24 Å respectively while the same parameters are used for LJ potential. The results are shown in Fig. 7.9. As before, the red dots are from the simulations and each of the two black curves are from our theory with the bending rigidities calculated in two different ways. The dashed curve is obtained using the formula $\kappa_n = nk_1 + Es^3(n^3 - n)/12$ where n is the number of layers, κ_n is the bending rigidity of n layer graphene, E is the Young's modulus and s is the inter-layer separation in multi-layered graphene. This relation is obtained from numerical calculations of spherical graphene using "revised periodic boundary conditions" in density functional tight binding method based simulations.[47] We used a value of 1 eV for κ_1 as before. The solid curve in contrast is obtained by simply assuming $\kappa_n = n\kappa_1$, which meant that each layer in multi-layered membranes behaved independently. As can be seen, we get a better agreement with the simulations with the case where the bending rigidity is assumed to vary linearly. The first approach to calculating the bending rigidity is closer to the straightforward continuum mechanics approach where bending rigidity is simply given by $\kappa = Et^3/12/(1 - \nu^2)$ (t is the thickness); while the second approach suggests frictionless sliding between layers which seems to be the case in the simulations.

It is also to be noticed that we assumed here implicitly that all the layers will have the same amplitude but this is not the case in the simulations. It is observed in the simulations that the amplitude of each layer decreases progressively from the bottom to the top layers, bottom being the closest to the substrate. To illustrate this point, the equilibrium configurations for two and five layered membranes are shown in Fig. 7.10. For the bilayered membrane the amplitudes of the bottom and top layers are 1.62 Å and 1.48 Å respectively; while the same for five layered membrane are 0.65 Å and 0.38 Å. This behavior can easily be explained by the nature of the LJ

potential. The LJ potential energy decreases rapidly as separation is increased from the equilibrium value, hence the bottom most layer interacts in the strongest manner with the substrate. In fact, due to the cutoff distance for LJ interactions in the simulations there is zero interaction between the substrate and any layer or atoms beyond 10.2 Å. Hence the top layers interact appreciably only with their neighboring layers. In addition to this, the low shear modulus of graphene allows the graphene layers to slide and accommodates varying degrees of bending strain. The net effect of these conditions is that the top layers only react to the corrugations of the layer below and so on leading to progressively decreasing amplitudes from the bottom to the top layers or vice versa. This in turn leads to smoother topographies and decreased adhesion energies for multi-layered graphene membranes when compared to monolayer graphene as evidenced in our simulation results.
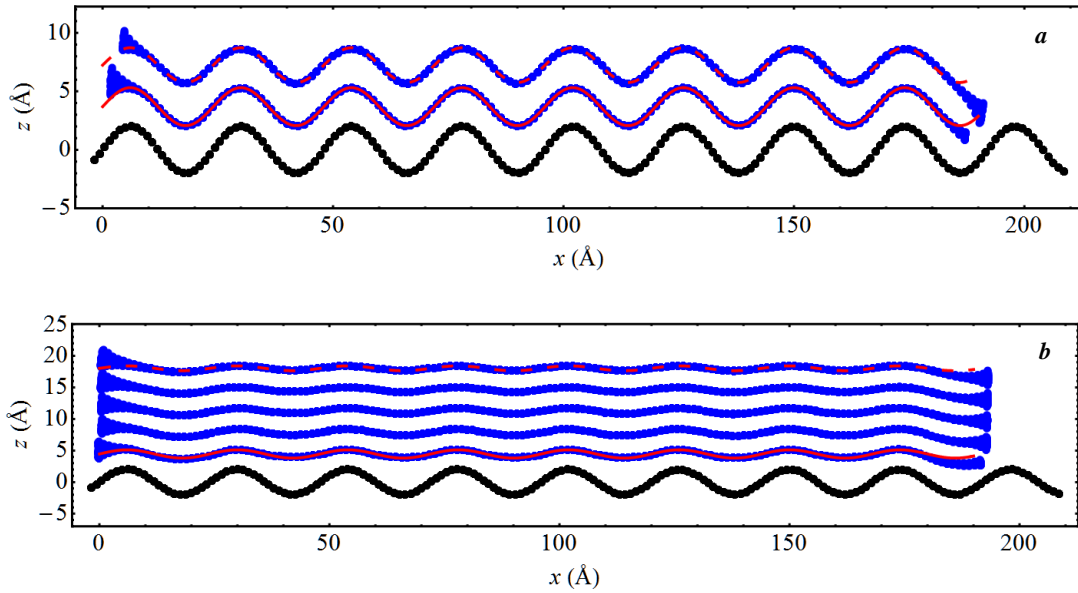
Figure 7.10 Plots showing the equilibrium configuration of (a) bilayer and (b) five layered graphene. The black and blue dots denote substrate and graphene atoms while the red curves denote the best fit sine curves for each layer.

7.2.3 Simulations – 2D Sinusoidal Corrugations

Having performed simulations with corrugations in one direction alone, we directed our attention to corrugations in both x and y directions. The first step of these simulations involved preparation of substrate. This is achieved by moving atoms on a flat surface out of plane according to the equation $s(x, y) = c \, \mathrm{Sin}\left[\frac{2\pi x}{\lambda_x}\right] \mathrm{Sin}\left[\frac{2\pi y}{\lambda_y}\right]$ so that it forms a structure that looks like an egg crate. This structure is allowed to relax as much as possible by constraining the atoms to move only along the surface given by $s(x, y)$. The graphene membrane, which is initially placed 20.4 Å away from the substrate, is then brought closer and allowed to move to an equilibrium configuration through energy minimization while the substrate atoms are rigidly fixed. The initial and the final equilibrium configurations are as shown in Fig. 7.11. The equilibrium configuration of the membrane follows the sinusoidal shape of the substrate and hence can be fit to a sinusoidal surface with the same wavelengths but different amplitude. The same post-processing steps as described before are done to obtain the γ, a and h. For convenience, we chose $\lambda_x = \lambda_y$. As before, we varied the amplitude, c and the wavelength λ of the substrate to see the resultant effect on the graphene membrane conformity. When varying the wavelength, the amplitude is fixed at 1 Å and while varying the amplitude, the wavelength is fixed at 24 Å. All the simulations are carried out at 0 K and with monolayer graphene of size 190×190 Å while the substrate is slightly larger to accommodate vdW interactions of the atoms along the edges of the graphene membrane.
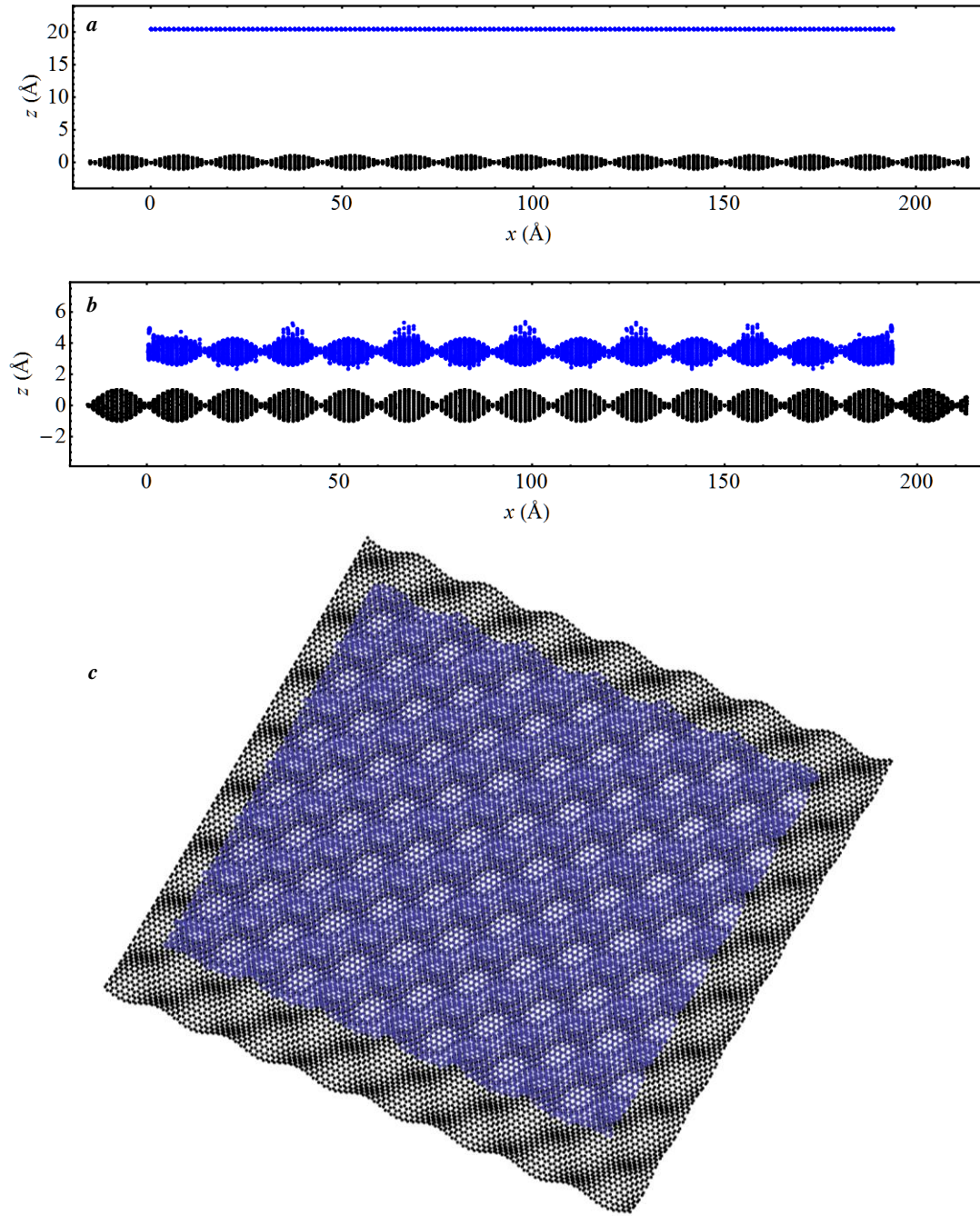
Figure 7.11 Side views of (a) the initial system configuration at the beginning of the simulation, and (b) the equilibrium configuration for graphene obtained at the end of the simulation with a substrate amplitude of 1 Å and wavelength 30 Å. General view of the system equilibrium configuration is seen in (c). The black and blue dots denote the atoms in substrate and graphene respectively.
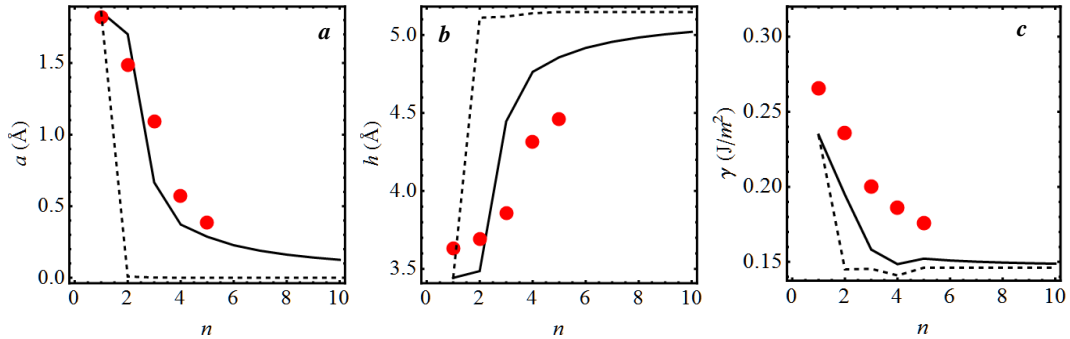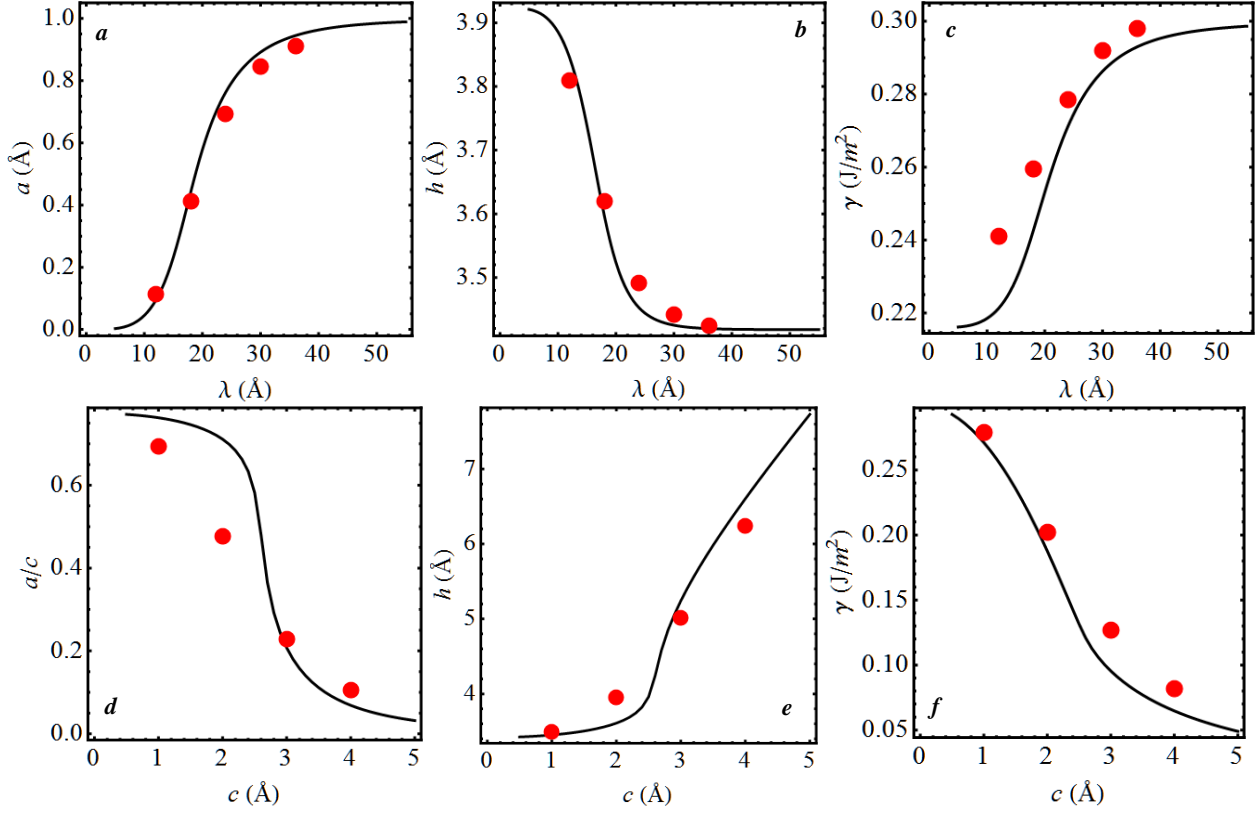
Figure 7.12 Plots showing the variation of (a) Amplitude, a, (b) Mean separation, h, and (c) Adhesion energy, γ with wavelength λ of the corrugated substrate with amplitude fixed at $c = 1$ Å. The bottom row plots show the variation of (d) normalized amplitude, a/c, (e) h and (f) γ with respect to substrate amplitude variation with $\lambda = 24$ Å. The graphene sheet size is set at about 190×190 Å.

The results of the simulations with varying wavelength are shown in Figs. 7.12a, b, and c and those with varying amplitude are shown in Figs. 7.12d, e and f. The red dots in each plot are the results of the simulations while the black curves are obtained from the theory i.e. optimizing the free energy in eq. (7.10). It can be seen that, just as in the case of one dimensional sinusoidal corrugations, the conformity of the graphene membrane transitions from good to poor with increasing substrate amplitude or decreasing wavelength. However, this transition is more gradual compared to the one dimensional case. Also to be noticed is the good agreement between the theory and the simulation results.
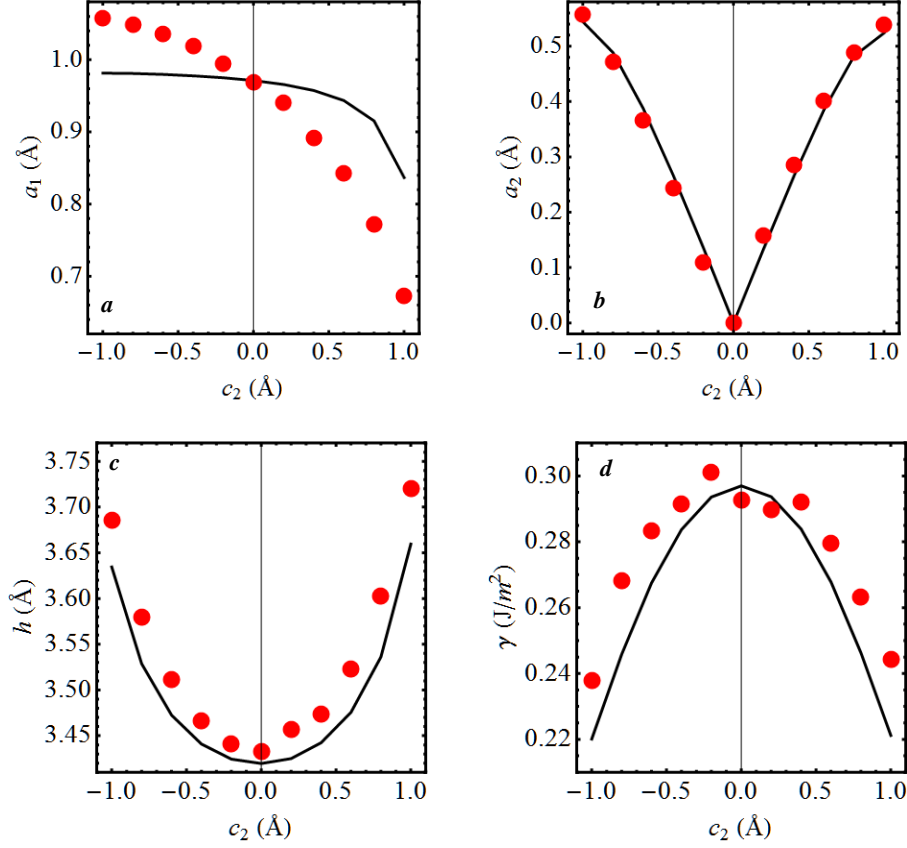
Figure 7.13 Plots in the top row show the variation of the amplitudes of each frequency components in the membrane with respect to the amplitude of the higher frequency component in the substrate: (a) a_1 vs c_2 and (b) a_2 vs c_2. The plots in bottom row show the variation of the equilibrium separation, h and adhesion energy, γ with c_2 respectively. The results from the simulations are plotted as red dots and those from simulations are plotted as black curves.

In the theory sub-section, we discussed a generalized free energy for a substrate described by a full or truncated Fourier series. To retain simplicity, we limited our studies to just two frequency components. We performed simulations with substrates taking the form, $s(x) = c_1 \mathrm{Sin}[qx] + c_2 \mathrm{Cos}[2qx]$ $(q = 2\pi/\lambda)$ where we fixed both c_1 and λ at 1 Å and 24 Å respectively. The simulations setup is exactly same as the one described before with 1D sinusoidal corrugation simulations. The value of c_2 is varied from -1 to 1 Å in steps of 0.2 Å and the results are compared with the theory. The free energy for this particular case is given by:

$$F(a_1, a_2, h) = \frac{D}{2}\left(\frac{q^4 a_1^2}{2} + \frac{(2q)^4 a_2^2}{2}\right) + V_f(h) \tag{7.12}$$

$$+ \sum_{j=1}^{n} \frac{d^j V_f(h)}{dh^j} \sum_{k=0}^{j} \frac{1}{k!\,(j-k)!} (a_1 - c_1)^k (a_2 - c_2)^{j-k} \int_0^{2\pi} Sin[x]^k \, Cos[2x]^{j-k} \frac{dx}{2\pi}$$

This expression is derived from (7.11) where the integrand in the last term is expanded with the help of the binomial theorem. The integrals in the last term here can be evaluated analytically for any arbitrary positive integers j and k. The free energy in this case has only three unknowns – the amplitude of the lower frequency sine component, a_1, the amplitude of the higher frequency cosine component, a_2 and the equilibrium separation, h. These values are obtained via optimization of F as before (here we used $n = 80$). Also these values along with the adhesion energy, γ are obtained from the simulations using the same post-processing steps as before. Figure 7.13 shows the simulation results along with those from the analysis. We plot the variation of a_1, a_2, h and γ with respect to c_2. It can be seen that the analysis captures the general trend quite well and predicts the amplitude of the higher frequency quite well. As the magnitude of c_2 is increased, the overall amplitude of the corrugation is also increased thus decreasing the ability of graphene to conform well. This is reflected quite well in the decrease of adhesion energy and increase of mean separation with increasing magnitude of c_2. However, the amplitude of the lower frequency component, a_1 shows a curious asymmetric trend. It decreases continuously with increasing c_2 and also the analysis does poorly in predicting a_1.

Thus we demonstrated here how our analysis can be extended to multi-component corrugations with a dual component 1D substrate profile. The analysis does well, qualitatively at the least, in predicting the conformity and adhesion energy. We surmise that this method might be used to study adhesion qualitatively on simple substrate profiles like square waves and triangle

waves since such simple substrate profiles can easily be represented using the few dominant Fourier components in their Fourier series expansions. Such surface profiles can also be readily fabricated to carefully understand and engineer adhesion.

7.3 Peel Test with Graphene Ribbons on Flat and Corrugated Substrates
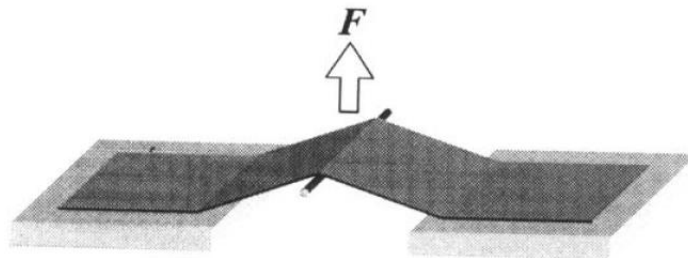
Figure 7.14 Schematic of a V-peel test[107]

We performed V-peel test[57,107] on graphene ribbons adhered to a flat and sinusoidally corrugated substrates (just like the ones described in previous section). The term V-peel test is used by Wan[107] et al in their paper owing to the inverted V-shape assumed by the plate or membrane being peeled as shown in Fig. 7.14. It is a simple experiment used to determine the adhesion energy wherein a line load or a displacement boundary condition is applied at the middle of a membrane and peeled from the substrate while the edges are fixed. The adhesion energy is obtained from the applied force, measured crack length and peel angle. The goal here is to understand the mechanics of peeling of the graphene membranes at the atomistic scale.

The simulation setup is similar to the one shown in Fig. 7.4 except here the periodic boundary condition in the width direction is no longer used. We took advantage of the symmetry of the peel test setup and simulated only half the membrane. Also, in these simulations the adhesion energy is set at about 0.4 J/m^2 by adding an LJ potential with $\epsilon \approx 1$ meV and $\sigma = 3.4$ Å to the interactions between the substrate and graphene atoms in addition to the LJ potential from the AIREBO potential. We will first describe the simulations with flat substrates along with a simple

analysis to explain the simulation results. Then, we move on to the more complicated peeling simulations with corrugated substrates and use the theoretical approach developed in the previous section to develop a theory to describe the results.

7.3.1 Flat Substrates – Theory and Simulations
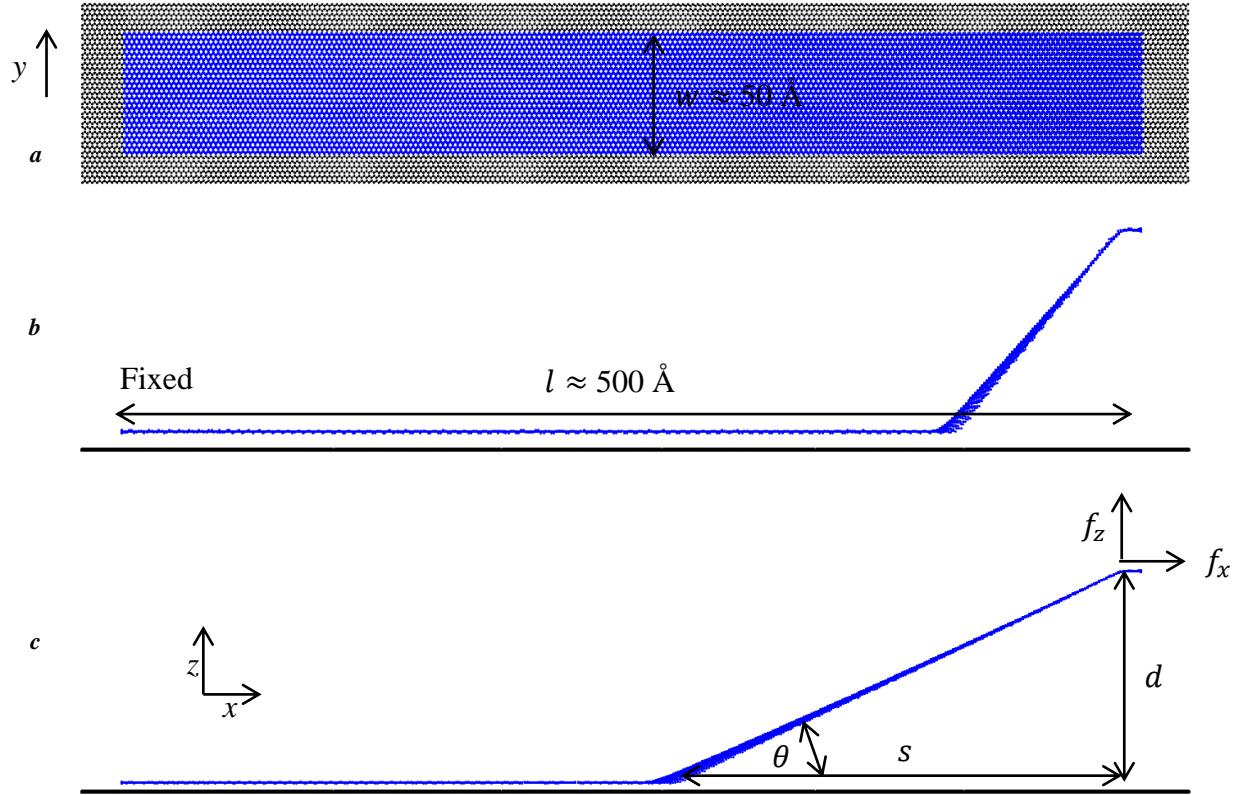
Figure 7.15 (a) Top view of the initial configuration with substrate and graphene atoms in black and blue colors respectively. (b,c) The self-similar equilibrium configurations at two different specified 'd'.

Peel tests at the macro-scale are conventionally performed with flat substrates with different kinds of boundary conditions and linear or non-linear continuum mechanics analyses exist for each case.[57] Non-linearities usually arise from either from large deformations or material models. Here we use one such variant where we apply a displacement boundary condition on one edge, while the other edge is kept fixed. The edge on which the displacement boundary condition is applied is displaced only in the z direction and is held fixed in the x direction. At a given specific

displacement d, the system is allowed to relax to a minimum energy state as shown in Figs. 7.15b,c. This is repeated several times, with an increasing d each instance. As d is increased gradually, the membrane peels away from the substrate forming a "crack" and simultaneously it is stretched. The resultant force on the displaced edge, f and its components, f_x, f_y and f_z are recorded. Also the crack length (s) and peel angle (θ) are extracted from the simulation results. The length of the membrane used is about 500 Å and the width is about 50 Å. The free edge is displaced by 175 Å in steps of 0.1 Å.
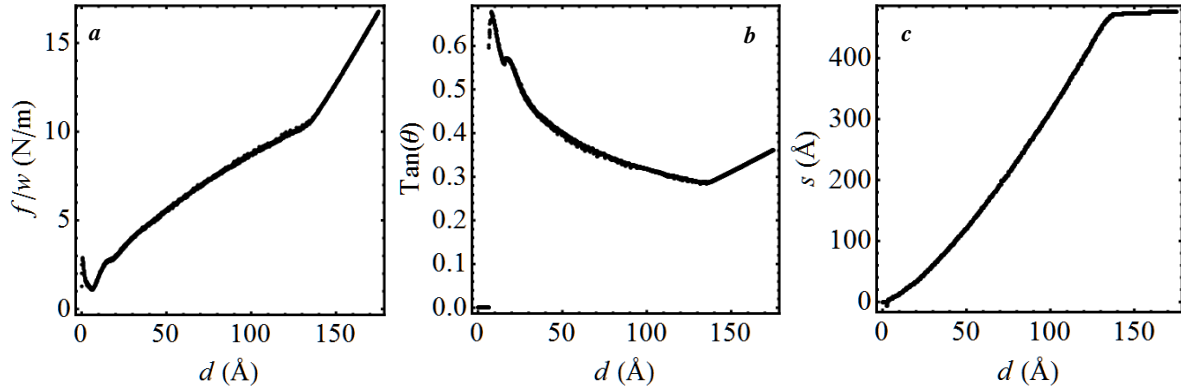
Figure 7.16 (a) Total force per unit width, f/w vs Displacement, d. (b) Angle, $Tan(\theta)$ vs d. (c) Crack length, s vs d.

The results of the simulation are plotted in Figs. 7.16a,b,c. The resultant force, f is plotted in Fig. 7.16a. The force increases gradually, as more length of the membrane is peeled from the substrate (as shown in Fig. 7.16c). At about $d = 137$ Å, the results look different due to the fact that the crack has reached the fixed end as evident from the plot of the crack length (Fig. 7.16c). Here the membrane is only uniaxially stretched and as there is no peeling involved, we are not interested in this part of the results. From continuum theory of the V-peel test,[57] it is known that at equilibrium when the crack is propagating in a self-similar fashion:

$$G = \gamma = \frac{f_z(1 - \text{Cos}[\theta] + \frac{\epsilon}{2})}{w \, \text{Sin}[\theta]} \tag{7.13}$$

Here G is the energy release rate, γ is the adhesion energy, w is the width of the membrane and ϵ is the strain in the delaminated membrane. However when we look at the strain field in the membrane as a function of the x coordinate as obtained from the simulation at $d = 80$ Å (see Fig. 7.17), we notice that the strain in the membrane is almost uniform. This is due to transmission of the membrane stress through the adhered region of the membrane too, in contrast to the normal peel test at macro-scale. This is possible due to the ability of the atoms in the adhered region to slide over the substrate atoms, which is not the case at macro-scale. As a result of this, the strain energy does not contribute to the energy release rate. Putting $\epsilon = 0$, we calculated the energy release rate using the values of f_z and θ and the plot is shown in Fig. 7.18. We can see that the value reaches 0.4 J/m^2 (indicated by red dashed line in Fig. 7.18) at about $d = 10$ Å, before which the eq. (7.13) is not valid as self-similarity is not established yet. It is to be noted that with $\epsilon = 0$, the expression in eq. (7.13) is now equivalent to the energy release rate in peeling of an inextensible membrane.
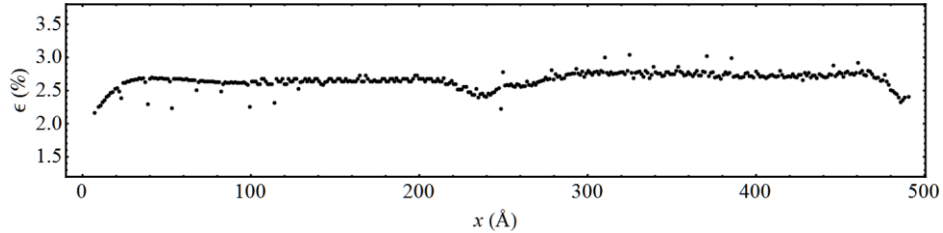
Figure 7.17 Strain field along the x coordinate in the membrane when $d = 80$ Å.
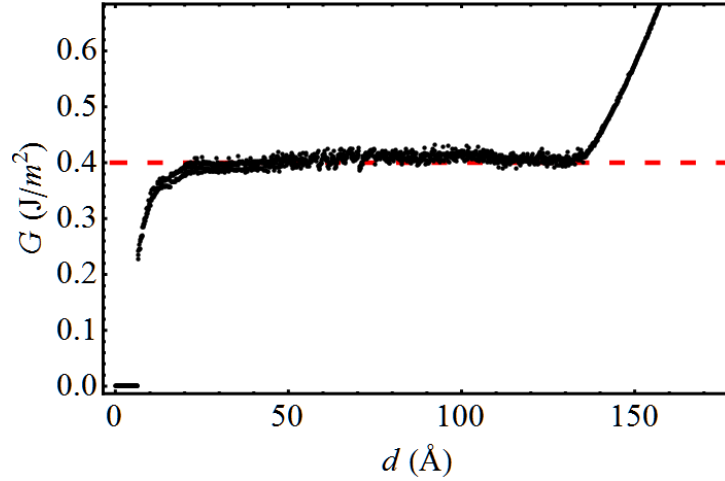
Figure 7.18 Energy release rate calculated using eq. (7.13) putting $\epsilon = 0$.

Hence, in conclusion, we performed peel test simulation with a graphene ribbon on a flat substrate. The simulation results are found to agree well with the peel test analysis of an inextensible membrane. The reason for this is that graphene ribbon as it is peeled from the substrate slides on the substrate which in turn distributes strain energy uniformly across the delaminated and adhered portions of the membrane. This means that as the membrane is peeled, the strain energy does not contribute to the energy released. In spite of the simulation involving atomistic sliding, the continuum mechanics description holds up quite well.

7.3.2   Corrugated Substrates – Theory and Simulations

We now move onto simulations of V-peel tests of graphene ribbons on sinusoidally corrugated substrates. The initial set-up is as shown in Fig. 7.19a: a graphene ribbon on a sinusoidally corrugated substrate with amplitude, c and wavelength, λ. As we learned in the previous sections, graphene will follow the substrate surface profile as closely as possible by achieving a balance between the adhesion energy and bending strain energy. Let the undeformed length of the graphene ribbon be denoted by l and the projected length of the ribbon in its equilibrium configuration be x_0 as shown in Fig. 7.19a. As in the flat substrate case, one edge is

134

fixed and the free edge is displaced vertically (Fig. 7.19b). At any given displacement, the equilibrium configuration is obtained by energy minimization. As shown in Fig. 7.19b, we found that in the equilibrium configuration a portion of the membrane is delaminated while the rest of the membrane still adheres to the substrate. As before, the delamination length, s (or the adhered length, $x = x_0 - s$), the delamination angle, θ, and the peeling force, f are recorded during the simulations. During the course of the simulations, we observed that the graphene atoms slid on the substrate just as in the flat substrate case. This caused the conformity of the graphene membrane in the adhered region change as the free edge is displaced. So, we also recorded how the amplitude of the adhered region, a changes as the displacement is increased.
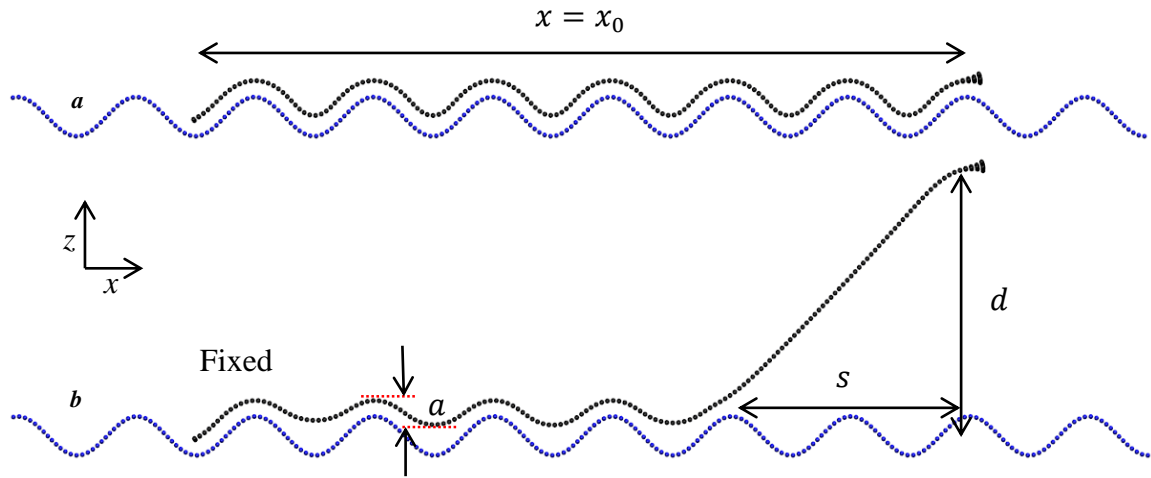
Figure 7.19 V-peel test on corrugated substrates. (a) Initial configuration, (b) Equilibrium configuration at a specific 'd'.

Before presenting the details of the simulation results, let us look at how we can analytically model this problem. The displacement applied at the free edge induces stretching in the whole of the membrane which we assumed to be uniform. We will later verify this assumption using the simulation results. This strain, ϵ can then be calculated from the constraint:

135

$$(l(1 + \epsilon) - l_a(a, x))^2 = (d - a \operatorname{Sin}[qx])^2 + s^2 \tag{7.14}$$

Here, l is the initial undeformed length of the graphene membrane and $l_a(a, x)$ is the arc length of the membrane attached to the substrate which can be easily obtained given the sinusoidal shape assumption. This constraint comes from the fact that the free end of membrane is simply displaced vertically upwards. The resultant force needed to displace the free end can be determined from the strain as, $f = Etw\epsilon$.

Given the known variables substrate amplitude and wavelength (c and λ), displacement (d), the unknowns in this problem are force (f), strain (ϵ), angle (θ), adhered length (x), adhered region amplitude and equilibrium separation (a and h). Assuming $h = h_0$ i.e. fixing the equilibrium separation (h) to be the same as that of a flat substrate (h_0), the only independent variables here are a and x. The rest can be obtained from these two variables: ϵ and hence f from eq. (7.14), θ simply from d and s. Hence, the free energy of the system (graphene ribbon, substrate and the adhesive interface) per unit width can then be written as a function of a and x:

$$F(a, x) = F_{adh} + F_{ben} + F_{str} \tag{7.15}$$

Here, F_{adh} is the contribution of the adhesive interactions. Using the approach as shown in eq. (7.8):

$$F_{adh}(a, x) = V_f(h_0)x + \sum_{i=1}^{n} \frac{d^i V_f(h)}{dh^i} \Big|_{h=h_0} \frac{(a-c)^i}{i!} \int_0^l \operatorname{Sin}[qx]^i \, dx \tag{7.16}$$

$$= -\gamma \left(x - \frac{10}{h_0^2}(a-c)^2 \left(x - \frac{\operatorname{Sin}(2qx)}{2q} \right) + \mathcal{O}((a-c)^3) \right)$$

Unlike in eq. (7.7), as mentioned already, here we fixed the equilibrium separation, h at h_0 to simplify the calculations. Also, the interaction of the atoms near the interface of the adhered and detached regions is ignored here. The bending strain energy contribution, F_{ben} is given by:

$$F_{ben}(a, x) = \frac{D}{2} \int_0^l \left(\frac{d^2 g(x)}{dx^2} \right)^2 dx$$
$$= \frac{D}{4} q^4 a^2 \left(x - \frac{\text{Sin}(2qx)}{2q} \right)$$

(7.17)

Here $g(x) = h_0 + a \, \text{Sin}[qx]$ and any bending strain energy contribution from the region where the membrane goes from adhered to detached is ignored. The strain energy contribution due to stretching induced by the displacement of the free edge, F_{str} is then:

$$F_{str}(a, x) = \frac{Et}{2} \int_0^l \left(\epsilon + \frac{1}{2} \left(\frac{dg(x)}{dx} \right)^2 \right)^2 dx$$
$$= \frac{Et}{2} \left(\begin{array}{c} l\epsilon^2 + \frac{1}{2} \epsilon q^2 a^2 \left(x + \frac{\text{Sin}(2qx)}{2q} \right) \\ + \frac{1}{16} q^4 a^4 \left(\frac{3x}{2} + \frac{\text{Sin}(2qx)}{q} + \frac{\text{Sin}(4qx)}{8q} \right) \end{array} \right)$$

(7.18)

The equilibrium configuration is then given by minimizing the free energy with respect to the unknowns a and x:

$$\frac{\partial F}{\partial a} = \frac{\partial F}{\partial x} = 0$$

(7.19)

Due to the algebraic complexity of the free energy expression, we solved these equations numerically for a given set of parameters. It is to be noticed if the substrate amplitude, c is made zero, then a also goes to zero. This simplifies the free energy to that of membrane adhered to a flat substrate and it can be shown that one can recover the result in eq. (7.13) (see Appendix A.3.5).

137
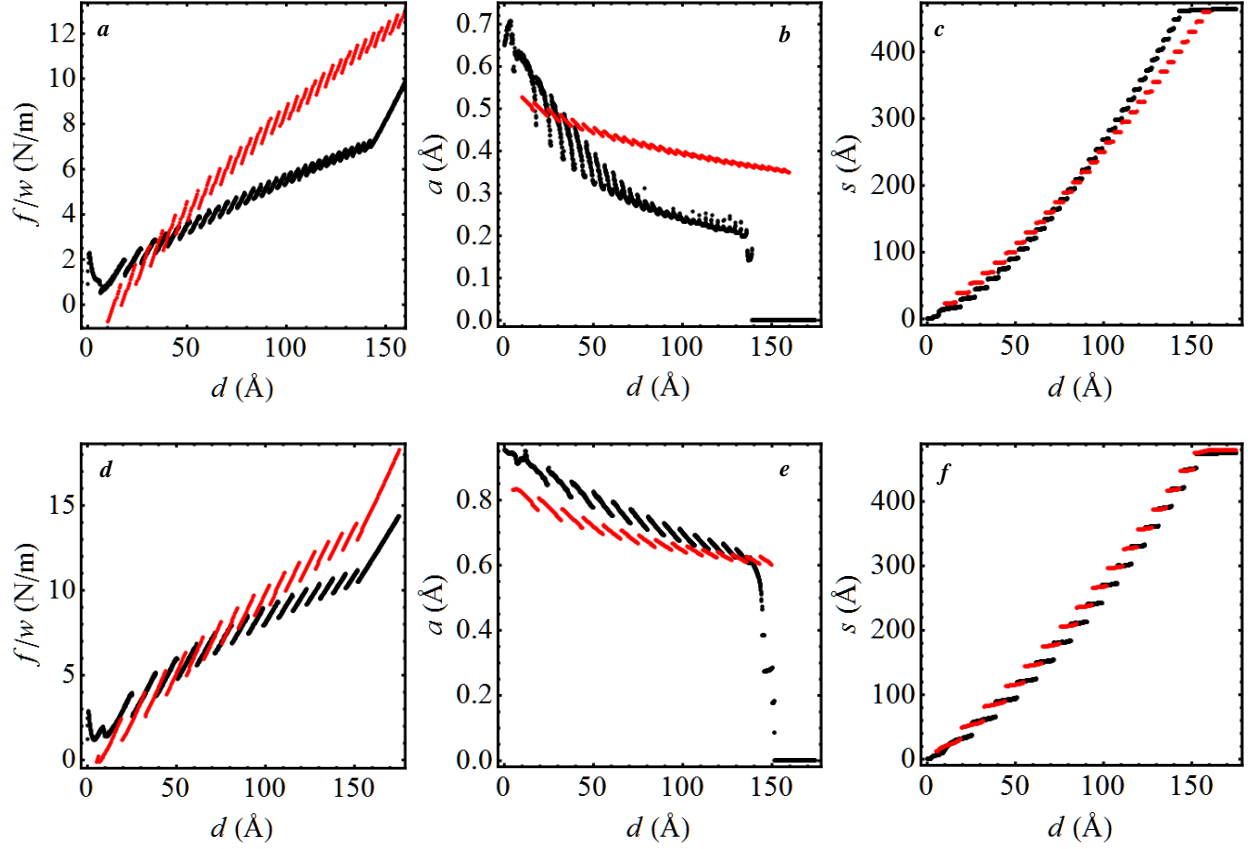
Figure 7.20 (a,d) Force per unit length, (f /w) vs Displacement, d, (b,e) Amplitude, a vs d and (c,f) Crack length, s vs d for λ = 15 Å and 30 Å respectively. The data in black and red are from the simulations and theory respectively.

We now compare the results of the simulations with those from our analysis. Because we assumed that the equilibrium separation does not change from the flat substrate case, we limited our simulations to substrate amplitude of $c = 1$ Å where $h \approx h_0$. The results from the simulations along with results of our analysis are plotted in Fig. 7.20 with $\lambda = 15$ Å and $\lambda = 30$ Å. It can be noticed that the overall mechanics is discontinuous due to 'instabilities'. We learned from the simulations that these 'instabilities' are formed due to combined sliding and delamination of the graphene ribbon from the substrate. As the free edge displacement, d is increased initially the membrane just slides resulting in a decrease of the amplitude of the adhered region, a without any change in x, the length of the adhered region. Also, we noticed that while sliding, the membrane is pinned to a peak on the substrate. As d is increased further, the membrane 'snaps' by getting

138

detached by a magnitude equal to about half the wavelength, λ. This snap seems to create slack which gets redistributed into the adhered region increasing the amplitude, a though not back to the initial value. After this snap-off, we noticed that the membrane is pinned at the next available peak on the substrate and now starts to slide again upon increasing d. This behavior continues on until the fixed end is reached. The pinning of the membrane at a peak is evident from the nearly discrete increment of the delaminated length as shown in Fig. 7.20c,f.

If not for the undulating behavior in the overall mechanics as shown in Fig. 7.20, it is similar to that of peeling from the flat substrate shown in Fig. 7.16. The force required to delaminate and displace the free end, f increases with increasing displacement, d (Figs. 7.20a,d). The delaminated length, s (or equivalently adhered length, x) also increases with d (Figs. 7.20c,f). On the other hand, the amplitude of the graphene ribbon in the adhered region, a decreases gradually with increasing d (Figs. 7.20b,e). The results from our analysis do poorly with $\lambda = 15$ Å case and better with $\lambda = 30$ Å when compared to simulation results. The reason might be the assumption $h = h_0$. Also, it is known graphene exhibits non-linear material properties beyond 1% strain[103] which we definitely surpass in these simulations. In contrast, in our analysis we assumed a constant value Et. In spite of its inaccuracy, our analysis captures the nature of the mechanics involved in this problem quite well.

We asserted earlier that the strain in the membrane is uniform while developing our theoretical analysis. The strain fields at a displacement of $d = 75$ Å are plotted in Figs. 7.21a and 7.21b for $\lambda = 15$ Å and 30 Å cases respectively. We can clearly see that the strains are quite uniform, hence validating our assertion.
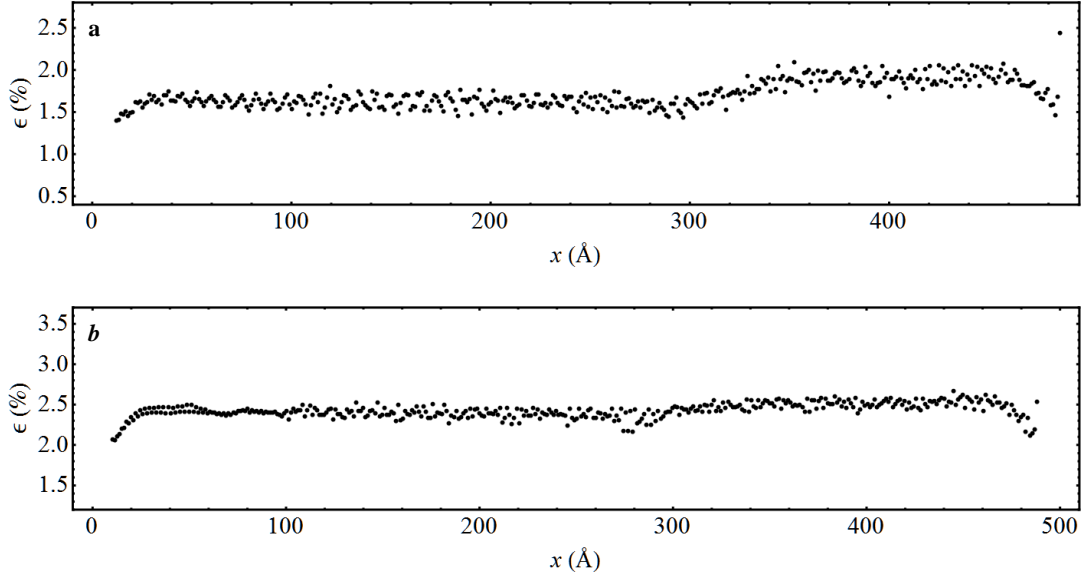
Figure 7.21 Strain field for (a) λ= 15 Å case, (b) λ = 30 Å case with d = 75 Å
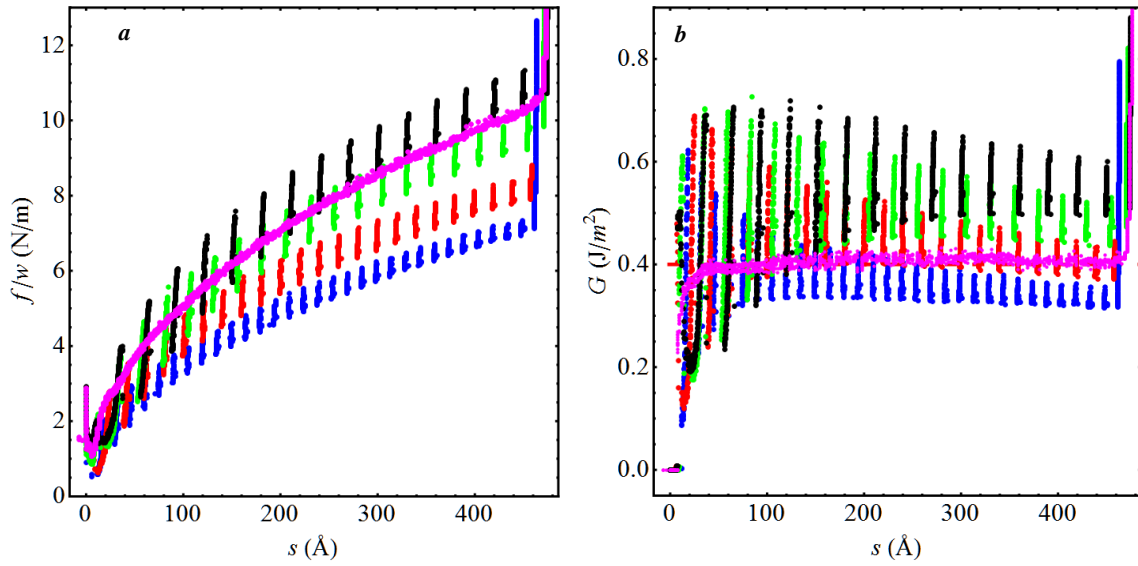
Figure 7.22 (a) The total force per unit width, f/w and (b) the energy release rate, G according to eq. (7.13) plotted against the crack length, s for λ = 15 Å (blue), λ = 20 Å (red), λ = 25 Å (green), λ = 30 Å (black) and flat substrate (magenta).

In an actual experiment, the force-displacement curve is the information that one can obtain in the easiest manner. We plotted a comparison of the magnitude of the force per unit width with respect to the crack length in Fig. 7.22a with different wavelengths along with the limiting case of a flat substrate. Expectedly we see that larger the wavelength, the closer the force-displacement to

140

the flat substrate case. Notice that from the periodic nature of these plots, we can easily infer the number of peaks on the substrate and the wavelength. In Fig. 7.22b, we plotted the energy release rate using the expression that we used for a flat substrate in eq. (7.13). The energy release rates for corrugated substrate give undulating values not revealing any direct information about the true adhesion energy as in the flat substrate case. These results are similar to the case of a flat substrate with periodically varying adhesion energy.[108] However, in our case the amplitude of the periodic variation is coupled to the amplitude of the graphene membrane (see eq. (7.16)) which in turn depends on the strain in the system in a non-linear manner (see eq. (7.14)). Thus even as the energy release rate shows a periodic pattern, the amplitude varies in a non-linear intractable manner making it very difficult to extract the adhesion energy from the energy release rate plots.

7.4 Summary

This chapter is divided into two main sections. In the first section, we described molecular mechanics simulations and a companion theoretical analysis where the equilibrium configurations of graphene membranes on sinusoidally corrugated substrates. We learnt through these simulations that the adhesion energy depends on the amplitude and wavelength of the substrate corrugations with larger amplitudes and smaller wavelengths leading to poor conformity. We confirmed a snap-through phenomenon associated with the conformity of graphene that has been observed by several others in the literature. We showed that our analysis compares quite well with the simulation results with both one and two dimensional sinusoidal corrugations.

In the second section, the peel mechanics of graphene ribbons on flat as well as sinusoidally corrugated substrates is studied. We found that the mechanics of peeling of the ribbon on a flat substrate is similar to that of an inextensible membrane owing to the sliding of the graphene sheet on the substrate. The mechanics of peeling on corrugated substrates differs significantly from that

on the flat substrate and reveals interesting mechanics. In the latter case, we observed instabilities in the way the graphene membrane delaminates from the substrate. We attempted to explain the observed results with the help of a free energy based analysis. This analysis, if not very accurate, captures the essential nature of the mechanics involved.

Bibliography

1. Novoselov, K. S. *et al.* Electric field effect in atomically thin carbon films. *Science* **306,** 666–9 (2004).

2. Hernandez, Y. *et al.* High-yield production of graphene by liquid-phase exfoliation of graphite. *Nature nanotechnology* **3,** 563–8 (2008).

3. Liang, X. *et al.* Electrostatic force assisted exfoliation of prepatterned few-layer graphenes into device sites. *Nano letters* **9,** 467–72 (2009).

4. Berger, C. *et al.* Ultrathin Epitaxial Graphite: 2D Electron Gas Properties and a Route toward Graphene-based Nanoelectronics. *The Journal of Physical Chemistry B* **108,** 19912–19916 (2004).

5. Berger, C. *et al.* Electronic confinement and coherence in patterned epitaxial graphene. *Science* **312,** 1191–6 (2006).

6. Coraux, J., N'Diaye, A. T., Busse, C. & Michely, T. Structural coherency of graphene on Ir(111). *Nano letters* **8,** 565–70 (2008).

7. Sutter, P. W., Flege, J.-I. & Sutter, E. A. Epitaxial graphene on ruthenium. *Nature materials* **7,** 406–11 (2008).

8. Kim, K. S. K. S. *et al.* Large-scale pattern growth of graphene films for stretchable transparent electrodes. *Nature* **457,** 706–10 (2009).

9. Reina, A. *et al.* Large area, few-layer graphene films on arbitrary substrates by chemical vapor deposition. *Nano letters* **9,** 30–5 (2009).

10. Li, X. *et al.* Large-area synthesis of high-quality and uniform graphene films on copper foils. *Science* **324,** 1312–4 (2009).

11. Sutter, P., Sadowski, J. T. & Sutter, E. Graphene on Pt(111): Growth and substrate interaction. *Physical Review B* **80,** 245411 (2009).

12. Kwon, S.-Y. *et al.* Growth of semiconducting graphene on palladium. *Nano letters* **9,** 3985–90 (2009).

13. Yan, Z., Peng, Z. & Tour, J. M. Chemical vapor deposition of graphene single crystals. *Accounts of chemical research* **47,** 1327–37 (2014).

14. Lee, J.-H. *et al.* Wafer-Scale Growth of Single-Crystal Monolayer Graphene on Reusable Hydrogen-Terminated Germanium. *Science* **344,** 286–289 (2014).

15.	Wu, B. *et al.* Self-organized graphene crystal patterns. *NPG Asia Materials* **5,** e36 (2013).

16.	Kim, K. *et al.* Grain boundary mapping in polycrystalline graphene. *ACS nano* **5,** 2142–6 (2011).

17.	Suk, J. W. *et al.* Transfer of CVD-grown monolayer graphene onto arbitrary substrates. *ACS nano* **5,** 6916–24 (2011).

18.	Blake, P. *et al.* Making graphene visible. *Applied Physics Letters* **91,** 063124 (2007).

19.	Lee, C., Wei, X., Kysar, J. W. & Hone, J. Measurement of the elastic properties and intrinsic strength of monolayer graphene. *Science* **321,** 385–8 (2008).

20.	Geim, A. K. Graphene: status and prospects. *Science* **324,** 1530–4 (2009).

21.	Lau, C. N., Bao, W. & Velasco, J. Properties of suspended graphene membranes. *Materials Today* **15,** 238–245 (2012).

22.	Bunch, J. S. *et al.* Impermeable atomic membranes from graphene sheets. *Nano letters* **8,** 2458–62 (2008).

23.	Weiss, N. O. *et al.* Graphene: an emerging electronic material. *Advanced materials (Deerfield Beach, Fla.)* **24,** 5782–825 (2012).

24.	Choi, W., Lahiri, I., Seelaboyina, R. & Kang, Y. S. Synthesis of Graphene and Its Applications: A Review. *Critical Reviews in Solid State and Materials Sciences* **35,** 52–71 (2010).

25.	Wassei, J. K. & Kaner, R. B. Graphene, a promising transparent conductor. *Materials Today* **13,** 52–59 (2010).

26.	Schedin, F. *et al.* Detection of individual gas molecules adsorbed on graphene. *Nature materials* **6,** 652–5 (2007).

27.	Milaninia, K. M., Baldo, M. a., Reina, A. & Kong, J. All graphene electromechanical switch fabricated by chemical vapor deposition. *Applied Physics Letters* **95,** 183105 (2009).

28.	Liu, X. *et al.* Large arrays and properties of 3-terminal graphene nanoelectromechanical switches. *Advanced materials (Deerfield Beach, Fla.)* **26,** 1571–6 (2014).

29.	Bunch, J. S. *et al.* Electromechanical resonators from graphene sheets. *Science* **315,** 490–3 (2007).

30.	Chen, C. *et al.* Performance of monolayer graphene nanomechanical resonators with electrical readout. *Nature nanotechnology* **4,** 861–7 (2009).

31. Jiang, D., Cooper, V. R. & Dai, S. Porous graphene as the ultimate membrane for gas separation. *Nano letters* **9,** 4019–4024 (2009).

32. Koenig, S. P., Wang, L., Pellegrino, J. & Bunch, J. S. Selective molecular sieving through porous graphene. *Nature nanotechnology* **7,** 728–32 (2012).

33. Cohen-Tanugi, D. & Grossman, J. C. Water desalination across nanoporous graphene. *Nano letters* **12,** 3602–8 (2012).

34. Autumn, K. *et al.* Evidence for van der Waals adhesion in gecko setae. *Proceedings of the National Academy of Sciences of the United States of America* **99,** 12252–6 (2002).

35. Maboudian, R. Critical Review: Adhesion in surface micromechanical structures. *Journal of Vacuum Science & Technology B: Microelectronics and Nanometer Structures* **15,** 1 (1997).

36. Scharfenberg, S. *et al.* Probing the mechanical properties of graphene using a corrugated elastic substrate. *Applied Physics Letters* **98,** 091908 (2011).

37. Low, T., Perebeinos, V., Tersoff, J. & Avouris, P. Deformation and Scattering in Graphene over Substrate Steps. *Physical Review Letters* **108,** 096601 (2012).

38. Seol, J. H. *et al.* Two-dimensional phonon transport in supported graphene. *Science* **328,** 213–6 (2010).

39. Pereira, V. & Castro Neto, A. Strain Engineering of Graphene's Electronic Structure. *Physical Review Letters* **103,** 046801 (2009).

40. Van Lier, G., Van Alsenoy, C., Van Doren, V. & Geerlings, P. Ab initio study of the elastic properties of single-walled carbon nanotubes and graphene. *Chemical Physics Letters* **326,** 181–185 (2000).

41. Kudin, K., Scuseria, G. & Yakobson, B. C2F, BN, and C nanoshell elasticity from ab initio computations. *Physical Review B* **64,** 235406 (2001).

42. Frank, I. W., Tanenbaum, D. M., van der Zande, A. M. & McEuen, P. L. Mechanical properties of suspended graphene sheets. *Journal of Vacuum Science & Technology B: Microelectronics and Nanometer Structures* **25,** 2558 (2007).

43. Yakobson, B., Brabec, C., Bernholc, J. & Berhnolc, J. Nanomechanics of Carbon Tubes: Instabilities beyond Linear Response. *Physical Review Letters* **76,** 2511–2514 (1996).

44. Lu, J. Elastic Properties of Carbon Nanotubes and Nanoropes. *Physical Review Letters* **79,** 1297–1300 (1997).

45. Huang, Y., Wu, J. & Hwang, K. Thickness of graphene and single-wall carbon nanotubes. *Physical Review B* **74,** 245413 (2006).

46. Arroyo, M. & Belytschko, T. Finite crystal elasticity of carbon nanotubes based on the exponential Cauchy-Born rule. *Physical Review B* **69,** 115415 (2004).

47. Koskinen, P. & Kit, O. Approximate modeling of spherical membranes. *Physical Review B* **82,** (2010).

48. Wei, Y., Wang, B., Wu, J., Yang, R. & Dunn, M. L. Bending rigidity and Gaussian bending stiffness of single-layered graphene. *Nano letters* **13,** 26–30 (2013).

49. Nicklow, R., Wakabayashi, N. & Smith, H. Lattice Dynamics of Pyrolytic Graphite. *Physical Review B* **5,** 4951–4962 (1972).

50. Lindahl, N. *et al.* Determination of the bending rigidity of graphene via electrostatic actuation of buckled membranes. *Nano letters* **12,** 3526–31 (2012).

51. Timoshenko, S. & Woinowsky-Krieger, S. *Theory of Plates and Shells*. (McGraw-Hill, 1959).

52. Plaut, R. H. Linearly elastic annular and circular membranes under radial, transverse, and torsional loading. Part I: large unwrinkled axisymmetric deformations. *Acta Mechanica* **202,** 79–99 (2008).

53. Hencky, H. Über den spannungszustand in kreisrunden platten mit verschwindender biegungssteiflgkeit. *Zeitschrift für Mathematik und Physik* **63,** 311–317 (1915).

54. Campbell, J. D. On the theory of initially tensioned circular membranes subjected to uniform pressure. *The Quarterly Journal of Mechanics and Applied Mathematics* **9,** 84–93 (1956).

55. Fichter, W. B. Some Solutions for the Large Deflections of Uniformly Loaded Circular Membranes. *NASA Technical Paper* **3658,** (1997).

56. Grabmüller, H. & Weinitschke, H. J. Finite displacements of annular elastic membranes. *Journal of Elasticity* **16,** 135–147 (1986).

57. Williams, J. G. Energy Release Rates for the Peeling of Flexible Membranes and the Analysis of Blister Tests. *International Journal of Fracture* **87,** 265–288 (1997).

58. Saif, M. T. A., Alaca, B. E. & Sehitoglu, H. Analytical modeling of electrostatic membrane actuator for micro pumps. *Journal of Microelectromechanical Systems* **8,** 335–345 (1999).

59. Xu, X. & Liao, K. Molecular and continuum mechanics modeling of graphene deformation. *Materials Physics and Mechanics* **4,** 148–151 (2001).

60. Kitipornchai, S., He, X. & Liew, K. Continuum model for the vibration of multilayered graphene sheets. *Physical Review B* **72,** 1–6 (2005).

61. Atalaya, J., Isacsson, A. & Kinaret, J. M. Continuum elastic modeling of graphene resonators. *Nano letters* **8,** 4196–200 (2008).

62. Duan, W. H. & Wang, C. M. Nonlinear bending and stretching of a circular graphene sheet under a central point load. *Nanotechnology* **20,** 075702 (2009).

63. Bao, W. *et al.* Controlled ripple texturing of suspended graphene and ultrathin graphite membranes. *Nature nanotechnology* **4,** 562–6 (2009).

64. Lipowsky, R. The conformation of membranes. *Nature* **349,** 475–81 (1991).

65. Swain, P. S. & Andelman, D. The Influence of Substrate Structure on Membrane Adhesion. *Langmuir* **15,** 8902–8914 (1999).

66. Pierre-Louis, O. Adhesion of membranes and filaments on rippled surfaces. *Physical Review E* **78,** 021603 (2008).

67. Israelachvili, J. N. & Tabor, D. The Measurement of Van Der Waals Dispersion Forces in the Range 1.5 to 130 nm. *Proceedings of the Royal Society A: Mathematical, Physical and Engineering Sciences* **331,** 19–38 (1972).

68. Israelachvili, J. *et al.* Recent advances in the surface forces apparatus (SFA) technique. *Reports on Progress in Physics* **73,** 036601 (2010).

69. Lu, Z. & Dunn, M. L. van der Waals adhesion of graphene membranes. *Journal of Applied Physics* **107,** 044301 (2010).

70. Bertoni, G., Calmels, L., Altibelli, A. & Serin, V. First-principles calculation of the electronic structure and EELS spectra at the graphene/Ni(111) interface. *Physical Review B* **71,** 075402 (2005).

71. Jiang, D., Du, M.-H. & Dai, S. First principles study of the graphene/Ru(0001) interface. *The Journal of chemical physics* **130,** 074705 (2009).

72. Rudenko, A. N., Keil, F. J., Katsnelson, M. I. & Lichtenstein, A. I. Graphene adhesion on mica: Role of surface morphology. *Physical Review B* **83,** 045409 (2011).

73. Zong, Z., Chen, C.-L., Dokmeci, M. R. & Wan, K. Direct measurement of graphene adhesion on silicon surface by intercalation of nanoparticles. *Journal of Applied Physics* **107,** 026104 (2010).

74. Small, M. K. & Nix, W. D. Analysis of the accuracy of the bulge test in determining the mechanical properties of thin films. *Journal of Materials Research* **7,** 1553–1563 (2011).

75. Dannenberg, H. Measurement of adhesion by a blister method. *Journal of Applied Polymer Science* **5,** 125–134 (1961).

76. Gent, A. N. & Lewandowski, L. H. Blow-off pressures for adhering layers. *Journal of Applied Polymer Science* **33,** 1567–1577 (1987).

77. Wan, K.-T. & Mai, Y.-W. Fracture mechanics of a new blister test with stable crack growth. *Acta Metallurgica et Materialia* **43,** 4109–4115 (1995).

78. Wang, L. *et al.* Ultrathin oxide films by atomic layer deposition on graphene. *Nano letters* **12,** 3706–10 (2012).

79. Barton, R. A. *et al.* High, size-dependent quality factor in an array of graphene mechanical resonators. *Nano letters* **11,** 1232–6 (2011).

80. Allen, M. G. & Senturia, S. D. Analysis of Critical Debonding Pressures of Stressed Thin Films in the Blister Test. *The Journal of Adhesion* **25,** 303–315 (1988).

81. Allen, M. G. & Senturia, S. D. Application of the Island Blister Test for Thin Film Adhesion Measurement. *The Journal of Adhesion* **29,** 219–231 (1989).

82. Zhang, Z. & Li, T. Determining graphene adhesion via substrate-regulated morphology of graphene. *Journal of Physics D: Applied Physics* **43,** 075303 (2010).

83. Gao, W. & Huang, R. Effect of surface roughness on adhesion of graphene membranes. *Journal of Physics D: Applied Physics* **44,** 452001 (2011).

84. Viola Kusminskiy, S., Campbell, D. K., Castro Neto, A. H. & Guinea, F. Pinning of a two-dimensional membrane on top of a patterned substrate: The case of graphene. *Physical Review B* **83,** 165405 (2011).

85. Kitt, A. L. *et al.* How graphene slides: measurement and theory of strain-dependent frictional forces between graphene and SiO2. *Nano letters* **13,** 2605–10 (2013).

86. Mohideen, U. & Roy, A. Precision Measurement of the Casimir Force from 0.1 to 0.9 μm. *Physical Review Letters* **81,** 4549–4552 (1998).

87. Bordag, M., Geyer, B., Klimchitskaya, G. L. & Mostepanenko, V. M. Lifshitz-type formulas for graphene and single-wall carbon nanotubes: van der Waals and Casimir interactions. *Physical Review B* **74,** 205431 (2006).

88. Sarabadani, J., Naji, A., Asgari, R. & Podgornik, R. Many-body effects in the van der Waals–Casimir interaction between graphene layers. *Physical Review B* **84,** 155407 (2011).

89. Casimir, H. B. G. On the attraction between two perfectly conducting plates. *Proc. K. Ned. Akad. Wet.* **51,** 150 (1948).

90. Hlyoon. High-resolution Atomic Imaging of Specimens in Liquid Observed by Transmission Electron Microscopes Using Graphene Liquid Cells. *KAIST* (2012). at <http://www.kaist.edu/_prog/_board/?mode=V&no=10304&code=ed_news&site_dvs_cd=en&menu_dvs_cd=0601&list_typ=B&skey=&sval=&smonth=&site_dvs=&GotoPage=18>

91. Levy, N. *et al.* Strain-induced pseudo-magnetic fields greater than 300 tesla in graphene nanobubbles. *Science* **329,** 544–7 (2010).

92. Georgiou, T. *et al.* Graphene bubbles with controllable curvature. *Applied Physics Letters* **99,** 093103 (2011).

93. Yuk, J. M. *et al.* High-resolution EM of colloidal nanocrystal growth using graphene liquid cells. *Science* **336,** 61–4 (2012).

94. Lim, C. H. Y. X. *et al.* A hydrothermal anvil made of graphene nanobubbles on diamond. *Nature communications* **4,** 1556 (2013).

95. Simulia, D. ABAQUS 6.11 Analysis User's Manual. *Abaqus 6.11 Documentation* (2011).

96. Lui, C. H., Liu, L., Mak, K. F., Flynn, G. W. & Heinz, T. F. Ultraflat graphene. *Nature* **462,** 339–41 (2009).

97. Guinea, F., Horovitz, B. & Le Doussal, P. Gauge field induced by ripples in graphene. *Physical Review B* **77,** 205421 (2008).

98. Guinea, F., Katsnelson, M. I. & Geim, A. K. Energy gaps and a zero-field quantum Hall effect in graphene by strain engineering. *Nature Physics* **6,** 30–33 (2009).

99. Lipowsky, R. & Seifert, U. Adhesion of membranes: a theoretical perspective. *Langmuir* **7,** 1867–1873 (1991).

100. Aitken, Z. H. & Huang, R. Effects of mismatch strain and substrate surface corrugation on morphology of supported monolayer graphene. *Journal of Applied Physics* **107,** 123531 (2010).

101. Scharfenberg, S., Mansukhani, N., Chialvo, C., Weaver, R. L. & Mason, N. Observation of a snap-through instability in graphene. *Applied Physics Letters* **100,** 021910 (2012).

102. Shenoy, V., Reddy, C., Ramasubramaniam, A. & Zhang, Y. Edge-Stress-Induced Warping of Graphene Sheets and Nanoribbons. *Physical Review Letters* **101,** 245501 (2008).

103. Zhao, H., Min, K. & Aluru, N. R. Size and chirality dependent elastic properties of graphene nanoribbons under uniaxial tension. *Nano letters* **9,** 3012–5 (2009).

104. Xu, Z. & Buehler, M. J. Geometry controls conformation of graphene sheets: membranes, ribbons, and scrolls. *ACS nano* **4,** 3869–76 (2010).

105. Stuart, S. J., Tutein, A. B. & Harrison, J. A. A reactive potential for hydrocarbons with intermolecular interactions. *The Journal of Chemical Physics* **112,** 6472 (2000).

106. Plimpton, S. Fast Parallel Algorithms for Short-Range Molecular Dynamics. *Journal of Computational Physics* **117,** 1–19 (1995).

107. Wan, K.-T. Fracture Mechanics of a V-peel Adhesion Test – Transition from a Bending Plate to a Stretching Membrane. *The Journal of Adhesion* **70,** 197–207 (1999).

108. Chen, B., Shi, X. & Gao, H. Apparent fracture/adhesion energy of interfaces with periodic cohesive interactions. *Proceedings of the Royal Society A: Mathematical, Physical and Engineering Sciences* **464,** 657–671 (2008).

109. Koh, Y. K., Bae, M.-H., Cahill, D. G. & Pop, E. Reliably counting atomic planes of few-layer graphene (n > 4). *ACS nano* **5,** 269–74 (2011).

110. Cheo, L. S. & Reiss, E. L. Unsymmetric Wrinkling of Circular Plates. *Quarterly of Applied Mathematics* **31,** 75–91 (1973).

Appendix A

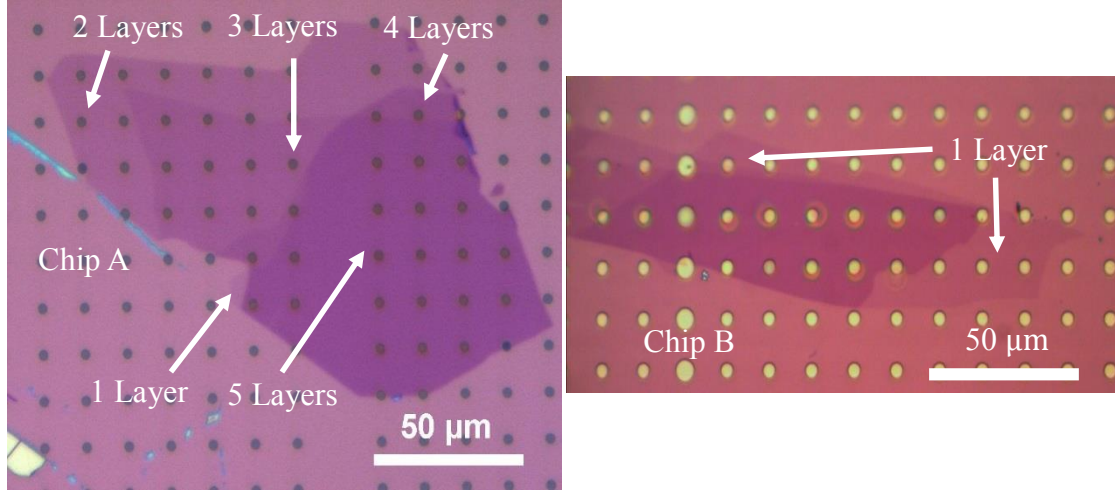## A.1 Appendix for Chapter 3

Figure A.1 Optical images of graphene flakes on Chips A & B with the number of layers identified.
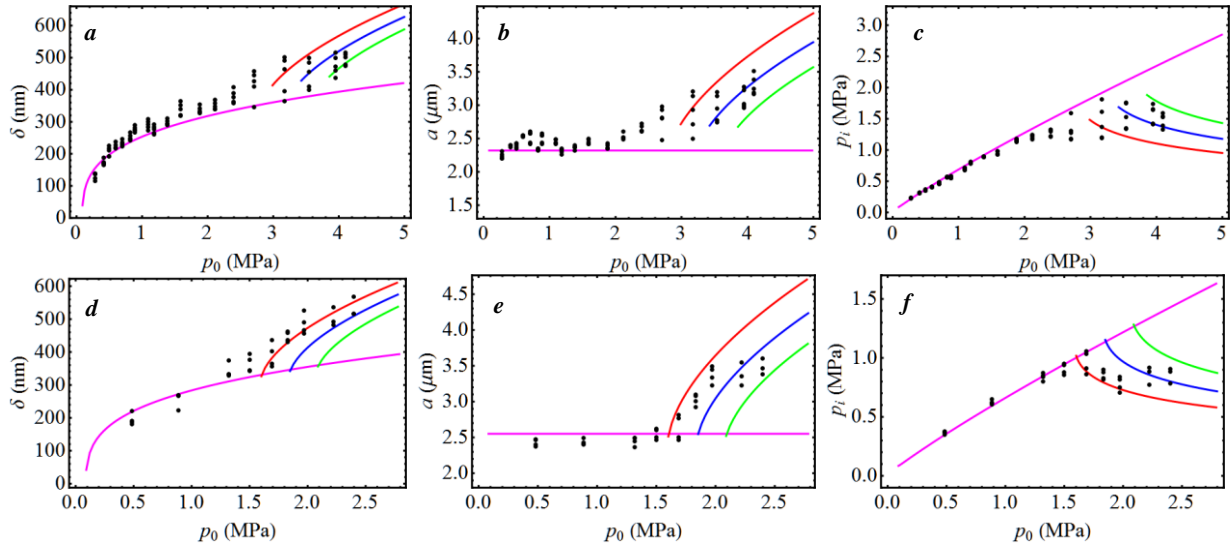

Figure A.2 Plots showing maximum deflection δ (a,d), blister radius a (b,e) and final equilibrium pressure p_i (c,f) versus input pressure p_0 for all monolayer membranes on chips B (a-c) and C (d-f) respectively. The magenta colored curve is a theoretical curve assuming no delamination of the membrane for $Et = 347\,N/m$. Red, Blue and green curves are theoretical curves for three different values of the graphene/SiO_2 adhesion energy Γ – 0.38, 0.45, 0.52 J/m^2 and 0.20, 0.24, 0.28 J/m^2 for chips B and C respectively.
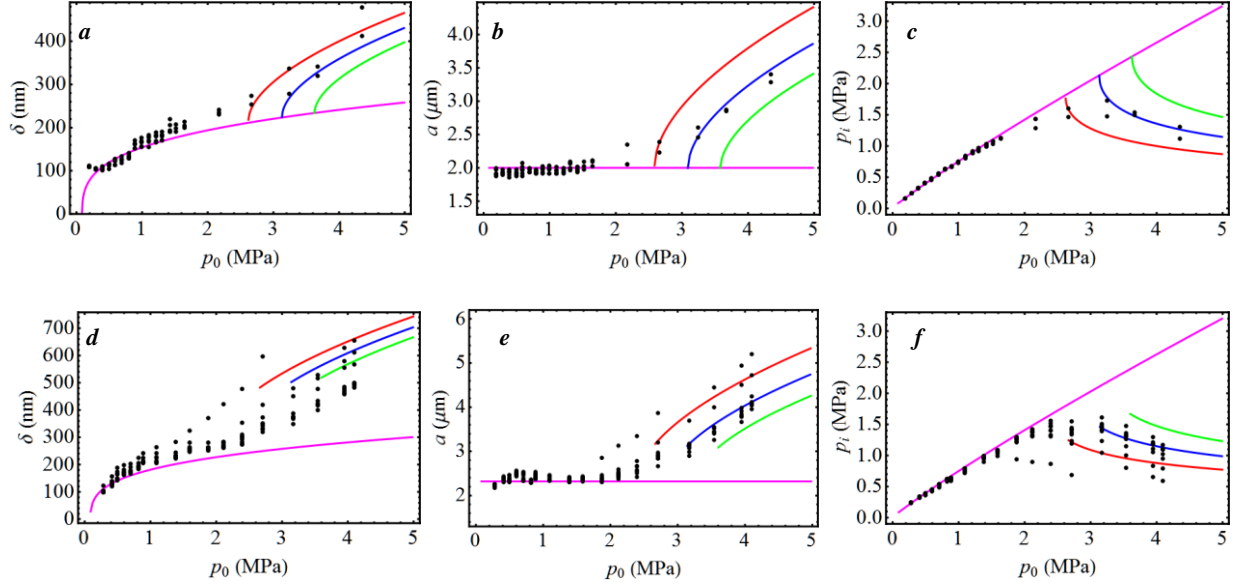
Figure A.3 Plots showing maximum deflection δ (a,d), blister radius a (b,e) and final equilibrium pressure p_i (c, f) versus input pressure p_0 for three-layer membranes on chips A and B respectively. The magenta colored curve is a theoretical curve assuming no delamination of the membrane for $Et = 950$ N/m. Red, Blue and green curves are theoretical curves for three different values of the graphene/SiO₂ adhesion energy $\Gamma - 0.24, 0.30, 0.36$ J/m² and 0.26, 0.32, 0.38 J/m² for chips A and B respectively.

Figure A.4 Plots showing maximum deflection δ (a), blister radius a (b) and final equilibrium pressure p_i (c) versus input pressure p_0 for all four-layer membranes on Chip A. The magenta colored curve is a theoretical curve assuming no delamination of the membrane for $Et = 1330$ N/m. Red, Blue and green curves are theoretical curves for three different values of the graphene/SiO₂ adhesion energy $\Gamma - 0.24, 0.30, 0.36$ J/m² respectively.
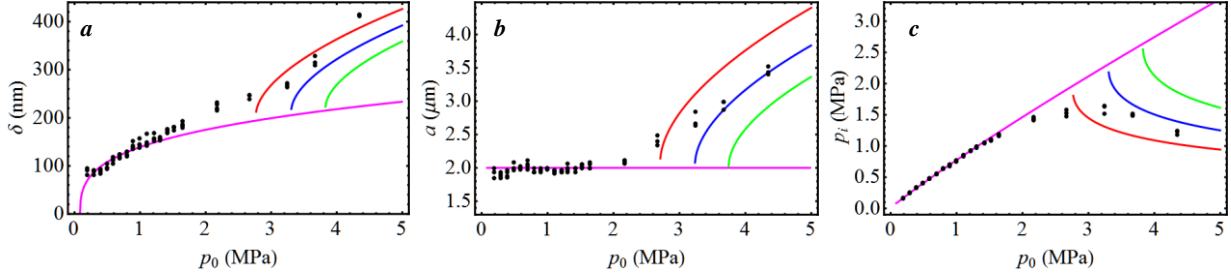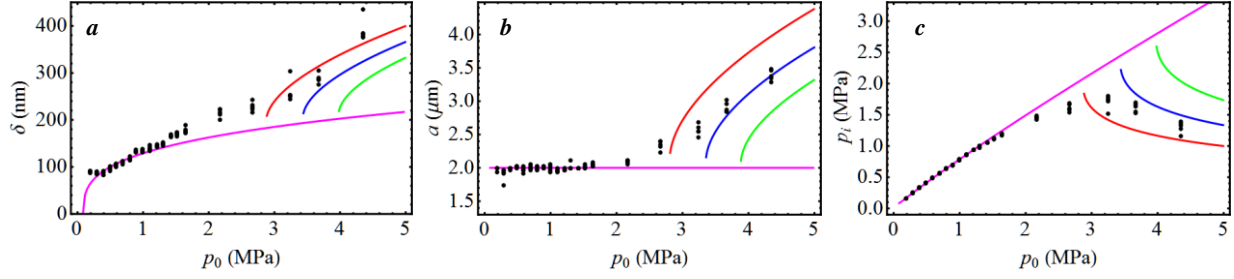
Figure A.5 Plots showing maximum deflection δ (a), blister radius a (b) and final equilibrium pressure p_i (c) versus input pressure p_0 for all five-layer membranes on Chip A. The magenta colored curve is a theoretical curve assuming no delamination of the membrane for Et = 1690 N m^{-1}, n = 5. Red, Blue and green curves are theoretical curves for three different values of the graphene/SiO$_2$ adhesion energy Γ – 0.24, 0.30, 0.36 J/m^2 respectively.

A.2 Appendix for Chapter 4

A.2.1 Determination of Graphene Thickness
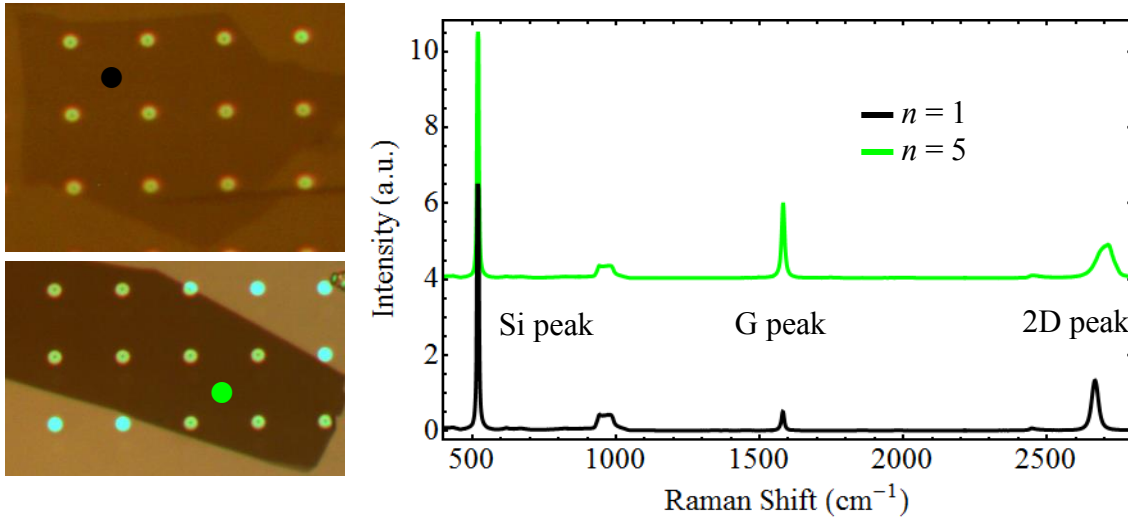
Figure A.6 Raman spectroscope of the graphene flakes (optical images on the left) used in the experiment - monolayer (black) and multilayer (green) graphene. The top image on the left is that of monolayer and the bottom one is that of multi-layered graphene. The location where the Raman spectroscopy is done is denoted by black and green dots respectively.

We used a combination of Raman spectroscopy and optical contrast to determine the number of graphene layers. Raman spectroscopy uses Raman (inelastic) scattering of monochromatic light to investigate rotation and vibrational modes in a system. We used the

relative integrated intensity of the graphene G peak and the Silicon optical phonon peak, *I(G)/I(Si)* as described in Koh et al[109] to count the number of layers. Figure A.6 shows the locations where the Raman spectrum is measured on the monolayer and multi-layered flakes used in the experiment using black and green dots respectively. The plot on the right shows the recorded Raman spectrum with the Si, G and 2D peaks identified. For reference, the Raman spectrum is also measured on a graphene flake with 1-5 layers of graphene identified optically. The recorded spectrum and the flake with the spots, where the spectrum is measured identified, is as shown in Fig. A.7. The relative integrated intensity *I(G)/I(Si)* is plotted in Fig. A.8 and as expected it varies linearly with the number of layers. The blue circular dots are from the reference flake and the red triangular dots are from the experimental flakes.
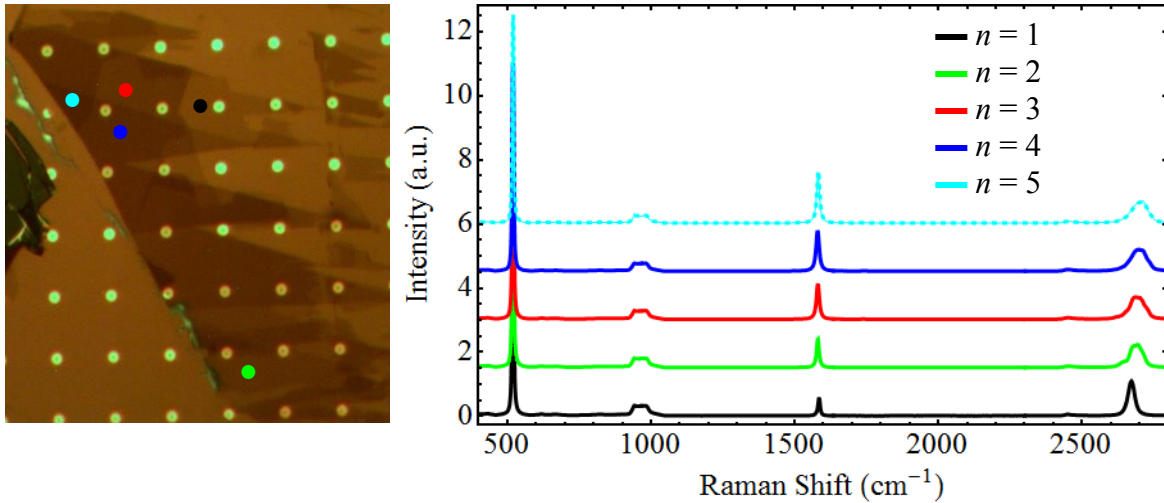
Figure A.7 Raman spectroscope of a graphene flake with 1 to 5 layers (n=1 – black, n=2 – green, n=3 – red, n=4 – blue, n=5 – cyan with the solid plot for this flake and the dashed plot for the experimental flake) used to confirm the number of layers in the multilayer graphene flake.
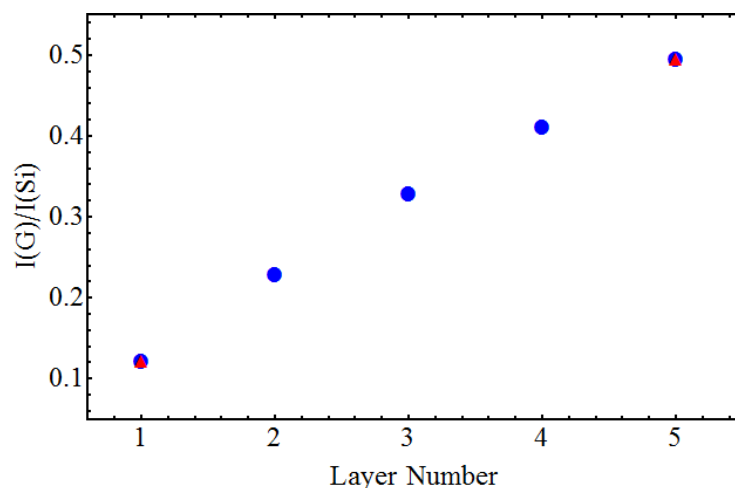
Figure A.8 Integrated intensities, I(G)/I(Si) for differently thick graphene sheets. The blue dots are for the graphene in the reference flake and the red triangles are for the sheets that make up the experimental flakes.

A.2.2 AFM Height Scans of a Monolayer Graphene Membrane

Figure A.9 Full AFM Height Scans of a monolayer device arranged in increasing order of charging pressures left to right and top to bottom. Darker regions indicate deflected membrane, while the white region is the graphene adhered to the substrate which is also the reference plane.

155

A.2.3 Sliding of Graphene Membranes

Hencky's series solution for clamped/fixed circular membranes describes the mechanics with two constants C_1 and C_2. Since the interfacial shear strength of grap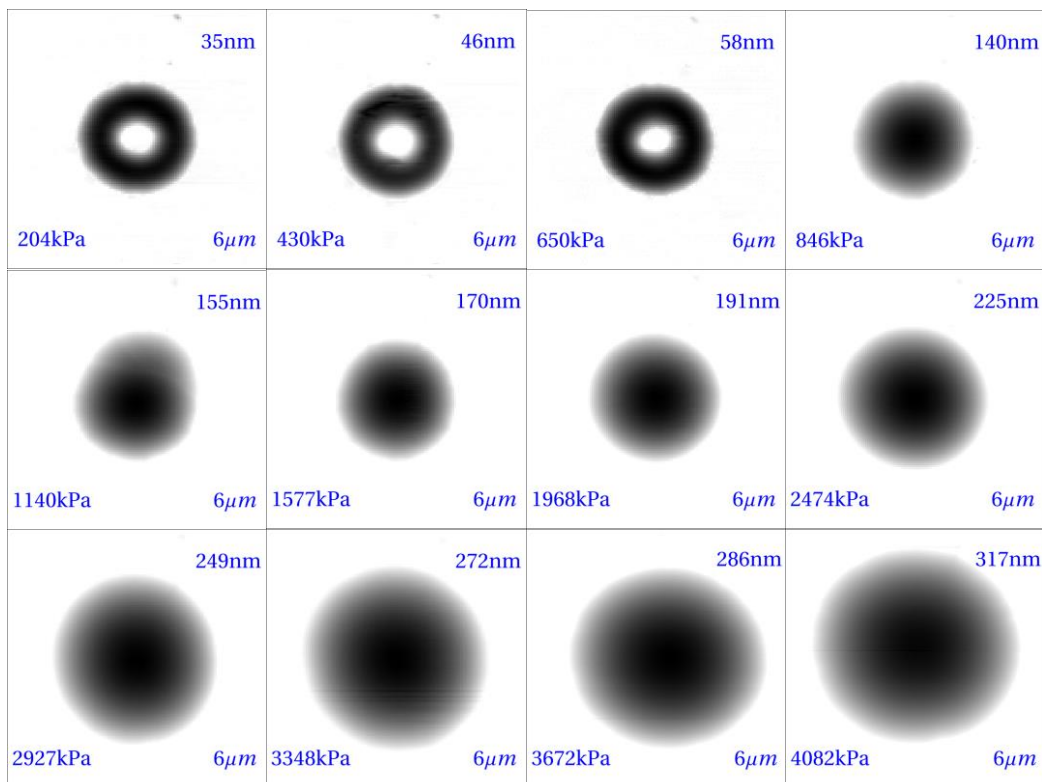hene-SiO$_x$ is finite and if it is small enough, the graphene membrane can slide on the substrate while still being adhered to the substrate[85]. This condition will lead to a larger membrane deflection than that predicted by Hencky's solution. We modified Hencky's solution to reflect the sliding boundary condition, and it turns out that the functional form of the solution remains the same except C_1 and C_2 are now different. We can show that even if C_1 is increased by 10% from the value obtained from Hencky's solution (0.525), the resulting increase in the calculated averaged adhesion energy is only about 3.4%. Hence, for simplicity we kept $C_1 = 0.525$ and used the resulting value of adhesion energy, 0.160 J/m^2. We then use C_2 as the lone fitting parameter to make the experimental observations (δ, a and p_i) self-consistent. We obtain a value of 0.755 that fits the theory with the experimental observations. This value is 10% higher than the value from Hencky's solution. Figure A.10 below shows the results of the fit.
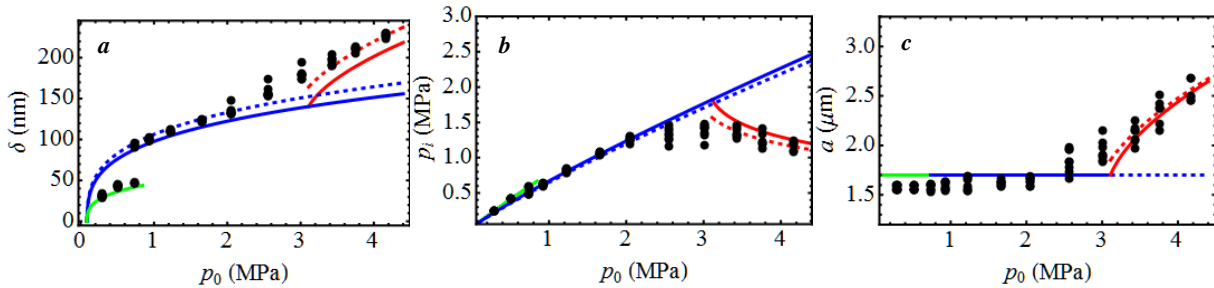
Figure A.10 (a) Maximum deflection, (b) Equilibrium pressure and (c) Outer radius of the circular bulge versus the charging pressure for multi-layered graphene membranes. In each case, the green curve corresponds to the annular deformation, blue curve is for the circular deformation without delamination, and red curves are for circular deformation with delamination for different adhesion energies (dashed - C_2 =0.755, solid - C_2 =0.686).

Sliding boundary conditions can also result in symmetry breaking deformation and hence wrinkling[110]. Apparent wrinkling in varying degrees is observed in all of the multi-layered devices at higher pressures ($\geq$ 2.56 MPa) as shown in Fig. A.11.
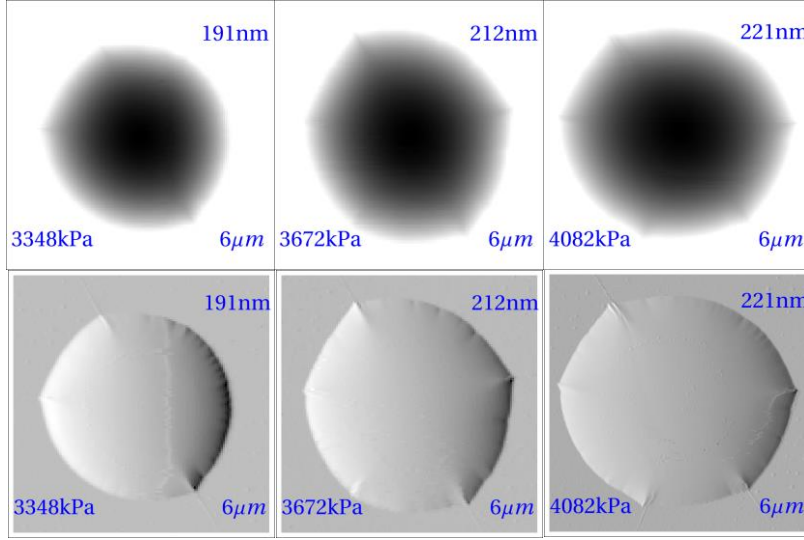
Figure A.11 AFM height scans (top row) and respective derivatives (bottom row) showing wrinkling of a multi-layered device at higher pressures.

A.3 Appendix for Chapter 7

A.3.1 Free Energy – Direct Integration

The free energy contribution of adhesion energy in eq. (7.9) can also be obtained directly by integration for sinusoidal surfaces. The result of this integration for potential between two surfaces, V_f (eq. (7.3)) is given by ($\delta = (a - c)/h$):

$$
\begin{aligned}
F_{adh} &= \int_0^\lambda \frac{dx}{\lambda} V_f(h + (a - c)\,\mathrm{Sin}[qx]) \\
&= \frac{\gamma}{6}\left(\frac{h_0}{h}\right)^4 \left(\left(\frac{h_0}{h}\right)^6 \frac{2(128 + 2304\delta^2 + 6048\delta^4 + 3360\delta^6 + 315\delta^8)}{64(1 - \delta^2)^{19/2}} - 5\left(\frac{(2 + 3\delta^2)}{(1 - \delta^2)^{7/2}}\right)\right)
\end{aligned} \tag{1}
$$

A.3.2 Generalized Free Energy using Complex Fourier Series

Let the substrate be described by the complex Fourier series, $s(x) = \sum_m c_m e^{iq_m x}$ and let us

assume that the graphene membrane follows the curve, $g(x) = h + z(x) = h + \sum_m a_m e^{iq_m x}$. In

this case, the free energy per unit volume following our approach will be:

$$
\begin{aligned}
F(a_m, h) = \frac{D}{2} \sum_m |a_m|^2 q_m^4 + V_f(h) \\
+ \sum_{j=1}^{n} \frac{d^j V_f(h)}{dh^j} \frac{1}{j!} \sum_{\substack{\sum_m l_m = j}}^{\sum_m m l_m = 0} \frac{j!}{\prod_m l_m!} \prod_m (a_m - c_m)^{l_m}
\end{aligned}
\tag{2}
$$

Here, c_m and a_m are the Fourier coefficients and are complex numbers; h (equilibrium separation)

and a_m being the unknowns. The internal summation in the nested summation of the last term is a

result of a multinomial expansion where l_m are the exponents which have to obey the constraints

$\sum_m l_m = j$ and $\sum_m m l_m = 0$ (note that m can take either positive or negative integer values). The

second of the constraints comes from the non-zero terms after integration of each term in the

multinomial expansion.

A.3.3 Post-processing of Simulation Results

The LAMMPS simulation package allows the user to output, at any given step,

thermodynamic quantities such as the temperature, total energy, constraint forces, size of the

system etc. It also enables users to output atomic coordinates for the whole system at any desired

step. We used this capability to obtain the energies in the initial and final configurations, the

projected area to calculate the adhesion energy per unit area. To obtain the amplitude, a and the

mean height, h, we used the atomic coordinates obtained from the final equilibrium configuration.

This is done programmatically using Mathematica scripting. In the script, we discarded the atoms at the edge of the graphene membrane and used the rest of the atoms to fit them to a function, $h + a\ Sin[\frac{2\pi x}{\lambda}]$ with a and h as the fitting parameters. It is clear that here we implicitly assume that the graphene membrane has uniform amplitude.

For the peeling simulations, the post-processing is more involved and we used a different Mathematica script for post-processing. As we displace the free end and perform energy minimization, the atomic coordinates of a strip of atoms in the middle of the membrane parallel to y-axis are saved. From these coordinates and for each value of d, we obtain the delaminated length, s which is defined to be the length of the membrane measured from the free end to the point where the z-coordinate of the atoms is below a threshold value (~6 Å for $c = 1$ Å). The peeling angle, θ is obtained by simply calculating the slope of the delaminated part of the membrane. Alternatively, it can be directly determined from the magnitude of the force components. The strain is calculated as the average of the strain along the length of the membrane with respect to the undeformed configuration. Finally, the amplitude (a) of the adhered region is simply obtained by looking at the maximum and minimum values of the z-coordinates of the atoms that are below the threshold z-coordinate and sufficiently far away from the "crack tip".

A.3.4 Bending Rigidity

We determined the bending rigidity of monolayer graphene by performing simulations wherein the atoms are arranged in a cylindrical fashion (as shown in Fig. A.12a) with a particular radius of curvature, R. We then constrained the atoms to move only on the cylindrical surface and let the system relax for 10 ps using a Noose-Hoover styled NVT ensemble at about 0 K. At the end of the simulation, the total energy of the system is expected to reach a stable value. The

difference of the final system energy from this simulation and the final energy for a flat sheet of graphene with the same number of atoms then gives the bending energy. For a cylindrical deformation, the bending energy per unit area is given by $U_b = \frac{1}{2}D\kappa^2$, where D is the bending rigidity and κ is the curvature. Using this equation and for different radii of curvatures starting from 40 Å to 400 Å in steps of 20 Å, we determined the bending rigidity. The results are plotted in Fig. A.12b. The value of D, as can be seen varies between 0.91-1.85 eV and the average value is 0.99 eV.
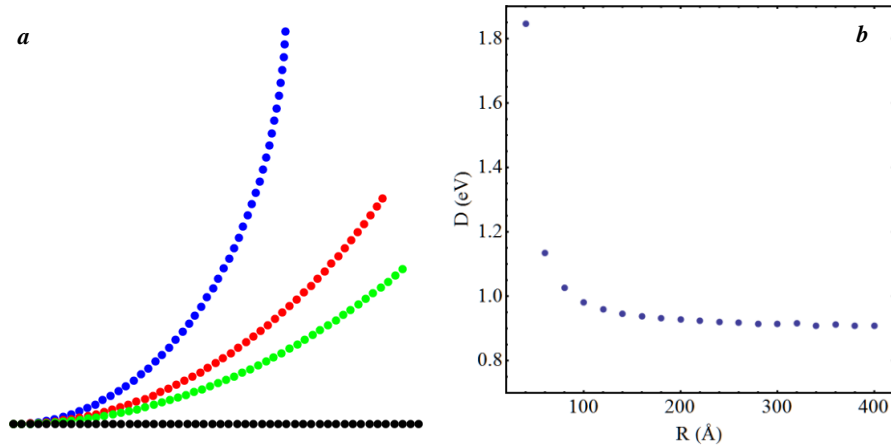

Figure A.12 (a) The atomic configurations used to determine the bending rigidity, blue – R=40 Å, red – 80 Å, green – 120 Å and black – flat, (b) Bending rigidity, D vs Radius of curvature, R.

A.3.5 Peeling from Corrugated Substrates – Limiting Case

The limiting case for peeling from corrugated substrates would be a flat substrate where $c = 0$. In the absence of corrugations, the membrane should also be flat i.e. $a = 0$. Hence, the free energy as described in 7.3.2 (see (7.15)-(7.18)) can now be written as:

$$F(x) = -\gamma x + \frac{Et}{2}l\epsilon(x)^2 \tag{3}$$

Here, $\epsilon = \frac{(d^2+s^2)^{\frac{1}{2}}-s}{l}$ and $s = l - x$ with all the symbols retaining their original meanings in 7.3.2.

Hence minimizing the free energy with respect to x leads us to:

$$\frac{dF(x)}{dx} = -\gamma + Et\epsilon(x)\frac{d\epsilon(x)}{dx} = 0$$

$$\Rightarrow \gamma = Et\epsilon\left(1 - \frac{s}{(d^2+s^2)^{\frac{1}{2}}}\right) \tag{4}$$

Notice that $f = Et\epsilon$ and $Cos[\theta] = \frac{s}{(d^2+s^2)^{\frac{1}{2}}}$, hence $\gamma = f(1 - Cos[\theta])$ which is equivalent to the

inextensible membrane version of the eq. (7.13). Thus we recover the energy release rate for the

flat substrate as the limiting case for peeling from a corrugated substrate.